



Faculté Des  
Sciences  
De Sfax



Università degli  
Studi  
di Genova



Consiglio  
Nazionale  
Delle  
Ricerche

---

## Design magnetic hybrid nanomaterials for molecules harvesting/ delivery

---

A dissertation submitted for the degree of  
Doctor of Philosophy in Sciences and  
Technologies of Chemistry and Materials  
by Sawssen Slimani (cycle: "XXXIV").

### Commission composed by:

Prof. Mouhamed Ellouze	University of Sfax, Tunisia.	(President)
Prof. Hedi Rahmouni	University of Kairouan, Tunisia.	(Reporter)
Prof. Bagher Aslibeiki	University of Tabriz, Iran.	(Reporter)
Prof. Chiara Bisaio	University of Eastern Piedmont, Italy.	(Examiner)
Prof. Davide Peddis	University of Genova, Italy.	(Supervisor)
Prof. Essebti Dhahri	University of Sfax, Tunisia.	(Supervisor)
Dr. Mourad Smari	University of Silesia, Poland.	(Invited)





Faculté Des  
Sciences  
De Sfax



Università degli  
Studi  
di Genova



Consiglio  
Nazionale  
Delle Ricerche



Laboratoire de Physique appliquée



Nanostructured  
Magnetic  
Materials Lab.



Istituto di  
Struttura Della  
Materia

## Design magnetic hybrid nanomaterials for controlled molecules harvesting/ delivery

by

Sawssen Slimani

Co-tutoring Doctoral thesis submitted to the University of Sfax, Tunisia and the University of Genova, Italy, in partial fulfilment of the requirements for the degree of Ph.D. in “Fundamental Science”, and “Scienze e Technologie della Chimica e dei Materiali”

Supervisors    **Prof.Dr. Davide Peddis**  
University of Genova, Italy.  
**Prof.Dr. Essebti Dhahri**  
University of Sfax, Tunisia.

2021-2022

**Sawssen Slimani**

Design magnetic hybrid nanomaterials for controlled molecules harvesting/ delivery

Co-tutoring Doctoral thesis submitted to the University of Sfax and University of Genova in partial fulfilment of the requirements for the degree of Ph.D. in “Fundamental Science”, and “Scienze e Tecnologie della Chimica e dei Materiali”, 2022

Supervisors: Prof.Dr. Essebti Dhahri and Prof.Dr. Davide Peddis and.

**Università degli Studi di Genova**

Department of Chemistry and Industrial Chemistry (DCCI)

Nanostructured Magnetic Materials Laboratory

Genova, Italia.

**Faculté des Sciences de Sfax**

Faculté des sciences de Sfax

Laboratoire de physique appliquée

Sfax, Tunisie.

**Istituto di Struttura Della Materia**

Consiglio Nazionale delle Ricerche, CNR

Nanostructured Magnetic Materials Laboratory

Monterotondo Scalo, Roma, Italia.





# Abstract

This thesis focuses on magnetic features in single and hybrid nanostructures. Magnetic material based on a spinel iron oxide structure ( $\text{MeFe}_2\text{O}_4$ ; Me:  $\text{Fe}^{2+}$ ;  $\text{Co}^{2+}$ ;) and coated by a mesoporous structure as well as by peculiar molecules (e.g. DNA) and by several types of polymers, have been investigated. The objective of the study is the design of single/hybrid nanoarchitectures with the aim of controlling the magnetic properties as well as their magnetic structure, which may serve as a basis for delivering and harvesting molecules in nanotechnological applications.

The magnetic properties of nanoparticles are particularly sensitive to the particle size, being determined by finite size effects on the core properties, related to the reduced number of spins cooperatively linked within the particle, and by surface effects, becoming more important as the particle size decreases physical properties differ greatly from their parent massive materials. Accordingly, the first part of the thesis is dedicated to the study of the different fundamental concepts of magnetism at the nanoscale.

We present morpho-structural and magnetic investigation of  $\text{Fe}_3\text{O}_4$  and  $\text{CoFe}_2\text{O}_4$  nanoparticles. In case of  $\text{Fe}_3\text{O}_4$  synthesized with co-precipitation method we have investigated: (i) the temperature effect, (ii) the reaction atmosphere effect and (iii) Cobalt doping effect in tuning specially the magnetic properties. The results reveal a significant change in the magnetic properties (i.e., saturation magnetization and coercive field) due to the Co-doping effect. While in the other cases magnetic properties were independent on the change in the experimental parameters within the experimental error.

The effect of surface modification for  $\text{Fe}_3\text{O}_4$  nanoparticles with mesoporous silica, DNA molecules and polyacrylic acid, gallic acid, oleic acid and polyethylene glycol was deeply investigated specially from magnetic point of view. The analysis of different cases shows the important role of the functionalization in tuning the properties of the magnetic core. We found that the surface coating has a large influence on changing the saturation magnetization, easy axis orientation in case of oleic acid and mesoporous silica respectively, as compared to the other cases where a change in the interparticle distance by 5% was the main observed change.

In case of  $\text{CoFe}_2\text{O}_4$  prepared with polyol method and coated with mesoporous silica structure also a small but evident decrease in the interparticle interactions is observed.

on the other hand, we also introduce a hybrid nanoarchitecture combining crystalline cobalt ferrite and the amorphous parent material, that behaves as an artificial single-phase material with enhanced magnetic anisotropy, well above the values achievable by the individual components. Apart from the experimental investigation micromagnetic modeling is presented as a tool to interpret the magnetic state of the nanocomposite. We compare the simulated result with the experimental one proving the observed large magnetic anisotropy and elucidating the active role of each phase.

Finally, we have introduced a theoretical investigation of permanent magnets with cubic geometry disposed in different configurations. Furthermore, experiments have been carried out using a home-made circuit, along with the development of a simple method for data treatment that enable to understand the behavior of the nanoparticles in an applied magnetic field.

## Abstract (Italian)

Questo lavoro di tesi è focalizzato sullo studio e l'ottimizzazione di proprietà magnetiche di nanostrutture magnetiche ibride per il trasporto controllato di molecole. Sono stati studiati materiali magnetici basati su ossido di ferro con struttura a spinello, anche con stechiometria complessa ( $\text{MeFe}_2\text{O}_4$ ; Me:  $\text{Fe}^{2+}$ ;  $\text{Co}^{2+}$ ), e rivestiti da molecole di vario tipo (es. Silice, mesoporosa, DNA, polimeri).

Le proprietà magnetiche sono particolarmente sensibili alla dimensione dei costituenti un materiale, essendo determinate da effetti di dimensione finita e da effetti di superficie, che diventano più importanti man mano che la dimensione della particella diminuisce. In quest'ottica, la prima parte della tesi è dedicata allo studio dei diversi concetti fondamentali del magnetismo su scala nanometrica.

Presentiamo un'indagine morfo-strutturale e magnetica delle nanoparticelle a stechiometria complessa  $\text{CoFe}_3\text{-xO}_4$ . Nel caso di  $\text{Fe}_3\text{O}_4$  sintetizzato con metodo di co-precipitazione abbiamo studiato: (i) l'effetto della temperatura, (ii) l'effetto dell'atmosfera di reazione e (iii) l'effetto della stechiometria nel controllo delle proprietà magnetiche. I risultati rivelano un cambiamento significativo nelle proprietà magnetiche (i.e., magnetizzazione di saturazione e campo coercitivo) a causa dell'effetto di drogaggio del Co.

$\text{Fe}_3\text{O}_4$  sono state funzionalizzate con silice mesoporosa, molecole di DNA e acido poliacrilico, acido gallico, acido oleico e polietilenglicole focalizzando l'attenzione sulla modifica delle proprietà magnetiche... È stato osservato che il rivestimento superficiale ha una grande influenza sul cambiamento della magnetizzazione di saturazione, l'orientamento dell'asse facile nel caso dell'acido oleico e della silice mesoporosa rispettivamente, rispetto agli altri casi in cui un cambiamento nella distanza interparticellare del 5% è stato il principale cambiamento osservato. Nel caso del  $\text{CoFe}_2\text{O}_4$  preparato con il metodo del poliolo e rivestito con una struttura di silice mesoporosa si osserva anche una piccola ma evidente diminuzione delle interazioni interparticellari.

Nell'ambito di questa ricerca è stato approfondito lo studio delle proprietà magnetiche di una nanoarchitettura ibrida che combina la ferrite di cobalto cristallina e il materiale amorfo genitore, che si comporta come un materiale monofase artificiale con anisotropia magnetica migliorata, ben al di sopra dei valori ottenibili dai singoli componenti. Oltre all'indagine sperimentale viene presentata la modellazione micromagnetica come strumento per interpretare le proprietà magnetiche del nanocomposito.

Infine, risultati preliminari sono stati ottenuti nello studio di configurazioni di magneti permanenti con proprietà ottimizzate per il recupero di particelle. In aggiunta, esperimenti preliminari di recupero dinamico di nanoparticelle sono stati fatti utilizzando un circuito « homemade »

## Acknowledgement

I present my warm thanks to **Dr. Davide Peddis**, associate professor of Physical Chemistry at the university of Genova and associate researcher at National Research Council (CNR, Rome) and **Dr. Essebti Dhahri**, Professor at the Faculty of Sciences of Sfax and, who agreed to give me a chance by allowing me to join their research teams. These two generous men, have always been able to guide me well during the Ph. D period, and share their precious knowledge and their overwhelming enthusiasm for physics and chemistry. These two persons with my most gratitude are not only my research supervisors but also a professional and personal example.

I express my gratitude to **Mr. Mourad Smari**, postdoctoral fellow at University of Aveiro, for the precious help, for his remarkable ideas, for his kindness, his availability. Once again, I thank my **Dr. Mourad Smari**.

I cannot forget **Dr. Sara Laureti** and **Dr. Gaspare Varvaro**, associate researchers at National Research Council (CNR, Rome) and **Dr. Fabio Canepa**, professor at the university of Genova, for their precious advices. I have benefited from their scientific knowledge a lot.

I would like to express all my gratitude and my thanks to my family and all my friends. I also want to thank all the people I have known during my Ph. D and my colleagues.

# Contents

	<b>Introduction.....</b>	<b>.....</b>
	<b>Aim and Thesis Structure.....</b>	<b>.....</b>
<b>1</b>	<b>Magnetism at nanoscale: an overview.....</b>	<b>1</b>
	1.1 Magnetism in condensed matter.....	2
	1.2 Finite size Effect.....	3
	1.3 Superparamagnetism.....	5
	1.4 Magnetic anisotropy .....	8
	1.4.1 Magnetocrystalline anisotropy .....	8
	1.4.2 Shape anisotropy .....	8
	1.4.3 Surface and interface anisotropy .....	9
	1.5 Interparticle interactions .....	10
	1.6 Supermagnetism.....	12
<b>2</b>	<b>Technologies and operating conditions of experimental process .....</b>	<b>13</b>
	2.1 X-ray diffraction analyses.....	14
	2.2 Transmission Electron Microscopy (TEM).....	16
	2.3 Superconducting Quantum Interference Device (SQUID).....	17
	2.3.1 Magnetization versus magnetic field.....	21
	2.3.2 Zero Field Cooled (ZFC)/Field Cooled (FC).....	22
	2.3.3 Thermoremanent magnetization (TRM) .....	24
	2.3.4 Remanence plot technique.....	26
	2.4 Mössbauer Spectroscopy.....	29
	2.5 Infrared Spectroscopy.....	31
	2.6 X-ray absorption Near-Edge structure (XANES) spectroscopy.....	32
<b>3</b>	<b>Nanoarchitecture based Hybrid Materials: Design the magnetic properties...34</b>	
	3.1 Definition and classification.....	35
	3.2 Iron oxide with spinel structure.....	41
	3.2.1 Crystalline Structure.....	42
	3.2.2 Magnetism in Spinel ferrites.....	43
	3.3 Designing Spinel ferrites nanoparticles: Co-precipitation.....	44
	3.3.1 Synthesis Process.....	45
	3.3.2 Temperature effect.....	46
	3.3.2.1 Structural Study.....	46

3.3.2.2	Magnetic properties and interparticle interactions.....	46
3.3.3	Atmosphere effect.....	50
3.3.3.1	Morpho-structural investigation.....	50
3.3.3.2	Magnetic structure.....	53
3.3.3.3	Interparticle interactions.....	56
3.3.4	Doping effect.....	60
3.4	Magnetic mesoporous silica-based hybrid materials: Investigation of the magnetic properties.....	63
3.4.1	Synthesis process: Polyol chemical method.....	64
3.4.2	Surface coating: mesoporous silica.....	65
3.4.3	Experimental investigation.....	66
3.3.3.4	Mesoporous silica coated CoFe <sub>2</sub> O <sub>4</sub> .....	66
3.3.3.5	Mesoporous silica coated Fe <sub>3</sub> O <sub>4</sub> : .....	70
3.4.3.2.1	Magnetization Dynamic.....	70
3.4.3.2.2	Nanoparticles Arrangement.....	71
3.5	Magnetism in hybrid material: Design new magnetic properties.....	75
3.5.1	Experimental investigation.....	75
3.5.1.1	Sample Preparation.....	75
3.5.1.2	Morpho-structural investigation.....	76
3.5.1.3	Magnetic properties.....	78
3.5.1.4	Random Anisotropy Model.....	82
3.5.1.5	Micromagnetic Model.....	87
3.6	Chapter Conclusions.....	91
<b>4</b>	<b>Surface and Interface Magnetism: The Role of Molecular Coating.....</b>	<b>94</b>
4.1	Role of organic coating to tune the magnetic properties.....	95
4.1.1	Ligand exchange process.....	95
4.1.2	Morphological study.....	96
4.1.3	Effect of organic coating.....	97
4.1.4	Interparticle interactions.....	99
4.1.5	Mutual relationship between colloid stability and magnetic properties .....	100
4.2	Magnetic nanoparticles coated with DNA molecules: study of magnetic properties.....	102
4.2.1	Magnetic properties.....	102
4.2.2	Effect of DNA coating: interparticle interactions.....	103

4.3	Chapter Conclusions.....	105
<b>5</b>	<b>Interaction Magnetic Core-Magnetic field.....</b>	<b>106</b>
5.1	Experimental Motivation .....	107
5.2	Magnetic nanoparticles in magnetic field .....	107
5.3	Permanent Magnets.....	108
5.4	Optimal configuration of magnets.....	108
5.5	Circuit for experiments in dynamic conditions.....	111
5.6	Chapter Conclusions.....	113
<b>6</b>	<b>Conclusions .....</b>	<b>114</b>
<b>7</b>	<b>Publications and Contributions.....</b>	<b>118</b>
7.1	List of publications	
7.2	Oral and poster contributions	
7.3	Events organization	
7.4	Schools and Workshops	
	<b>Bibliography .....</b>	<b>123</b>

## Abbreviations and Symbol list

<b>MD</b>	Multi-Domain
<b>(BH)max</b>	Maximum Energy Product
<b>CFO</b>	Cobalt ferrite
<b>DCD</b>	Direct current demagnetization
<b><math>\delta</math></b>	Inversion degree
<b><math>\delta m</math></b>	Delta-m plot
<b><math>E_{dip}</math></b>	Dipolar energy
<b>FC</b>	Field cooled
<b><math>H_k</math></b>	Anisotropy field
<b>H</b>	Magnetic field
<b><math>H_d</math></b>	Demagnetizing field
<b><math>H_c</math></b>	Coercive magnetic field
<b>SD</b>	Single-Domain
<b><math>T_c</math></b>	Curie Temperature
<b><math>T_N</math></b>	Néel Temperature
<b><math>r_c</math></b>	Critical radius
<b>FiM</b>	Ferrimagnetic/ferrimagnetism
<b>FM</b>	Ferromagnetic/ferromagnetism
<b>H</b>	Magnetic field
<b>PM</b>	Paramagnetic/Paramagnetism
<b><math>K_a</math></b>	Anisotropy constant
<b><math>M_s</math></b>	Saturation magnetization
<b>M</b>	Magnetization
<b>IRM</b>	Isothermal remanent magnetization
<b>NP</b>	Nanoparticle
<b>V</b>	Volume
<b><math>k_B</math></b>	Boltzmann constant

$\tau$	Relaxation Time
<b>MCA</b>	Magnetocrystalline Anisotropy
<b>Mr</b>	Remanent magnetization
<b>MNH</b>	Magnetic Nano-hybride
$\mu$	Magnetic moment
$\mu_0$	Vacuum permeability
<b>XAFS</b>	X-ray adsorption fine structure
<b>H<sub>int</sub></b>	Interaction field
<b>DS</b>	Debye Scherrer
<b>OA</b>	Oleic acid
<b>WH</b>	Williamson-Hall
<b>B<sub>ext</sub></b>	External field
<b>B<sub>hyp</sub></b>	Hyperfine field
<b>RKKY</b>	Ruderman Kittel Kasuya-Yosida-interactions
<b>SFM</b>	Superferromagnetic
<b>L<sub>Corr</sub></b>	Correlation Length
<b>SPM</b>	Superparamagnetic/superparamagnetism
<b>SSG</b>	Superspinglass
<b>SW</b>	Stoner – Wohlfarth
<b>T<sub>B</sub></b>	Blocking temperature
<b>TC</b>	Curie Temperature
<b>TEM</b>	Transmission electron microscopy
<b>XRD</b>	X-Ray diffraction
<b>RAM</b>	Random magnetic anisotropy
<b>T<sub>irr</sub></b>	Irreversible temperature
<b>T<sub>max</sub></b>	Maximum temperature
<b>PEG</b>	Polyethylene glycol
<b>TRM</b>	Thermo remanent magnetization
<b>SQUID</b>	Superconducting Quantum Interference Device

**$\chi_{irr}$**

**GA**

**PAA**

Irreversible Susceptibility

Gallic acid

Polyacrylic acid

## Introduction

Magnetism at nanoscale (i.e., nanomagnetism) is the field of physics that deals with the study of magnetic properties of magnetic materials (e.g., ferromagnetic, ferrimagnetic, and antiferromagnetic materials) with at least one of its geometric dimensions at the nanoscale (i.e., length scale between 1-100 nm) [1]. In recent decades, nanomagnetic materials have attracted considerable attention due to the plausible miniaturization of technological devices via nanostructuring and the potential development of advanced applications with the various nanoscale systems. For example, magnetic nanoparticles (MNPs) are potential candidates for multiple applications such as medical diagnosis and therapy [2], sensors [3], high-density magnetic recording, biochemical and nanofunctional devices, etc. Magnetic nanoparticles can be considered as unique complex physical objects whose magnetic properties are particularly sensitive to particle size, being determined by finite size effects, related to the reduced number of spins cooperatively linked within the particle, and by surface effects, becoming more important as the particle size decreases, leading to physical properties that differ greatly from parent bulk materials.

For nanoparticles, the multi-domain structure is no more energetically favorable and single magnetic domains are formed, each with a giant magnetic moment often referred to as a "super spin". Depending on the arrangement of the super spins (i.e., the strength of the interparticle interaction), an ensemble of magnetic nanoparticles can exhibit ferromagnetism-like (superferromagnetic), paramagnetism-like (superparamagnetic), or spinglass-like (superspinglass) behavior, constituting a new class of magnetism, called supermagnetism[4]. Every nanostructure exhibits different magnetic properties from each other and distinct magnetic states which become more exotic after the control of some parameters such as particle shape, size distribution, surface chemistry and chemical homogeneity and the competition of different interactions, which offer the opportunity to improve/design new magnetic properties.

## Aim and thesis structure

The research activity of this thesis focus on the design and the investigation of the magnetic properties of hybrid-materials as a system that can be used for controlled molecules harvesting/ delivery in different application areas, aiming to give a contribution in implement new synthetic approaches and/or understanding the behavior of fine particles, which path the way to tune their magnetic properties. The studies are carried out on nanostructured magnetic materials based on the spinel iron oxide structure ( $\text{MeFe}_2\text{O}_4$ ; Me:  $\text{Fe}^{2+}$ ;  $\text{Co}^{2+}$ ) then functionalized by different ligands/shell (i.e. polymers, mesoporous silica structure, DNA molecules etc.). These materials are good models' systems to show the relationship between the structural, morphological and the magnetic properties, which offer a good opportunity for understanding and tuning the magnetic features of fine particles.

This work is structured into six chapters that include the fundamentals of nanomagnetism, discussion of the results, and conclusions. A summary of the chapters is presented below:

### Chapter 1

The first chapter focuses in the basic concepts of the magnetism in condensed matter and at nanoscale.

### Chapter 2

In this chapter, detailed description concerns all the technologies and the operating conditions of the experimental process has been introduced.

### Chapter 3

this chapter discuss the design of the magnetic properties in nanomaterials, highlighting the correlation between the structural and the morphological properties with the magnetic features. The analysis of synthesized spinel iron oxide nanoparticles (magnetic core) under different reaction parameters will be reported. Their effect on the magnetic properties will be studied with different experimental magnetic protocols (i.e., ZFC/FC, TRM, DCD etc.). we follow with full investigation of the nanoparticles based hybrid material, we present novel classification of magnetic nanohybrid materials with respect to

the literature. Finally, this chapter will present also a novel approach to create magnetic hybrid material designed to improve magnetic anisotropy and interactions among their constituents. In addition, a micromagnetic model will be reported to explain the magnetic complex structure of the new system.

## Chapter 4

Introduce the role of the surface modification of nanoparticles to tune the magnetic properties. It will analyse the influence of different ligands used, on the interparticle interactions, the mutual relation between colloidal stability and the magnetic properties.

## Chapter 5

This chapter concerns the development of homemade circuit for a quantitative characterization of the behavior of magnetic nanoparticle in a magnetic field. A pre- investigation of better configurations of permanent magnet also will be reported.

## Chapter 6

This chapter summarizes the most important results and conclusions obtained from the different parts reported in this thesis.

# Magnetism at nanoscale: An overview

# 1

” The point is that, whenever we propose a solution to a problem, we ought to try as hard as we can to overthrow our solution, rather than defend it. Few of us, unfortunately, practice this precept; but other people, fortunately, will supply the criticism for us if we fail to supply it ourselves.

— **Karl Popper (1902-1994)** —  
(Philosopher)

In this chapter we give a short overview on magnetism at the nanoscale, summarizing the different fundamental concepts of nanomagnetism which are used in the following chapters

## 1.1 Magnetism in condensed matter

In condensed matter, two big classes of magnetic behaviour can be distinguished: non-cooperative and cooperative magnetism. The non-cooperative magnetism is observed if all magnetic moments were reciprocally isolated while the Cooperative magnetism is observed if the atomic magnetic moments can mutually act together. The non-cooperative magnetism can be presented by the paramagnetic and diamagnetic behavior of the material. Paramagnetism is described by an uncoupled atomic moment located in an isotropic environment, where no long-range order is present and the magnetic moments tend to align under an external magnetic field. Instead, diamagnetism is due to the effect of an applied magnetic field on the motion of the atomic inner electrons, inducing an opposite effect to the applied field.

In case cooperative magnetic system, the exchange interactions between adjacent magnetic moments determines the magnetic order in the material. We distinguish direct and indirect exchange interaction. Direct exchange interaction is observed when the magnetic moments are close enough to have a significant overlap of their wave functions, while indirect exchange interaction occurs when the atomic magnetic moments are coupled over relatively large distances, through e.g., a nonmagnetic ion that is placed between the magnetic ions, leading to the so-called super-exchange interaction. The exchange interactions between magnetic moments in a three-dimensional solid can be described by the Heisenberg Hamiltonian [5]:

$$H_{\text{exch}} = -2 \sum_{i < j} J_{ij} S_i \cdot S_j \quad (1.1)$$

where  $J_{ij}$  is the exchange integral describing the magnitude of coupling between the spins  $S_i$  and  $S_j$ . The magnetic behavior can be then classified based on the exchange integral sign. One can distinguish, the ferromagnetic (FM) behavior observed below the curie temperature,  $T_c$  (the temperature at which the transition from ferromagnetic state to paramagnetic (PM) state occurs) where the magnetic moments are aligned parallel to each other. The ferromagnetism is

observed when the exchange integral has a positive value (i.e.,  $J > 0$ ). In case  $J < 0$ , leads to antiferromagnetic (AFM) ordering has two oppositely directed sublattices with equal magnetic moments, that the net magnetization is equal to zero [6]. The transition temperature at which the AFM ordering disappears, known as the Néel temperature,  $T_N$  [7]. On the other hand, two oppositely directed sublattices with unequal magnetic moments constitute the ferrimagnetic order (FIM), whose non-zero net magnetization results from the difference between the magnetizations of the sublattices [8]. In crystalline ferrimagnet the magnetic atoms are distributed over two kind of lattice sites with different crystallographic environments, forming two sublattices, designated 'A' and 'B'. In each sublattice the magnetic moments are parallel to each other (ferromagnetically coupled). While the alignment between the moments of A and B is antiparallel (antiferromagnetically coupled). Large class of the most prominent magnetic materials are ferrimagnets, such as the spinel oxides (more details in section 2.2), that their magnetic properties can be tuned through this coupling.

## 1.2 Finite size Effect

The multidomain structure (MD) was explored first by Curie Weiss [9] who explain the existence of domain structure, which reduces the magnetostatic energy of a ferromagnetic system. The latter is consisting of a number of small regions (domains), each spontaneously magnetized to saturation. The boundaries between domains are called domain walls (DW) acting as transition zones of finite thickness in which the magnetization gradually changes from the direction on one side to that on the other side [10]. As the volume of the magnetic system decreases, the size of the domains and the width of the walls are reduced, modifying, then their inner structure. Below a certain critical size, the energy required to produce a domain wall is greater than the corresponding reduction in the magnetostatic energy. Consequently, the system no longer divides in smaller domains, forming a magnetic single domain (SD) [11,12], (**Figure 1.1**). The critical radius ( $r_c$ ) below which particles present the SD configuration can be expressed by the equation [13–15] :

$$r_c \approx 9 \frac{(AK_a)^{1/2}}{\mu_0 M_s^2} \quad (1.2)$$

where  $K_a$  is the anisotropy constant,  $M_s$  is the saturation magnetization,  $A$  is the exchange stiffness and  $\mu_0$  is the vacuum permeability. This  $r_c$  is characteristic of each material and in the range of nanometers.

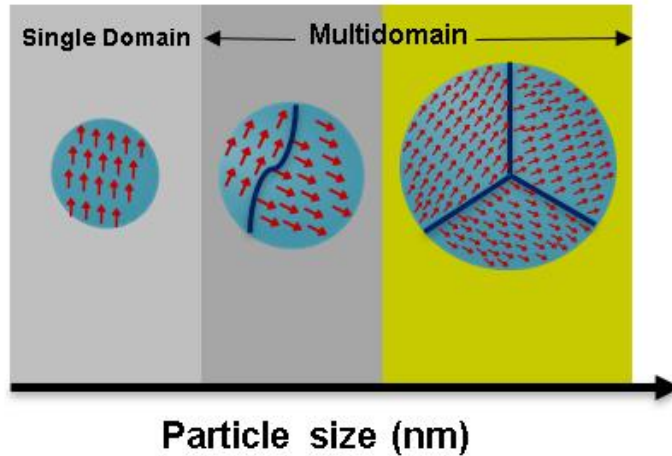


**Fig.1.1:** Magnetic domain configuration versus particle size evolution.

This change gives rise to the finite size effects originated from the geometric limitation of particle volume, that dramatically affects the particle's magnetic properties. As an example, the reduction in the particle size can lead to a change in the coercive field,  $H_c$  (details in section 4.1.3.1), **Figure 1.2**. When  $r_c$  is reached,  $H_c$  increases due to the incoherent spin rotation with the field. Once the maximum in  $H_c$  is reached, spins start to align with the field by coherent rotation, inducing a decrease in the coercive field [16]. With a continuous decrease in particle size,  $H_c$  falls to zero with a change in the magnetic behavior, called the superparamagnetism.

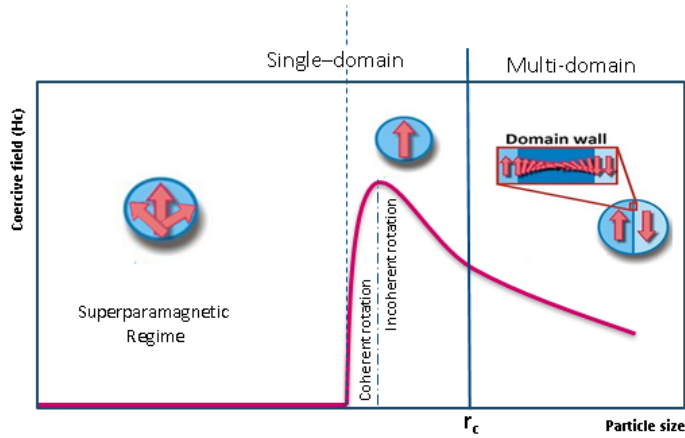


**Fig.1.2:** For larger grain sizes, coercivity decreases as the grain subdivides into domains (multidomain structure). Maximum coercivity field for a given material occurs within its single domain range. For extremely small grain sizes, coercivity falls to zero.

### 1.3 Superparamagnetism

The most interesting finite-size effect in small particle systems is the superparamagnetism [17,18]. The latter is analogous to the classical paramagnetism with different time and magnetization (M) scale. Superparamagnetism can be better described with Stoner-Wohlfarth model (SW). This model assumes that particles are in single domain state, all magnetic moments inside the nanoparticle (NP) undergo the reversal process coherently, with negligible interactions, with these conditions one can speak about “superspin” moment ( $\sim 10^3 - 10^5 \mu_B$ ). The energy of an ellipsoidal NP with uniaxial anisotropy can be written as:

$$E = K_a V \sin^2(\theta) - \mu_0 H V M_s \cos(\alpha - \theta) \quad (1.3)$$

K<sub>a</sub> is the effective anisotropy constant, V is the particle volume,  $\theta$  is the angle between magnetization vector and easy direction, M<sub>s</sub> is the saturation magnetization, and  $\alpha$  is the angle between the applied field (H) and the magnetization easy axis. The two terms present the magnetocrystalline anisotropy and the Zeeman energy respectively. In case of zero field, the NP

energy is a function of  $\sin^2$ , with two degenerate minima at  $\theta = 0^\circ$  and  $\theta = 180^\circ$ , which correspond to the two energetically favored orientations of the superspin moment along the easy axis separated by an energy barrier  $\Delta E = KV$ . If  $\Delta E$  is comparable or smaller than thermal fluctuation  $K_B T$ , nanoparticles are in superparamagnetic regime. Considering a long observation time during the M versus H measurement, the thermal fluctuation leads to a random reversal of the superspin moment, consequently to a closed loop of Langevin-type and zero spontaneous magnetization. For an applied field, the energy minima are shifted and the degeneracy is removed. A simplified case for  $\alpha = 0^\circ$  or  $180^\circ$ , squared hysteresis can be observed and  $H_c$  can be defined as the anisotropy field  $\mu_0 H_K = 2K/M_s$ .

For nanoparticles in superparamagnetic regime, the superspin dynamics at zero field can be described with Néel-Brown model. Given the thermal dependence, the model assumes the rotation on NP by Arrhenius law. The characteristic relation time can be expressed by:

$$\tau = \tau_0 \exp\left(\frac{E_B}{K_B T}\right) \quad (1.4)$$

Where  $\tau_0$  is the length of time characteristic of the probed material.

As mentioned above, the observation of the superparamagnetism depends for the time scale of the measurement  $\tau_m$ , thus from the experimental technique. As an example, in Mössbauer spectroscopy (details in section 4.1.4), the timescale is  $5 \times 10^{-9}$  sec, while in static magnetization measurements (details in section 4.1.3), the timescale is in the range 10-100 sec. Generally, in case  $\tau_m > \tau$  particles are in superparamagnetic regime, freely fluctuate. In  $\tau_m \ll \tau$ , particles are appeared to be in a blocked state. In addition, according to the eq 1.4,  $\tau$ , depends on the temperature (T). Accordingly, we can define a cross-over temperature separating the two states, which we call the blocking temperature,  $T_B$ . It is defined as that temperature at which the time scale matches with the relation time,  $\tau_m = \tau$  :

$$T_B = \frac{kV}{k_B \ln\left(\frac{\tau_m}{\tau_0}\right)} \quad (1.5)$$

In dc magnetization measurements,  $T_B$  is determined from the maximum in ZFC curve (details in 4.4.3.2), that the average blocking temperature is proportional to the ZFC maximum temperature, with a proportionality constant of  $\beta$ .

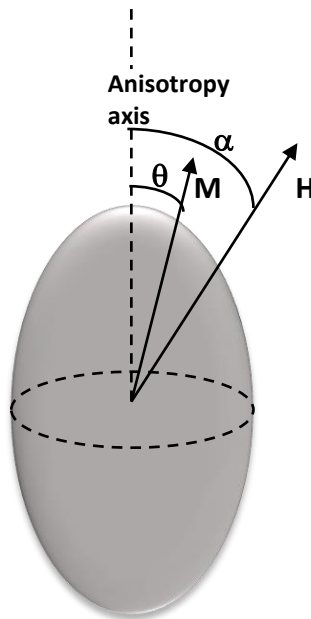


**Fig.1.3:** Sketch of the magnetization reversal for a monodomain particle with uniaxial anisotropy with an applied field  $H$ .

## 1.4 Magnetic anisotropy

The magnetic anisotropy [19–21] can be defined as the directional dependence of material's magnetic properties, inducing then the concept of preferred directions of the magnetic moment, called easy magnetization axes. Any deviation from these directions lead to an additional anisotropy energy on the system. As the anisotropy energy increase the magnetic moment are not any more orientated according to the easy axis but to the known as hard

magnetization axes. The magnitude and the type of the magnetic anisotropy [22,23] affect several macroscopic parameters such as saturation and coercivity. In bulk materials, magnetocrystalline and magnetostatic energies are the main sources of anisotropy. In magnetic nanoparticles, other types of anisotropy (e.g., surface anisotropy) can have the same order of magnitude as those of the bulk materials. A short qualitative discussion of some contributions will be provided at this point, with particular attention being paid to the most important anisotropies of the nanostructured systems. A complete description of magnetic anisotropy energy can be found elsewhere [6,8].

#### 1.4.1 Magnetocrystalline anisotropy

The magnetocrystalline anisotropy (MCA) is an intrinsic property of the magnetic material, which present the tendency of the magnetic moment to align itself along a preferred crystallographic direction and results from the spin-orbit coupling. under an applied magnetic field, the electron spin tends to reorient its direction, accompanied by a reorientation of the orbital due to the strong coupling between the spin and the orbital components. In addition, the orbital is also coupled to the system lattice therefore the attempt to rotate the spin axis is resisted. the symmetry of the MCA is the same as the one of the crystal structure, as an example in case of a particle with a single axis of high symmetry. The symmetry causes a uniaxial anisotropy energy, which is given by:

$$E_{\text{uni}} = K_1 V \sin^2 \theta + K_2 V \sin^4 \theta + \dots \quad (1.6)$$

$K_1$  and  $K_2$  are the anisotropy constants,  $V$  is the particle volume and  $\theta$  is the angle between the magnetization vector and the easy axis.

#### 1.4.2 Shape anisotropy

Shape anisotropy is another common kind of magnetic anisotropy belongs to the anisotropic shape of the magnetic materials. In case of perfect spherical system, the same field will magnetize it to the same extent in every direction. If it's not

the case, then it will be easier to magnetize the system along a long axis, which is known as shape anisotropy phenomenon. The origin of shape anisotropy is connected with the concept of the demagnetizing field. For a sample with a magnetization  $M_j$  magnetized with an external magnetic field along an axis  $j$ , the field inside this sample tend to be in the opposite direction to external field. The generated field is called demagnetizing field,  $H_d$ , that induce the demagnetization of the sample. The demagnetizing field is given by:

$$H_j^d = N_d M_j \quad (1.7)$$

$N_d$  is the demagnetizing factor which is determined by the shape of the sample. As an example, for elongated samples,  $N_d$  is small along the long axis and large along the short axis. The Demagnetizing factors can be very important, and in some cases a high field is required to magnetize a sample with a large demagnetizing factor.

### 1.4.3 Surface anisotropy

Magnetic behaviour near a surface in a magnetically ordered material may differ in most cases from that inside. This is due to the fact that the reduced symmetry, the change in the atom coordination number as a consequence of the finite particle size effect can offer the possibility of inducing new magnetic structures with new and interesting magnetic phenomena such as surface/interface anisotropy [24,25]. The lower symmetry at the surface produces an additional lower symmetry surface anisotropy term, which is larger than the bulk material. A phenomenological way to represent the contribution of the surface anisotropy to the total effective anisotropy is given by the equation [19]:

$$\langle K_{\text{eff}} \rangle = K_V + \frac{S}{V} K_S \quad (1.8)$$

where  $\langle K_{\text{eff}} \rangle$  represents the mean value of the effective anisotropy constant,  $\langle K_V \rangle$  volume magnetic anisotropy term and  $\langle K_S \rangle$  represents the surface anisotropy term.

This fact was first treated by Néel based on a phenomenological approach [26]. For small surface anisotropy, we can observe a regime of quasi-collinear spin (Figure 1.4a) and as the surface anisotropy increases, the switching mechanism becomes less coherent (Figure 1.4b).

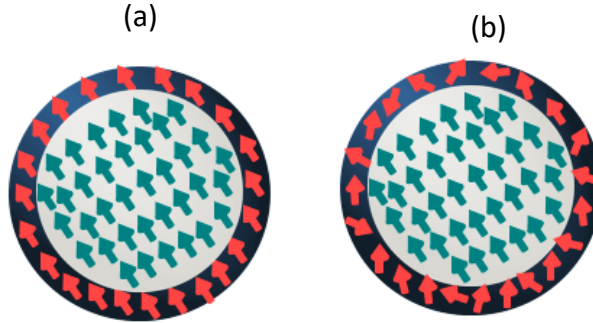


**Fig.1.4:** (a) Collinear spin configuration and (b) Non collinear spin configuration of a spherical particle.

## 1.5 Interparticle interactions

The existence of interparticle interactions has a significant influence on the magnetic behavior of a superspin ensemble. In general, these interactions are similar to those governing the spin interaction at the atomic scale, but at the nanoscale, i.e., the individual atomic spin is replaced by a superspin (giant moment) and taking into account the distance between the nanoparticles. Below we present a brief description of some types of magnetic interaction, highlighting the important interactions at the nanoscale. A more detailed description can also be found elsewhere [27,28].

An ensemble of spins of average moment  $\mu$  and average distance  $d$ , have an average energy of dipolar interactions ( $E_d$ ) expressed by [29]:

$$\langle E_d \rangle \cong \frac{\mu_0 \langle \mu^2 \rangle}{4\pi d^3} \quad (1.9)$$

Where  $\mu_0$  is the vacuum permeability. The high magnitude of dipolar interactions at nanoscale can induce a significant change in the magnetic behavior of the material [30,31]: an increment in the effective anisotropy, increasing the

blocking temperature of nanoparticles, inducing a kind of modified superparamagnetic behavior.

By increasing the interaction strength (very strong interaction), with the presence of randomness and the frustration, one can find the superspin glass [32] (SSG) phase below a critical temperature,  $T_g$ . This case is termed superspin glass, since the behavior is similar to spin glasses like but instead of atomic spins the particle superspins freeze into a spin glass phase below a critical temperature,  $T_g$ . In this case the relaxation time is given by:

$$\tau = \tau^* \left( \frac{T - T_g}{T_g} \right)^{-z\nu} \quad (1.10)$$

where  $\tau^*$  is the relaxation time of non-interacting particles and  $z\nu$  is the critical exponent.

When the dipolar interactions are strong enough and the spatial arrangement of nanoparticles ordered enough, ferromagnetic-like correlations of the superspin moments occur. This behavior is termed superferromagnet [33] (SFM), where  $\tau$  is given by:

$$\tau = \tau^* \left( \frac{T - T_c}{T_c} \right)^{-z\nu} \quad (1.11)$$

When particles are in close contact, electrons on neighboring magnetic atoms undergo exchange interaction [13,34], this is known as direct exchange. For a strong exchange coupled superspins, super ferromagnetism (SFM) occurs. On the other hand, if particles embedded in an insulating matrix, superexchange interaction can occur via intermediate atoms or ions (e.g., oxygen). When, the matrix and particles are both metallic, Ruderman-Kittel-Kasuya-Yosida (RKKY) interaction occurs and it varies as  $1/d^3$  ( $d$  is the interparticle distance) [35,36].

## 1.5 Supermagnetism

the magnetic behaviour of an ensemble of nanoparticles show a strong dependence on the interparticle interactions. Depending on the type and the strength of the interactions and due to the advanced time and magnetization scale an ensemble of nanoparticles can be in superferromagnetic (ferromagnetic-like), superparamagnetism (paramagnetic-like), superspin glass (spin-glass-like) behavior, which has been often called supermagnetism[4].

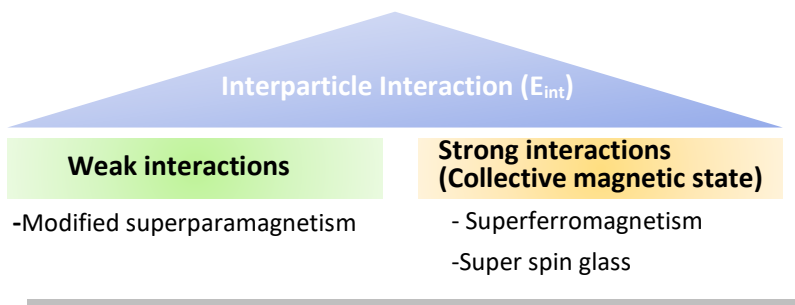


**Fig.1.5:** Supermagnetism.

## Technologies and operating conditions of experimental process

This chapter provides a brief overview of the characterization techniques used to analyze the materials reported in the thesis. The initial stages of analysis involve morpho-structural characterization using transmission electron microscopy (TEM) and X-ray diffraction (XRD) respectively. Fourier transform infrared spectroscopy (FTIR) was used to reveal the different functional groups on the surface of the nanoparticles, especially in case of functionalization. The structure and magnetic properties were characterized by Mössbauer spectroscopy and a superconducting quantum interference device (SQUID) respectively. Since magnetic properties being the main subject of this thesis, a more detailed explanation of the operation mode is devoted to the SQUID instrument. An overview on the different experimental protocols (ZFC/FC; TRM etc.) and the softwares used for data treatments are also reported.

## 2.1 X-ray Diffraction analyses

In 1912 Max Van Laue demonstrated that X-rays were diffracted by crystals following his success in determining the wavelength of X-rays using a crystal lattice. Subsequently, most scientists used X-rays to study crystalline structures, citing Pasteur's example in biology. The non-destructive X-ray diffraction analysis makes this technique a powerful problem-solving technique that can be applied in many different fields. This method only applies to crystalline media with the characteristics of the crystalline state (a periodic, ordered arrangement of the constituent atoms). It allows access to a lot of information such as the analysis of the angular positions of the diffraction lines which informs us about the type of geometrical arrangement (type of lattice P, I, F or C), the lattice parameters  $a$ ,  $b$ ,  $c$ ,  $\alpha$ ,  $\beta$ ,  $\gamma$ , while the analysis of their relative intensities allows us to discuss the position of the different atoms within the crystallographic lattice, thus constituting a "unique" identity card for each compound.

X-rays are high-energy electromagnetic radiation with short wavelengths ranging from 0.5 to 2.5 Å, which makes them more suitable for the study of periodic crystalline structures with interatomic distances of the same order of magnitude. The structural characterization of all the samples reported in this thesis is carried out by X-ray diffraction, the principle of which consists of sending a monochromatic X-ray beam onto the sample, the incident beam will be diffracted at certain specific angles and the recording of the signal is done by a suitable detector allowing the determination of the angles and intensities of the diffraction peaks obtained. Thus, the X-ray radiation elastically scattered by a crystalline sample shows constructive interference in a very limited number of directions. This diffraction phenomenon is modelled by Bragg's law demonstrated by W.H. Bragg and his son W.L. Bragg:

$$2 d_{hkl} \sin \theta = n\lambda \quad (2.1)$$

$d_{hkl}$  is the inter-reticular distance, which is the distance between two crystallographic planes.  $\theta$  is the half angle of deflection (half the angle between the incident beam and the detector direction).  $n$  is the order of the reflection and defines the X-ray wavelength.

The crystalline structure of our samples was characterized by X-ray diffraction (XRD) measurements, using a TT 3003 diffractometer (Seifert, Ahrensburg, Germany) equipped with a secondary graphite monochromator, employing  $\text{CuK}\alpha$  radiation ( $\lambda = 1.5418 \text{ \AA}$ ), **Figure 2.1**. Data were collected in the  $10^\circ$ – $70^\circ$   $2\theta$  range with a step size of  $0.04^\circ$  and counting 4 sec per step.

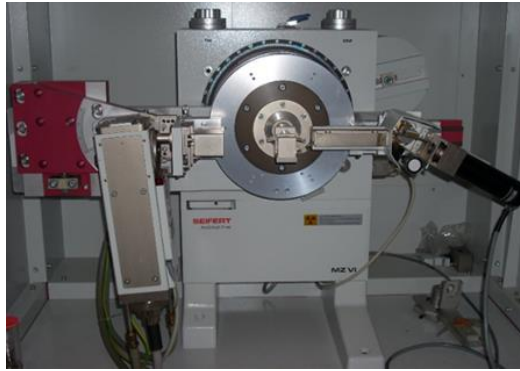


**Fig.2.1:** XRD Seifert 3003 TT diffractometer.

Apparent crystallite sizes are obtained from the Scherrer equation. The formula relates the breadth  $B_{hkl}$ , or full width at half-maximum of a certain peak in the X-RAY pattern to the average crystallite size  $D_{hkl}$ :

$$D_{hkl} = \frac{k\lambda}{B_{hkl} \cos \theta} \quad (2.2)$$

where  $\lambda$  is the average X-ray wavelength of  $\text{K}\alpha$  and  $\text{K}\beta$  radiation of Cu ( $\lambda = 0.154187 \text{ nm}$ ),  $\theta$  is the Bragg angle expressed in radians.  $k$  is the Scherrer constant which is most often cited in the literature as having a value of about 0.9 [37]. For our study, intense and symmetrical peaks were chosen and fitted with pseudo-Voigt function to calculate the average crystallite size.

In addition, we also employed the Williamson-Hall (WH) method [38,39] for some samples for comparison with the size trend given by the Scherrer formula. WH is based on the principle that the approximate formulas for size broadening,  $\beta_L$ , and strain broadening,  $\beta_e$ , vary very differently with respect to the Bragg angle,  $\theta$ . Equation 2.2 shows that the Scherrer equation follows a  $1/\cos\theta$  dependency, but WH method show dependency on  $\tan\theta$ :

$$\beta_{\text{tot}} = \beta_L + \beta_e \quad (2.3)$$

$$\beta_{\text{tot}} = \frac{k\lambda}{B_{\text{hkl}} \cos \theta} + 4\varepsilon \tan \theta \quad (2.4)$$

multiply equation (2.4) by  $\cos\theta$  we get:

$$\beta_{\text{tot}} \cos \theta = \frac{k\lambda}{B_{\text{hkl}}} + 4\varepsilon \sin \theta \quad (2.5)$$

$\beta \cos\theta$  was plotted with respect to  $4\varepsilon \sin\theta$  and size component is obtained from the y-intercept of the fitted line.

## 2.2 Transmission Electron Microscope (TEM)

The morphological characterization of the samples is carried out using a CM200 microscope (Philips, Amsterdam, The Netherlands.) operating at 200 kV and equipped with a LaB6 filament. The transmission electron microscope (TEM) is a very powerful focal tool, which works on the principle of sending a very fine beam of high-energy electrons that is focused by a series of electromagnetic lenses. The number of backscattered electrons and/or secondary electrons generated by the beam emerging from the sample are collected by an electron detector and an image of the sample is formed.

Study the nanoparticles morphology by TEM analysis provide a comprehensive overview on the ensemble of nanoparticles and allowing to extract additional

and relevant information about size and shape. Statistical analysis was performed using the free “ImageJ” software. The use of software like ImageJ allows collecting information about individual particle such as the area and perimeter of the projected image. To evaluate the average diameter for the spherical-like particles, we calculate the mean value between the maximum width and length of the particle. Then, the frequency counts of particles size are fitted with a lognormal function given by [40] :

$$P = \frac{1}{D\sigma\sqrt{2\pi}} \exp \left[ -\frac{\ln^2(D/D_{\text{TEM}})}{2\sigma^2} \right] \quad (2.6)$$

where  $\sigma$  is the standard deviation and  $D_{\text{TEM}}$  is the median of the log-normal distribution.

### 2.3 Superconducting Quantum Interference Device (S.Q.U.I.D)

The magnetic behavior of the produced magnetic systems is the central issue of this work. The response to an applied magnetic field and temperature variation usually defined the magnetic properties of the nanoparticles. For example, the experimental observation of the superparamagnetism depends from the measuring time of the experimental technique ( $\tau_m$ ) with respect to the relaxation time ( $\tau$ ).

As  $\tau_m \ll \tau$ , the magnetic moments seem blocked and the properties are the same of a bulk material. While, if  $\tau_m \gg \tau$ , the magnetization of the sample fluctuates between the easy directions (dynamic properties). The study of the sample behavior in a wide range of applied magnetic field and temperature was carried out using Superconducting Quantum Interference Device (S.Q.U.I.D.). The magnetometer produces a magnetic field ranging from zero to  $\pm 5T$  generated by the superconducting solenoid. The sample temperature varies from 4.2K, the cooling process is performed in presence of liquid helium, up to 400K.

The measurements can be performed on samples in liquid form, using specific type of capsules, or in form of powder mixed with epoxy resin to prevent the particles movement during the measurement. The measurements are controlled by a computer that is following a previously prepared measuring sequence. A schematic presentation of the used SQUID system is illustrated in **Figure 2.2**.

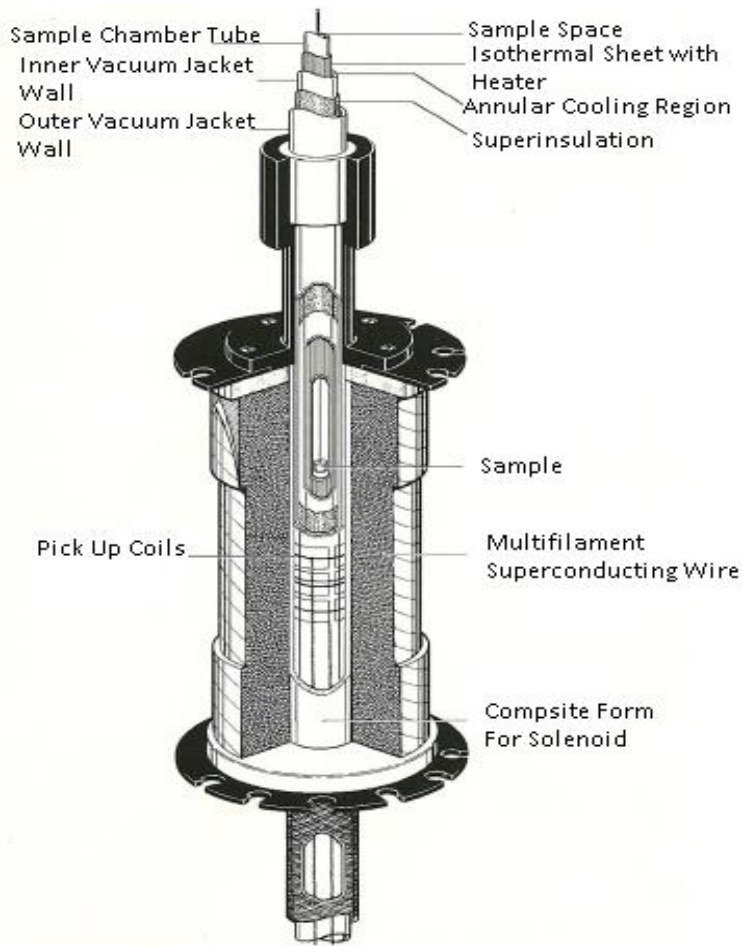


**Fig.2.2:** Schematic overview of the SQUID magnetometer [41].

The used set-up holds a second-order gradiometer, which brings many benefits, since the first-order coils aren't sensitive to a change of the homogenous external field, whereas field gradients induce a voltage. Second-order gradiometer superconducting detection coil and the detected signal are reported in **Figure 2.3**.

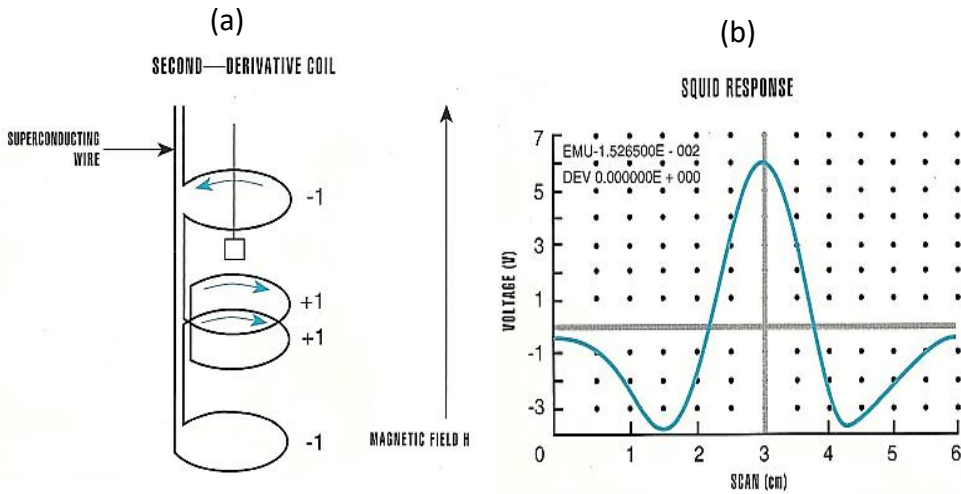


**Fig.2.3:** (a) configuration of the second-order gradiometer superconducting detection coil, (b) detected signal [41].

Furthermore, the SQUID loop is composed by two Josephson junctions forming a ring structure. The Josephson junction is an insulating layer coupling two superconductors. In absence of an external voltage or magnetic field, the dc current flows through such a junction give rise to the so called dc Josephson effect:

$$j = j_m \sin \delta_0 \quad (2.7)$$

$j_m$  is the maximum current density and  $\delta_0$  is the phase difference between both sides of the junction.

If an external voltage is applied, the potentials  $\vec{A}$  and  $U$ , lead to the ac Josephson effect given by:

$$j = j_m \sin[\delta_0 - \omega t] \quad (2.8)$$

$\omega$  is the frequency of the oscillating current arises over the junction.

In the presence of a very small magnetic field only  $\vec{A}$  is a position dependent phase shift therefore:

$$\delta = \delta_0 + \frac{2\pi}{\phi_0} \int \vec{A} \cdot d\vec{l} \quad (2.9)$$

$\phi_0$  is the flux quantum. With the equations (2.7), (2.8), (2.9), also complex arrangements of Josephson junctions can be described, like a SQUID loop. Thus, a magnetic flux  $\phi$  is flowing perpendicular through the ring, **Figure 2.4**. The detected current oscillates with changing magnetic flux penetrating the SQUID by multiples of the flux quantum  $\phi_0$ . Accordingly, the device can be used to measure very small changes in magnetic fields.

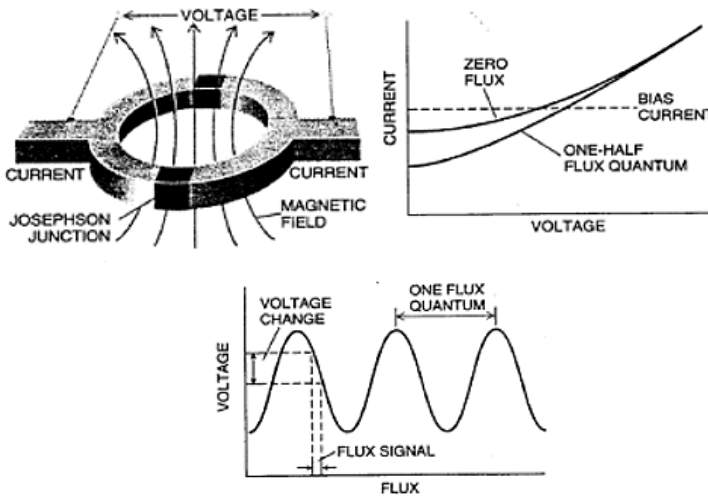


**Fig.2.4:** The basic function of the SQUID [42].

### 2.3.1 Magnetization versus magnetic Field

The magnetization measurement was carried out under an applied field of  $\pm 5T$ . The first measurement was performed at low temperature (5K), below the blocking temperature. Under these conditions the sample shows an irreversible loop (Hysteresis loop) typical for a ferromagnetic material. Magnetic hysteresis is promoted by different factors, that can be intrinsic or extrinsic to the material, as summarized in **Figure 2.5**.

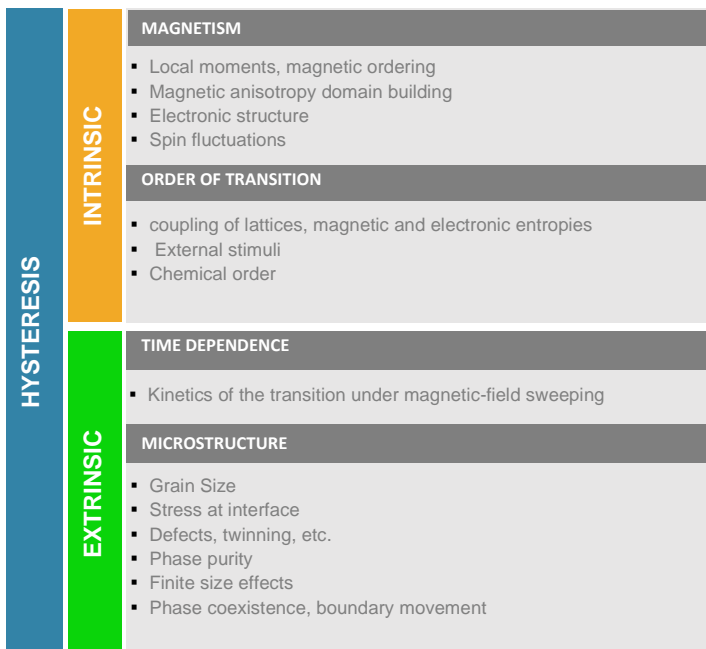


**Fig.2.5:** Intrinsic and extrinsic sources of hysteresis effects [43].

**Figure 2.6a**, shows an example of a hysteresis loop measured at 5K. The hysteresis parameters are the coercive field ( $H_c$ ), saturation magnetization ( $M_s$ ) and remanent magnetization ( $M_r$ ).

Saturation magnetization is defined when the sample reach the saturation (all the magnetic moments are aligned in the direction of the magnetic field) after  $H_{max}$  is applied.  $M_s$  is obtained by fitting the high field part of hysteresis curve by:

$$M = M_s \left( 1 - \frac{a}{H} - \frac{b}{H^2} \right) \quad (2.10)$$

$M_r$  (defined the residual magnetization after the field removal) and  $H_c$  (defined as the field necessary to cancel the remanent magnetization, and it is usually proportional to the average anisotropy energy) are determined directly from the graph, using a simple linear fit.

On the other hand, if the magnetic  $M$  vs  $(H)$  is performed above the blocking temperature, a superparamagnetic behavior ( $M_r=0$  and  $\mu_0 H_c = 0$ ) can be observed, **Figure 2.6b**.

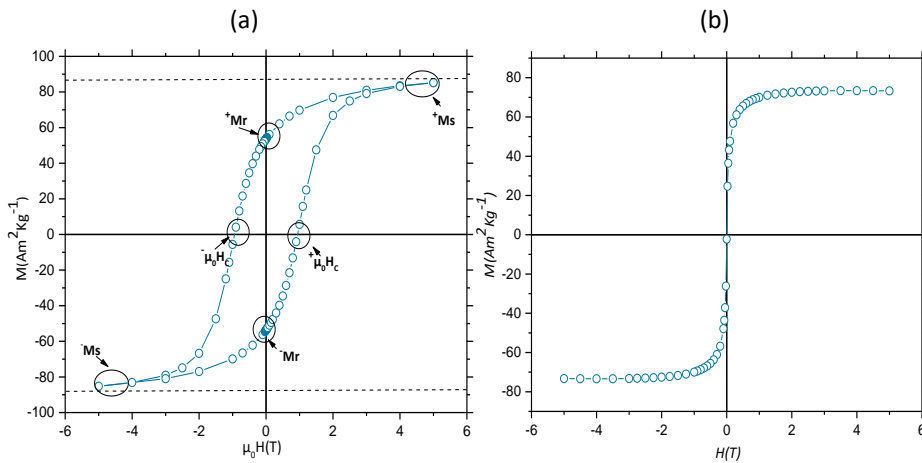


**Fig.2.6:** An example of  $M$  Vs  $H$  curves is shown: (a) at  $5\text{K}$ , the coercive field  $\mu_0 H_c$ , the remanent magnetization  $M_r$  are evidenced, and (b) at  $300\text{K}$ ,  $M_r=0$  and  $\mu_0 H_c=0$ .

### 2.3.2 Zero Field Cooled (ZFC)-Field Cooled (FC) protocols

Temperature dependence of magnetization is investigated by Zero Field Cooled (ZFC) and Field Cooled (FC) protocols. The experiment is performed in the temperature range  $5\text{K}$ - $325\text{K}$ . For ZFC measurement, the sample is cooled down from room temperature to  $5\text{K}$  in zero magnetic field, accordingly all the net

magnetic moments in each single domain particle aligned along the easy axis. Then a small magnetic field is applied and  $M_{ZFC}$  is measured during warming up, the resulting curve is called ZFC curve. The maximum temperature in ZFC curve is directly proportional to the average blocking temperature,  $T_B$ , with a proportionality constant,  $\beta$  which depend on the type of particle size distribution for a log-normal distribution,  $\beta = 1.5-2$  [44]:

$$T_{max} = \beta T_B \quad (2.11)$$

$M_{FC}$  is measured during the cooling process from 300K to 5K in presence of the same magnetic field applied during the ZFC measurement. When the substance is cooled under an applied magnetic field, the magnetization direction of the nanoparticles is frozen. At high temperatures, the particles are no longer in the blocked state, the magnetization decreases and a significant number of nanoparticles are in the superparamagnetic regime. **Figure 2.7** illustrate an example of ZFC-FC curves of interacting magnetite sample (FeO), where below a given temperature an irreversible behavior is observed. The temperature at which this irreversible behavior is observed called irreversibility temperature ( $T_{irr}$ ). The latter is related to the blocking temperature of the biggest particles.  $T_{irr}$  is defined as the temperature at which the difference between  $M_{FC}$  and  $M_{ZFC}$  becomes smaller than 3% [45].

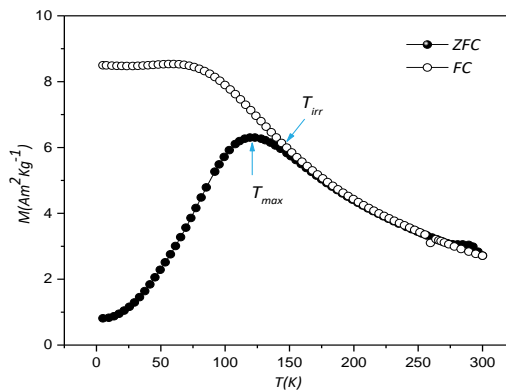


**Fig.2.7:** An example of ZFC (empty circles) and FC (full circle) curves of interacting nanoparticles is shown.

### 2.3.3 Thermoremanent magnetization (TRM)

To perform the thermoremanent magnetization (TRM) measurement [46], the sample was first cooled down in presence of external magnetic field from 300K to 5K. After the field is turned off,  $M_{\text{TRM}}$  is measured during warming up. At 5K, the nanoparticles are frozen and the random oriented nan-powder lead to a broad distribution in the anisotropy energy barrier. As the temperature increase, number of nanoparticles overcome their energy barrier, thus the magnetization direction of each thermally activated nanoparticle starts to flip randomly, leading to a decrease in the overall magnetization of the nanoparticles.

$$M_{\text{TRM}} = M_{\text{nr}} \int_{\Delta E_a}^{\infty} \mathcal{F}(\Delta E) dE \quad (2.12)$$

$M_{\text{nr}}$  is the non-relaxing component of the magnetization and  $\Delta E_a$  is a critical value of energy, below which all the particles are blocked. An estimation of the anisotropy energy barrier distribution can be given by [47]:

$$\mathcal{F}(\Delta E) \propto -\frac{dM_{\text{TRM}}}{dT} \quad (2.13)$$

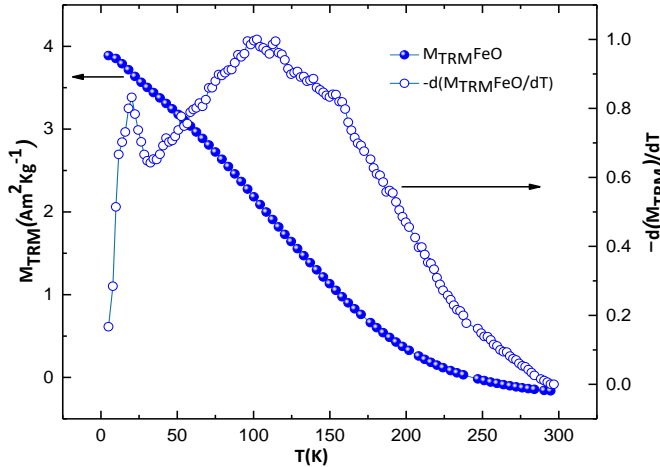


**Fig.4.8:** TRM curve (full circles) and the anisotropy energy distribution (empty circle) of FeO sample (with the ZEC/FC curves reported in Fig2.7).

In the section 1.3, the blocking temperature was defined as the temperature at  $\tau_m = \tau$ , however in real system, where nanoparticles have a distribution of size,  $T_B$  is defined as the temperature at which 50% of the particles are in superparamagnetic regime [48]. At a given temperature, the system of nanoparticles can contain two populations of particles in different states: blocked particles,  $P_B$  and particles in superparamagnetic regime,  $P_S$  and  $P_T$  is the total population. The integration of the area below the  $f(\Delta E)$  curve provides the relative ratio of these two subpopulations:

$$\int \mathcal{F}(\Delta E) \propto R(T) = \frac{P_B(T_x)}{P_S(T_x)} = \frac{\int_{T_x}^{T_{\max}} \mathcal{F}(T) dt}{\int_0^{T_x} \mathcal{F}(T) dt} = \frac{P_T - P_S(T_x)}{P_S(T_x)} \quad (2.14)$$

The temperature at which  $R=1$  corresponds to the blocking temperature, where 50% of particles are in superparamagnetic regime, i.e., the temperature at the integral (equivalent to the TRM derivative) reaches its maximum value. A good approximation of the TRM curve can be obtained from ZFC/FC measurements [46].

The total magnetic response of any magnetic system is given by:

$$M_{\text{tot}}(H, T, t) = M_{\text{rev}}(H, T) + M_{\text{irr}}(H, T, t) \quad (2.15)$$

$H$  is the measuring field,  $T$  is the measurement temperature and  $t$  is the measurement time. The first part represents the reversible part which is time independent and the second part represent the irreversible part which is time independent.

Looking to the thermal dependence of magnetization measured according to the ZFC/FC protocols, we can note that TRM measurement is closer to the FC one but with no applied field during the warming up of the sample. While the remanence obtained from the isothermal remanence magnetization (IRM) measurement is comparable to the ZFC protocol. The remanences from IRM and

TRM represent the irreversible contribution, thus M ZFC and MFC can be written as :

$$M_{ZFC}(H, T, t) = M_{rev}(H, T) + M_{IRM}(H, T, t) \quad (2.16)$$

$$M_{FC}(H, T, t) = M_{rev}(H, T) + M_{TRM}(H, T, t) \quad (2.17)$$

From eq (2.16) and eq (2.17) we can write:

$$M_{TRM}(H, T, t) = M_{FC}(H, T, t) - M_{ZFC}(H, T, t) + M_{IRM}(H, T, t) \quad (2.18)$$

For an ensemble of nanoparticles MIRM can be negligible, accordingly eq (2.18) can be simplified to:

$$M_{TRM}(H, T, t) = M_{FC}(H, T, t) - M_{ZFC}(H, T, t) \quad (2.19)$$

For non-interacting system, the distribution of the anisotropy energy barrier can be then estimated from (  $M_{FC} - M_{ZFC}$  ) curve:

$$\mathcal{F}(\Delta E) \propto - \frac{d(M_{FC} - M_{ZFC})}{dT} \quad (2.20)$$

#### 2.3.4 Remanence Plot Technique

Isothermal remanent magnetization (IRM) and direct current magnetization (DCD) protocols are two effective tools to investigate interparticle interactions. IRM protocol starts with a sample in a demagnetized state, a positive and small magnetic field  $H$  is applied for a short time, which is then removed and  $M_{IRM}(H)$  is measured at zero field. This experimental process is repeated by increasing the

applied field until the remanence takes the saturation value. In DCD measurement, we start from a saturated sample, then a small field in the opposite direction of magnetization is applied for few seconds, the field is switched off and  $M_{DCD}(H)$  is measured. The process is repeated until the sample reaches the saturation in the opposite direction increasing the magnetic field.

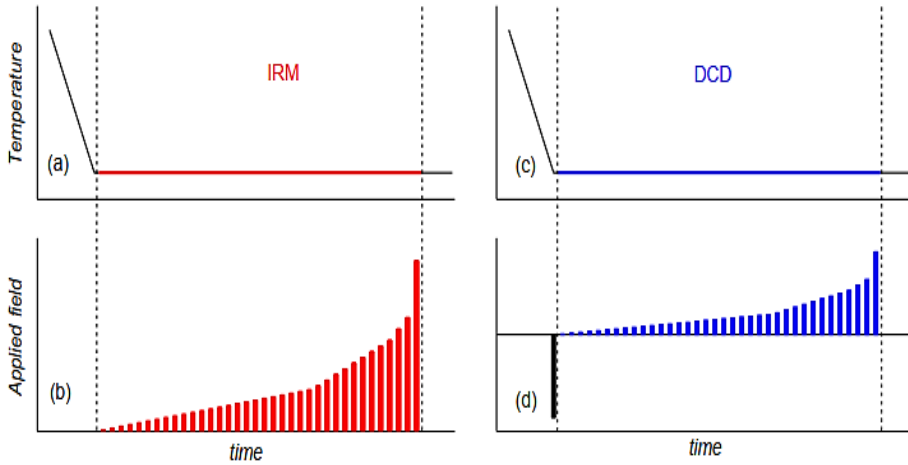


**Fig.2.9:** Schematic presentation of (a and b) IRM and (c and d) DCD experimental protocols

The derivative of the remanence curves with respect to the magnetic field  $H$  represents the irreversible susceptibility, or susceptibility of the irreversible magnetization [13]:

$$\chi_{irr} = \frac{dM_r}{dH} \quad (2.21)$$

$\chi_{irr}$  can be considered as a measure of the energy barrier distribution, which is in a real system of nanoparticles the energy barrier distribution is associated with a distribution of particles' coercivities, generally called switching field distribution (SFD). The remanence coercivity in IRM is defined as the field where IRM curve reaches its half maximum value and as the field where DCD is equal to zero, which corresponds to the maximum of the maximum of SFD.

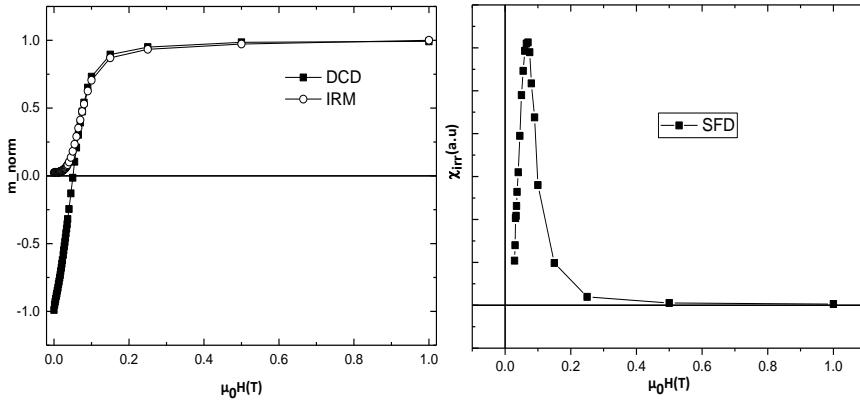


**Fig.2.10:** An example of (a) DCD and IRM curves (b) SFD from DCD curve of FeO sample.

For non-interacting single-domain particles with uniaxial anisotropy and magnetization reversal by coherent rotation, the IRM and DCD curves are related via the Wohlfarth equation [49]:

$$m_{DCD}(H) = 1 - 2m_{IRM}(H) \quad (2.22)$$

where  $m_{DCD}(H)$  and  $m_{IRM}(H)$  represent the reduced terms  $M_{DCD}(H)/M_{DCD}(H_{max})$  and  $M_{IRM}(H)/M_{IRM}(H_{max})$ , with  $M_{DCD}(H_{max})$  and  $M_{IRM}(H_{max})$  being the remanence values for the DCD and IRM curves for a large reversal field  $H_{max}$  capable of fully saturate the sample. Kelly et al. [50] have proposed :

$$\Delta M = m_{DCD}(H) - 1 + 2m_{IRM}(H) \quad (2.23)$$

The plot is equal to zero and deviates from this value in case of interactions: positive or negative deviations are indicative of the presence of interactions promoting the magnetized (e.g. exchange interaction) or demagnetized state (dipolar interaction), respectively.

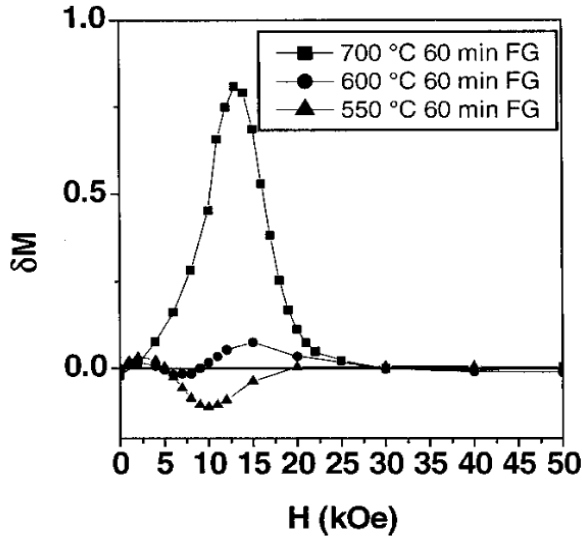


**Fig.2.11:**  $\delta m$  plots of annealed FePt nanoparticles, showing the evolution of the nature and strength of magnetic interparticle interactions [51].

## 2.4 Mössbauer Spectroscopy

Mössbauer spectroscopy is a nuclear technique with sufficient energy resolution to resolve the hyperfine structures of nuclear levels. It allows to probe the local electronic structure and, by extension, the local crystallographic, magnetic and chemical environments. The key to the success of this technique is based on the discovery that gamma radiation that can be emitted and absorbed in a resonant manner without recoil in solids, i.e. without any energy loss for the lattice. In a given experiment, the resonant absorption of  $\gamma$ -rays, emitted from a radioactive nucleus, by nuclei identical to those of the ground state of the emitting nucleus is measured. More than 45 isotopes, have a large enough Mössbauer effect to be measurable, among them the most used one is  $^{57}\text{Fe}$  that due to its very low energy gamma-ray and long-lived excited state. In the presence of a magnetic field, the nuclear spin moment experiences a dipolar interaction with the magnetic field, i.e., Zeeman splitting induced from a magnetic field at the nucleus ( $B_{hyp}$ ). In presence of external field, total effective magnetic field at the nucleus,  $B_{eff}$  is given by:  $B_{eff} = B_{ext} + B_{hyp}$ .

The shift of the isomer ( $\delta$ ) comes from the interactions between the nuclear charge and the electron charge density. The monopole interaction has altered the nuclear energy levels and so any difference in the s-electron environment between the source and absorber produces a shift in the resonance energy of the transition. This shifts the entire spectrum positively or negatively depending on the density of s-electrons. As an example, the isomer shift gives an idea about the valency states and ligand bonding states. When a nuclei have a non-spherical charge distribution produces an electric quadrupole interaction. The presence of an asymmetrical electric field can split the nuclear energy levels of the excited states, can result in shifts of the lines of the Mössbauer spectra, called quadrupole shift ( $\epsilon$ ).

In case of ferrites and under an applied magnetic field, the Mössbauer spectrum show magnetic splitting of the tetrahedral site increases and the octahedral site splitting decreases, allowing to distinguish iron ions located in different interstitial sites.

In addition ,if the obtained spectrum shows that the second and fifth lines have a non-zero intensity, they evidence a non-collinear structure for iron magnetic moments with respect to the applied field [52,53]. In the case of a non-collinear spin structure, the measured effective nucleus field ( $B_{\text{eff}}$ ) differs from the external field ( $B_{\text{ext}}$ ) due to the average canting angle  $\vartheta$  as graphically illustrated in **Figure 2.12**.

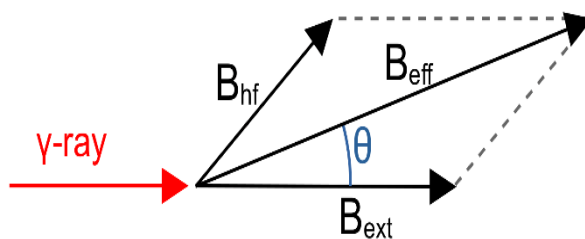


**Fig.2.12:** A sketch of the geometrical arrangement of the setup for  $^{57}\text{Fe}$  Mössbauer spectroscopy and the relation between the hyperfine field ( $B_{\text{hyp}}$ ), the measured effective nucleus field ( $B_{\text{eff}}$ ), and the external field ( $B_{\text{ext}}$ ), forming the average canting angle  $\vartheta$ .

For a thin sample, where thickness effects are negligible and where the direction of the hyperfine field is at random with respect to the  $\gamma$ -ray direction, the relative area of the Zeeman sextet are in the ratio:

$$3: 2p: 1: 1: 2p: 3 \quad (2.24)$$

where  $p$  is dependent on the canting angle  $\vartheta$ :

$$p = \frac{2 \sin^2 \theta}{1 + \cos^2 \theta} \quad (2.25)$$

By normalizing the total area to 1, the area of lines 2-5 ( $A_{2,5}$ ) is equal to:

$$A_{2,5} = \frac{1}{2} \sin^2 \theta \quad (2.26)$$

In the absence of canting effects, lines 2-5 disappear. On the other hand, from their residual intensity, the corresponding average canting angle  $\vartheta$  over the entire particle is determined [52]:

$$\theta = \arcsin \sqrt{2A_{2,5}} \quad (2.27)$$

## 2.5 infrared spectroscopy (IR)

Infrared spectroscopy or vibrational spectroscopy is a powerful tool to study and identify chemical substances or functional groups in solid, liquid or gas form. It measures the interaction of electromagnetic waves with matter by absorption, emission or reflection. IR exploits the absorption of molecules at frequencies characteristic of their structure, which occurs at a resonance frequency (i.e. the frequency of the adsorbed radiation is equal to the vibration frequency of the structure). We can distinguish two main modes of vibration: the stretching modes (involving 2 categories) and the bending modes (involving 4 categories). our samples were characterized with a Shimadzu IRPrestige-21, equipped with a Specac golden gate single reflection diamond attenuated total reflection. All

samples are analyzed in the region between 4000  $\text{cm}^{-1}$  and 450  $\text{cm}^{-1}$  and Fourier transform was used as a data-processing technique [54]. Most of the experiment reports in this thesis has been done by an Attenuated Total Reflectance (ATR) device the powders are deposited on a prism made of a material with a high refractive index for all infrared radiations (as a diamond).

## 2.6 X-ray Absorption Near-Edge Structure (XANES) spectroscopy

X-ray Absorption Fine Structure (XAFS) spectroscopy is a chemically selective powerful technique to study the properties of local atomic structure around the absorbers. In particular the near edge region (XANES) of the absorption spectrum is strongly sensitive to the oxidation state and coordination chemistry of the absorber, and can provide accurate chemical speciation in multi-phase compounds [55].

Fe K-edge (7112 eV) XAFS measurements were carried out at the XAFS beamline of the ELETTRA synchrotron [56]. X-ray absorption spectra were measured in transmission geometry at room temperature, measuring the X-ray intensities before ( $I_0$ ) and transmitted ( $I_t$ ) through the sample using two gas optimized ionization chambers. An Fe metal foil is placed after the  $I_t$  detector and a third ionization chamber measured the transmitted X-ray flux ( $I_{ref}$ ) which is used to monitor the X-ray energy calibration during the experiment. XAFS samples were prepared by mixing a small amount of MNPs powder with polyvinylpyrrolidone (PVP) polymer in approximately 1/10 weight concentration. About 100 mg of the mixtures were compressed in thin solid pellets suitable to be mounted on the sample holder by Kapton tape. To improve the data statistics and reduce artefacts due to X-ray beam drifts, at least three scans were collected for each sample and averaged after checking for the correct energy scale. In addition, Fe-K edge spectra from commercial reference compounds were measured, in particular pure Fe metal foil, FeO, Fe<sub>3</sub>O<sub>4</sub> and  $\gamma$ -Fe<sub>2</sub>O<sub>3</sub> oxide powders, in order to

be used as standard references for Fe<sup>0</sup>, Fe<sup>2+</sup> and Fe<sup>3+</sup> oxidation states. The total absorption signal through the sample was calculated as [57]:

$$a(E) = \ln\left(\frac{I_0}{I_t}\right) \quad (2.)$$

The raw absorption spectra  $a(E)$ , of NP and reference samples were processed for pre-edge background subtraction and post-edge jump normalization accordingly to standard XAFS data analysis procedures and analyzed in the XANES region using a Linear Combination Fit procedure using the Athena program.

## Nanoarchitecture Based Hybrid Materials: Design the Magnetic Properties

The desire for new functions and the improvement of technological innovations generate an enormous demand for new functional materials with tunable properties and improved performances. Scientists have demonstrated that by combining attributes of different classes of materials in one system is an efficient way to obtain new properties compared with their pure counterparts [58]. This strategy allows the emerging of new promising and potent class of materials so called hybrid-materials with a new world of diverse and complementary behaviors inherent of this class, where the diversity of the emerged properties leads to a very wide novel range of application areas. By applying this approach one can find many examples of hybrid materials that have been emerged during the last decades. For example, in a study of core-shell magnetic hybrid materials, the authors reported a significant effect resulting from the coupling of one ferro/ferri-magnetic material with another antiferromagnetic one, called the exchange bias phenomenon [59]. In other cases, an enhancement of the effective magnetic anisotropy energy and an increase of the blocking temperature ( $T_B$ ) have been observed as a result of the combination of two different phases [60].

Looking in the complete class, magnetic nanoparticles-based hybrid materials have been considered as a promising material for fundamental scientific discovery and for efficient technological applications. Since, after hybridization, the spin-orbit coupling at the interface between a magnetic and non-magnetic materials and the symmetry breaking at the nanoparticle surface (coming from the decrease in particle size) can be affected, which leads to a property of the resulting magnetic-hybrid material as a sum of individual contributions of each phase or/and an emerge of novel magnetic properties.

In order to cover several aspects, this chapter is divided into sections: The first section present a revision of the state of the art of the research on multifunctional magnetic hybrid nano-materials in literature and we continue with proposing new classification to magnetic nano-hybrid materials. Then we follow with synthesis of the magnetic nanoparticles and investigates the influencing factors in the synthesis process. A description of spinel iron oxide nanoparticles-mesoporous silica system: combination of the properties, is also reported. The last section is devoted to investigate the new magnetic properties result from combining magnetic phase with other phase to form a hybrid material: case of crystalline/amorphous cobalt ferrite nanocomposite.

### 3.1 Definition and classification

Magnetic nano-hybrid (-composite, -heterostructures) (MNH) is a material composed of two or more distinct phases in which at least one of phases has a long-range magnetic order, (e.g. FM, FiM or AFM). At nanoscale, terms composite and hybrid are synonyms since the chemical bounds or interactions between two phases are unavoidable. This bonding leads to the achieving new properties of hybrid material which do not presented in a simple mechanical mixture of components [61]. In literature it is more common under term MNH designate material composed from magnetic transition metal based oxide or metal component coupled with plasmonic noble metal [62,63], diamagnetic organic [64,65], functional carbon/graphene [66,67] or silica [68] counterpart in form of nanoheterostructures. The main distinctive feature of listed combination is their multifunctionality. Recently, a lot of attention was devoted to synthesis of multifunctional MNH combining structural, optical, mechanical, rheological,

catalytical properties. M. Farle predicted new and perspective directions where MNH find application:

- Spintronics using organic and inorganic magnetic building blocks down to the molecular level.
- Spin "nano" processing for energy saving magneto-logic devices and microprocessors based on spin-dynamics.
- Magnetic storage materials using three dimensional self-assembled hierarchies.
- Materials for magnetic refrigeration.

In literature presented several classifications of nanohybrids (no specified for magnetic) by different factors [69,70] , such as by morphological characteristic:

- **0-D**, core-shell, dumbbell-, Janus-like, encapsulated mesoporous and hollow nanoparticles of different shapes.
- **1-D**, nanowires or nanotubes covered, partially covered, encapsulated or decorated with nanoparticles.
- **2-D**, nanostructured and nanopatterned thin films, multilayer thin films, nanoplates and microdisc.
- **3-D**, bulk matrix filled with 0-, 1- and 2-D nanostructures including hierarchical and self-assembled structures (**Figure 3.1**).

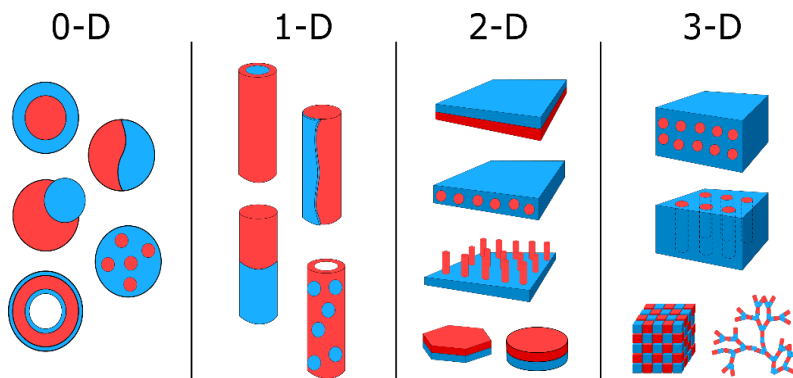


**Fig. 3.1:** Morphological classification of two-phase systems.

In follow we propose new and specified classification of magnetic nano-hybrid materials:

**Multimagnetic nanohybrids** consisted of two or more magnetic materials with different magnetic order (i.e., ferro(i)magnetic, antiferromagnetic) or different anisotropy. Indeed, exchange coupling of magnetic materials represent an interesting tool to change magnetic properties (i.e., saturation magnetization, magnetic anisotropy) of the final material. This approach is wide investigated to design new generation of permanent magnets with improved maximum energy product,  $(BH)_{\max}$  [71–73]. Magnetic phases with high anisotropy usually have relative low saturation magnetization and Curie temperature. Coupling with a magnetically hard phase with magnetically soft results in hysteresis with higher performance. Theoretically  $(BH)_{\max}$  value of exchange-spring magnet can exceed in about three times commercially available permanent magnets and reach  $954.93 \text{ KJ/m}^3$  [73].

One of the key issues in designing the multimagnetic nanohybrids is control of the magnetization reversal process. Depending on size of layers (or grains) this process can occur simultaneously in both magnetic phases or each phase can reverse independently. The first type of the reversal magnetization process, in rigidly coupled MNH is characterized by smoothed hysteresis while the second by two-steps hysteresis with a nucleation field ( $H_N$ ) related to magnetization reversal processes of soft phase. The critical size of the soft layer ( $t_s$ ) where happens the switching from the first to the second mechanism equals twice the width of a domain wall in the hard phase [73]:

$$\delta_h = \pi\sqrt{A_h/K_h}, \quad (3.1)$$

where  $A_h$  and  $K_h$  are the exchange and anisotropy constants of the hard phase, respectively. This picture is well explained, by Muscas et al. in a nanocomposite combining nanoparticles  $\text{La}_{0.67}\text{Ca}_{0.33}\text{MnO}_3$  (LCMO) and  $\text{CoFe}_2\text{O}_4$  (CFO) oxides. M vs H curves recorded at 5K, **Figure 3.2**, show a loop shape close to a simple superposition of the hysteresis loops of the pure CFO and LCMO phases.

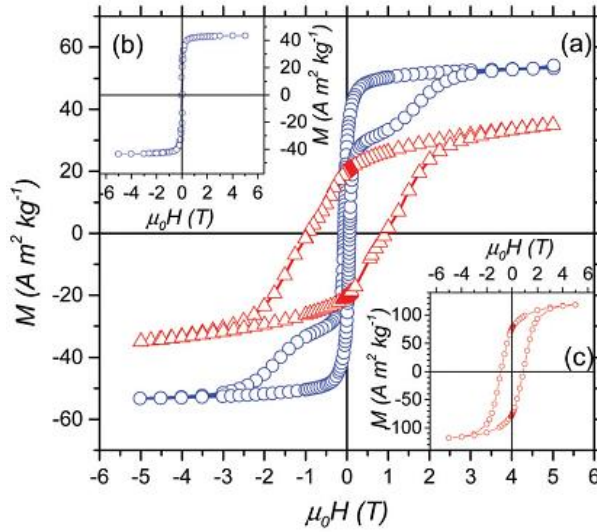


**Fig.3.2:** M vs. H curves of (a) blue circles present the hysteresis of mixed LCMO (prepared by Sol-Gel) and CFO (prepared by polyol), and red triangles present the hysteresis of LCMO/CFO nanocomposite prepared by a seed mediated growth self-combustion method. (b) LCMO and (c) CFO single phases reported for comparison [74].

**Magnetic/non-magnetic nanohybrids** magnetic/non-magnetic MNH consisted of ferro(i)magnetic phase covered, coupled with non-magnetic shell or encapsulated in matrix or layered structures. This class of MNH is probably one of the most investigated class of MNH because of native multifunctionality and vivid difference in physical properties of counterparts. Remarkable example of application of Class II MNH is biomedicine [65]. Here, coupling of magnetic phases with non-magnetic carried to combine magnetic properties with bio-functions (i.e., drugs, gens, enzymes, etc.), biocompatibility of silica, gold or polymers; or to add particular optical properties of semiconductor quantum dots. In biomedical application, magnetism can be applied for magnetic hyperthermia treatment or MRI diagnostics purposes, while the second phase, for example, plasmonic one for additional bioconjugation and the optical sensing [62,75]. To date several chemical synthetic strategies to synthesize MNH in form of core/shell, dumbbell-like and nanoflower nanoparticles of different sizes and shapes have been investigated [76,77].

Specific representatives of the magnetic/non-magnetic class are composite multiferroics, materials consisted of several phases with different ferroic order, for example, magnetoelectric multiferroics combined FM(i) or AFM with ferroelectric natures [78,79]. Coupled magnetism and electricity in one material give rise to unique physical phenomenon, such as electric-field control of magnetism, in particular, control of exchange bias, reversal of FM(i) and AFM domains. Those phenomena have a great potential in spintronics and in completely new fields such as electrically-controlled antiferromagnetic spintronic and domain-wall electronic [80,81]. From another side, switching of the electrical polarization of a multiferroic material by magnetic field is applicable in magnetic field sensors and in artificial biological interfaces. Synthetic hybrid multiferroics are more efficient than natural such as for example BiFeO<sub>3</sub>. Artificial multiferroics were produced in form of core/shell nanoparticles [82], multilayer thin films [83], nanocomposites [84], piezo-polymeric-based [85] and three-component [86] composites.

**Topological nanohybrids** topological MNH is the class of material where the second phase is surface which could be of the same chemical composition. The Class is composed by material with the strong influence of surface spins. Hybrids of this class can be chemically homogenous but because of the surface spins forming a magnetically anomalous region can be considered as two-phase system. In magnetic nanostructures, the strong influence of surface manifest in reduction of saturation magnetization and increased anisotropy [87,88]. As an example of this class of MNH we can find the hollow nanoparticles, because in this case the influence of surface is doubled (i.e., there is internal and external surfaces). The typical magnetic hysteresis of such particles is usually characterized by high coercive field and larger reduced remanent magnetization [89]. An example of this Class was described by Elias Ferreiro-Vila and colleagues who investigated CoFe<sub>2</sub>O<sub>4</sub> thin film prepared via a chemical solution and pulsed laser deposition methods. By variation of such parameters as temperature and epitaxial stress, they showed that the Co<sup>2+</sup> cations can migrate from octahedral to tetrahedral sites of spinel structure of CoFe<sub>2</sub>O<sub>4</sub> in strained layer [90]. This leads to drastically dropping of anisotropy in this layer which was confirmed by

appearance of two-phase-like M vs H hysteresis loops. Thus, in this case the surface layer having the same chemical composition, but different structural/microstructural properties act as a second magnetic phase.

**Interface nanohybrids** MNH with special magnetic phenomenon arise on interface between two magnetic or non-magnetic phases. Interface nanohybrid Class is MNH with strong influence of interface between two phases on magnetic properties of whole system with phenomenon arise because of contribution of interphases spins. In case of two magnetic phases, when the interface coupling constant  $J_{\text{int}}$  is less than  $K_{\text{hth}}$  ( $J_{\text{int}} < K_{\text{hth}}$ ), a very important phenomenon of the exchange bias (EB) can be observed [59]. In M vs H hysteretic measurements this phenomenon is displayed by the shift of hysteresis after induction of the preferential orientation of pinned spins on interface between two phases. Important requirement to observe bias is the significant difference in anisotropy constant between two magnetic phases and more pronounced become in the case of antiferromagnetic and ferro(i-)magnetic systems. The EB phenomena was firstly discovered in a system of FM/AFM core/shell nanoparticles by Meiklejohn and Bean [91], who observed a horizontal shift of hysteresis loop after cooling through the AFM Néel temperature,  $T_N$  (in system with  $T_N$  of AFM lower than the FM Curie Temperature,  $T_C$ ) in the presence of an applied magnetic field. The observation of such phenomenon has been then extended to interfaces between FiM and AFM as well as in FM/FiM [92,93] and AFM/AFM [94,95] systems. The key distinguishing feature of such systems is a family of interface spins with broken symmetry of exchange interaction which become pinned at certain temperature and act as an anchoring layer. The exchange bias in multilayered MNH of the Class IV is the crucial phenomenon lied in the base of devices in spintronics based on magnetoresistance, in particular the giant magnetoresistance [96].

The interface in nanostructures represents very rich on unexpected properties area. Besides fundamental exchange bias phenomenon there where observed many important and fundamental findings. For example, unprecedented in bulk appearance of ferromagnetism in non-magnetic materials. Several researcher

group confirmed ferromagnetic state of  $Ti^{3+}$  ions at interface in  $LaAlO_3/SrTiO_3$  heterostructures [97]. Room temperature magnetism was observed at interface of two antiferromagnetic cobalt oxides  $CoO/Co_3O_4$  attributed to a strained lattice configuration of this interface [98]. The orbital paramagnetism of Au with the large orbital/spin magnetic moment ratio ( $m_{orb}/m_{spin} = 0.38$ ) in magnetite-gold MNH [63]. This phenomenon was attributed to spin-polarization transfer across magneto-plasmonic interface via direct hybridization between the Au and Fe states.

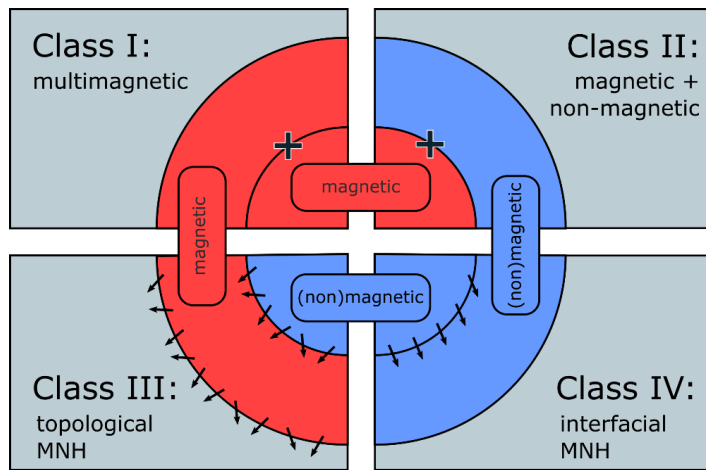


**Fig.3.3:** Classification of magnetic nanohybrids.

### 3.2 Iron Oxides with spinel structure

In the last decades, iron oxides with spinel ferrite nanoarchitectures have gained huge attention in fundamental science and in technological applications such as high-density data storage, catalysts, gas sensors, microwave absorbers and medical diagnostics and therapy [99–103] etc. Understanding the crystal chemistry of spinel ferrite is very important, as it can improve/control the physical and chemical properties of nanomaterials. Spinel iron ferrites have the general formula  $MFe_2O_4$  where  $M = Mn, Fe, Co, Ni, Cu,$  and  $Zn$ . The distribution of cations [104] in the structure is generally based on several parameters such as the size of the interstitial site, the ionic radii of the metal cations, the conditions

of the synthesis reaction, etc. At nanoscale regime, the decrease in crystallite size and the increase of the specific surface area lead to a significant improvement in the nanomaterial features (i.e., structural, magnetic, optical properties). Accordingly, a good control of the size and the shape by choosing the appropriate synthesis route, can allow to modulate the physical and chemical properties of spinel ferrites. Various chemical methods for the synthesis of spinel ferrites have been studied in the literature [105–107], but from our point of view, the design of new nanomaterials with simple synthesis methods based on inexpensive and less hazardous precursor materials needs more attention to fulfil the requirements for the commercially reliable methods. In the following, we give an overview of the spinel structure and its correlation with magnetic properties, with particular attention to the in-depth study of spinel iron oxides synthesized by co-precipitation method [108].

### 3.2.1 Crystalline Structure

Spinel ferrites crystallize in a face-centered cubic lattice with the space group F3dm [109]. The crystal structure consists of 32 oxygen atoms in close-packed arrangement, and the remainders are metal cations occupying 8 from 64 tetrahedral (A) sites and 16 from 32 available octahedral (B) sites. The cation distributions in both types of interstices can be represented by  $[M_{1-\delta}^{2+} Fe_{\delta}^{3+}]_A [M_{\delta}^{2+} Fe_{2-\delta}^{3+}]_B$ . The inversion degree,  $\delta$  defined the fraction of A or B sites occupied by  $Fe^{3+}$  or  $M^{2+}$  cations respectively. If  $\delta = 0$ , this corresponds to normal spinel ferrite structure. In case  $\delta = 1$ , the ferrite is called inverse spinel. If  $0 < \delta < 1$ , we are in the case of partially inverted or mixed spinel ferrites, where both  $Fe^{3+}$  and  $M^{2+}$  cations are distributed on both sites. The preference of sites from the different ions depends mainly on the relative ion size and the lattice site size. Divalent ions, due to their large charge, they occupy larger site. Hence in case of an inverse spinel structure it would be reasonable that divalent ions would go into the octahedral site and trivalent ions would go into tetrahedral site. Therefore, any change in  $\delta$ , then in the cationic distribution, leads to a significant change in the physical properties of the ferrites [104].

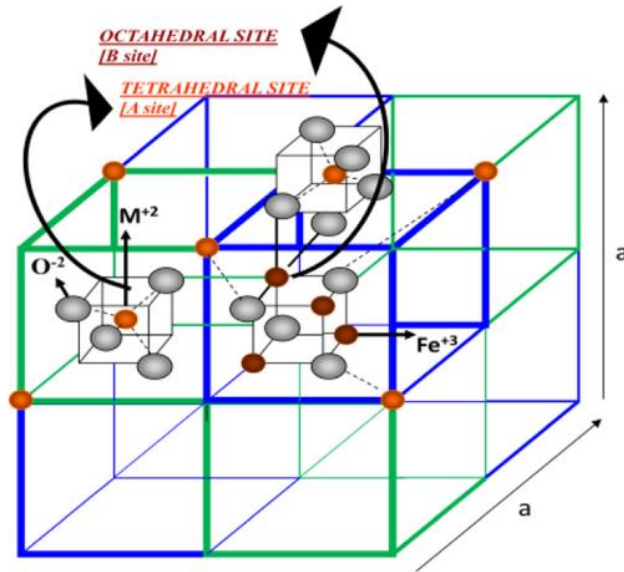


Fig. 3.4: Crystal structure of cubic ferrite[110].

### 3.2.2 Magnetism in spinel ferrites

The magnetic behavior associated with spinel ferrites is governed by the magnetic super-exchange interactions that occur between spins of the metallic cations in A- and B-sites through the intermediation of oxygen ions. These interactions are of three types:  $J_{A-B}$ ,  $J_{A-A}$  and  $J_{B-B}$  interactions. It is to be noted that the strongest, negative interaction is A-B for which the distances between the cations and the oxygen ion that link them are small and the values of bond angle are high. While the B-B interaction is intermediate between the A-B and A-A interactions [111]. The net moment in case of inverse spinel structure is only due to the magnetic moment of the divalent cations because of the antiparallel arrangement of the two sublattices. Then, changing the cationic distribution (quantified by the inversion degree) in interstitial sites of the spinel structure, can influence their magnetic properties, e.g. saturation magnetization as well as the magnetic anisotropy. The variation of the anisotropy with the relative occupancy of A- and B-sites by the cations can be expressed by [112,113]:

$$K = (1 - \delta) K_{M^{2+}}^A + \delta K_{Fe^{3+}}^A + \delta K_{M^{2+}}^B + (2 - \delta) K_{Fe^{3+}}^B \quad (3.2)$$

$K_{M^{2+}}^{A,B}$  and  $K_{Fe^{3+}}^{A,B}$  are the anisotropy constants of  $M^{2+}$  and  $Fe^{3+}$  at A- and -B sites. A study reported by C.Cannas et al. , shows that the reduction of anisotropy constant of cobalt ferrite–silica nanocomposites, is due to a high percentage of  $Co^{2+}$  in tetrahedral sites, which can be explained by the smaller single ion anisotropy for  $Co^{2+}$  located in tetrahedral sites compared to  $Co^{2+}$  in octahedral sites [114].

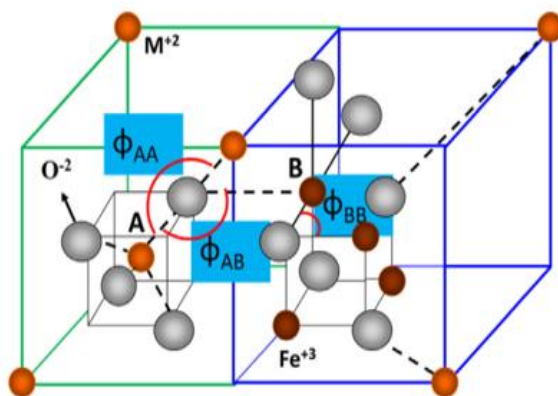


Fig. 3.5: Schematic representation of super exchange interaction [110].

### 3.3 Designing spinel ferrite nanoparticles magnetic core: Co-precipitation

Co-precipitation is one of the chemical methods used for nanoarchitectures preparation, based on the precipitation of one or more metals together with the support of a base [20,115–117]. Co-precipitation is very attractive method due to the high reaction yielding. On the other hand, this method is often considered to be more difficult since it needs an accurate control of the experimental conditions. The operation can be performed through two different modes, direct or reverse co-precipitation (i.e., adding the base to the acidic metal solution or vice versa, respectively). The preparation of co-precipitated particles is carried

out in three major steps: liquid mixing, nucleation and crystal growth to established the basic properties of the final product.

Typically, the nucleation and the growth are proceeded simultaneously. The nucleation is strongly dependent on the concentration, As illustrated in **Figure 3.6**, for low supersaturation levels, the nucleation process is slow and the growth is more quickly, that can lead to a large size distribution. At high supersaturation levels, the growth is very slow and the nucleation is dominating. Thus, higher supersaturation is required for dispersed coprecipitates through the rapid mixing of the concentrated solutions. A drawback of the co-precipitation process is the generation of large quantities of salt solutions that can lead to low stability.

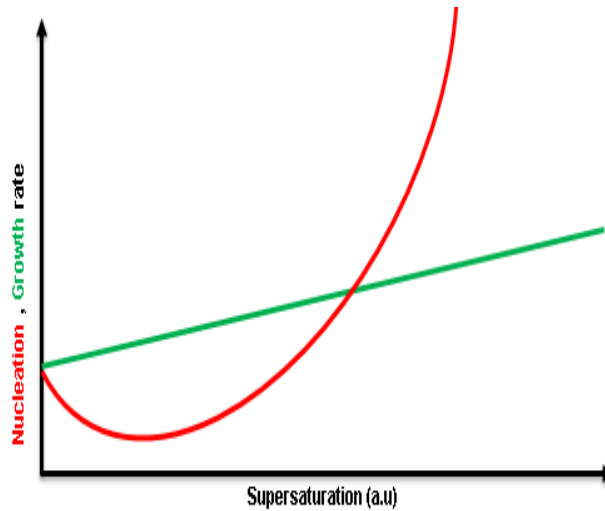


**Fig. 3.6:** Schematic representation of nucleation, growth rate versus supersaturation.

### 3.3.1 Synthesis Process

Spinel iron oxide nanoparticles were prepared by coprecipitation method. Experiments were carried out at 60 °C, under homogeneous magnetic stirring in a glass reactor contain 100ml of 0.01M HCL solution, equipped with a gas inflow port (for the nitrogen), and a port for the addition of 6.2 mmol of  $\text{FeCl}_3 \cdot 6\text{H}_2\text{O}$  and 3.15 mmol of  $\text{FeCl}_2 \cdot 4\text{H}_2\text{O}$  precursors. After one hour 20 ml of  $\text{NH}_3$  solution was deoxygenized and added abruptly to the iron salt solution. 60 min after the base

addition, the resulting precipitate was removed and washed for several cycles with deionized water then dried at 60 C° overnight, (**Figure 3.7**).

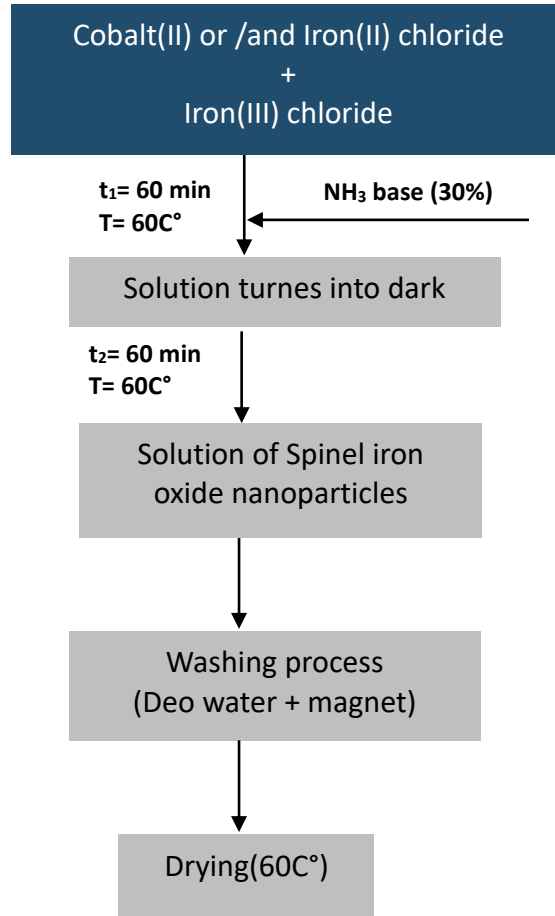


**Fig. 3.7:** Synthesis process of nanoparticles.

### 3.3.2 Temperature effect

#### 3.3.2.1 Structural Study

The obtained XRD patterns (**Figure 3.8a**) of Fe<sub>3</sub>O<sub>4</sub> prepared in controlled atmosphere(N<sub>2</sub>) and in different temperature range (25-100°C) show reflections ascribed to the crystalized spinel iron oxide structure (JCPDS card No.75-449). By using Debye Scherrer's formula a mean crystallites size between 7.0(7) to 10(1)

nm have been obtained. **Figure 3.8b**, report the size value of all the  $\text{Fe}_3\text{O}_4$  samples at different temperature estimated by Debye Sherrer's (DS) and Williamson-Hall methods (WH) [39] (details in section 2.1) .Due to the obtained equal size values of particles prepared at 25 °C and 60°C although the significant difference in the reaction temperature with Debye Sherrer's formula, we decide to more investigate the magnetic properties of these two samples in control atmosphere. The obtained samples are labeled FO-CA-25° and FO-CA-60°.

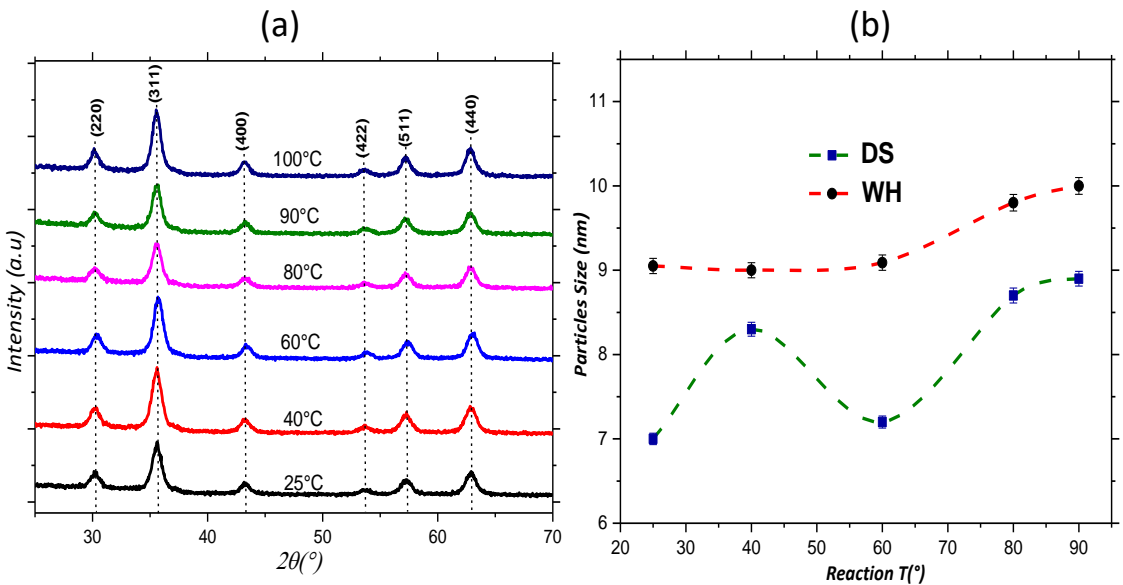


**Fig. 3.8:** (a) XRD patterns, (b) Crystallite Size from X-ray diffraction (XRD).

### 3.3.2.2 Magnetic Properties and Interparticle Interactions

Field dependence of magnetization (details in section 2.3) has been investigated at 5 K and 300K (**Figure 3.9**). At low temperature, the saturation magnetization, similar to bulk value ( $\sim 90 \text{ Am}^2\text{Kg}^{-1}$ ) [118], is the same for both samples, within the experimental error, values are summarized in **Table 3.1**. In addition, room

temperature magnetization measurement (Figure 3.9b), show superparamagnetic behavior for FO-CA-25° and FO-CA-60° samples.

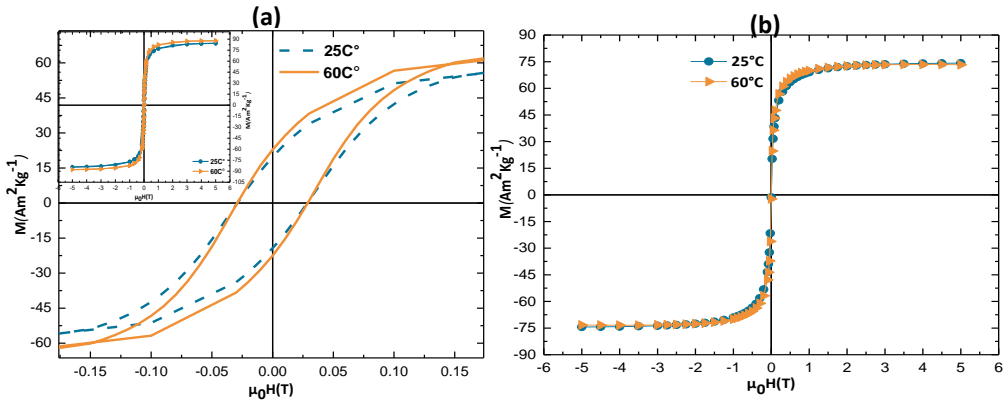


**Fig.3.9:** M vs H measured at (a) 5K and (b) 300K for 25°C (blue color) and 60°C (orange color).

**Tab.3.1:** Saturation magnetization ( $M_s$ ) at 5K and 300K, coercive field ( $H_c$ ).

Sample	$H_c$ (mT)	$M_s$ ( $\text{Am}^2\text{Kg}^{-1}$ ) 5K	$M_s$ ( $\text{Am}^2\text{Kg}^{-1}$ ) 300k
FO-CA-25	25 (2)	85 (8)	75(7)
FO-CA-60	28(2)	88(8)	70(7)

The temperature dependence of magnetization has been recorded according to ZFC-FC protocols at 2.5 mT, Figure 3.10a (details in section 2.3.2). Comparing with the samples synthesized at 25°C, a deviation to low temperature of the FO-CA-60 was observed. The shift to low temperature suggesting that the variation in the reaction temperature lead to a change in the interparticle interactions within the samples.

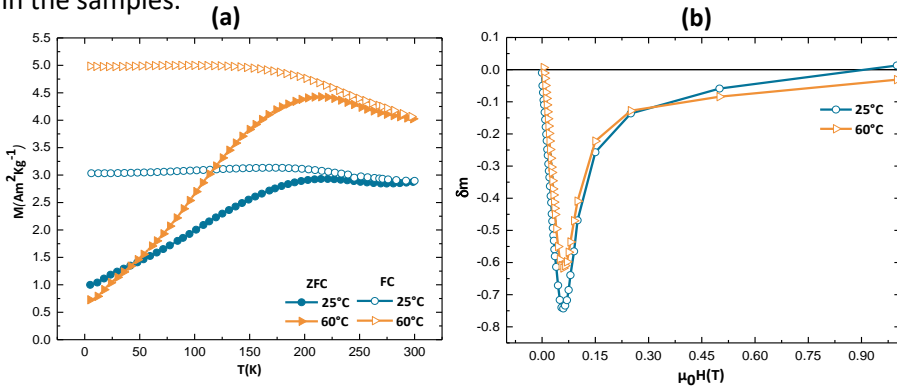


**Fig.3.10:** (a) ZFC-FC magnetization curves (b)  $\Delta m$  plots.

The type and the strength of interparticle interactions have been studied through  $\delta m(H)$  plots at 5K according to DCD (Direct Current Demagnetization) and IRM (Isothermal Remnant Magnetization) protocols of the two FO-CA nanoparticles at 25°C and 60°C (Figure 3.10b) (details in section 2.3.4) . The resulting  $\delta m$  curves for FO-CA-25 and FO-CA-60 samples confirm the presence of strong dipolar interactions which are higher in case of FO-CA-25. Based on the obtained results, the sample synthesized at 60°C has been chosen to be used for further investigations.

For further investigation of the interparticle interactions within the samples, a mean value of the interactions field ( $H_{int}$ ) is calculated [119]:

$$H_{int} = \frac{H^{DCD} - H^{IRM}}{2} \quad (3.2)$$

where  $H^{DCD}$  and  $H^{IRM}$  correspond to are the derivative of the  $m^{DCD}(H)$  and  $m^{IRM}(H)$  curves, i.e., the irreversible susceptibility:  $\chi_{irr} = dM/dH$  (Figure 3.11), that is generally refer to the switching field distribution (SFD), which is directly proportional to the energy barrier distribution in the nanoparticle ensemble [120–122] (details in section 2.3.4) . Interaction field values of -0.0149T and -0.0126T were obtained for FO-CA-25 and FO-CA-60 respectively, which reflect the change in the energy barrier distribution, reflecting the decrease in the anisotropy due to the change in the reaction temperature and confirming also the ZFC-FC analysis.

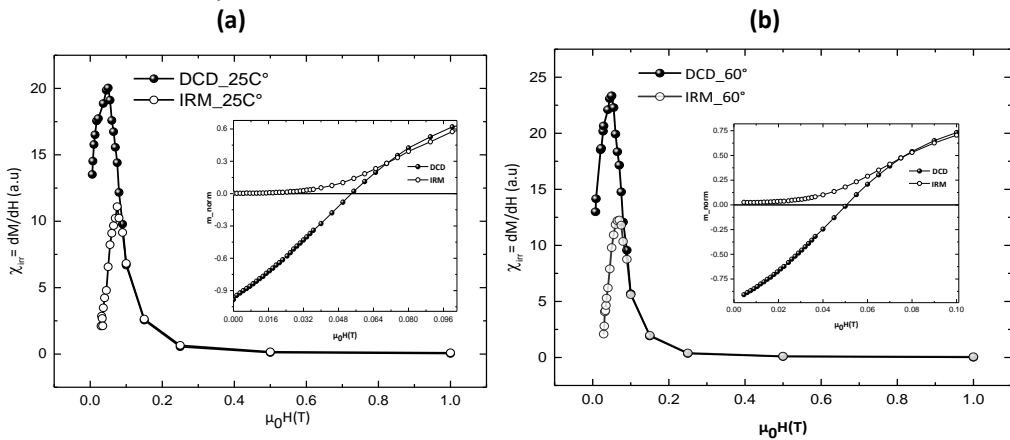


**Fig.3.11:** Irreversible susceptibility ( $\chi_{irr} = dM/dH$ ) derived by DCD (full circles) and IRM (open circles) for the sample (a) FO-CA-25, and (b) FO-CA-60, samples; insets: DCD and IRM curves.

### 3.3.3 Atmosphere effect

The motivation of the study performed on the effect of atmosphere comes from the fact that, several synthesis parameters (e.g., type of precipitating agent, stoichiometric ratio, temperature, etc.) on the chemical composition, morphology, size distribution and magnetic properties of MNPs coming from co-precipitation have been investigated, but few, and often contradictory works [123,124], on the effect of reaction atmosphere have been carried out. Accordingly, this part will focus on the effect of reaction atmosphere on the morpho-structural and magnetic properties through the multi-technique approach of spinel iron oxide nanoparticles synthesized via co-precipitation. Spinel iron oxide nanoparticles were prepared by coprecipitation method (details in section 3.3.1). To investigate the atmosphere effect, two samples of magnetite prepared under controlled atmosphere (nitrogen), FO-CA and under air, FO-NA were prepared.

#### 3.3.3.1 Morpho-structural Investigation

XRD patterns of both samples shows reflexions related to the spinel iron oxide structure (JCPDS card No.75-449), **Figure 3.12**. An average crystallite size of 9.0(9)nm was obtained for both samples by the Williamson-Hall method [38].

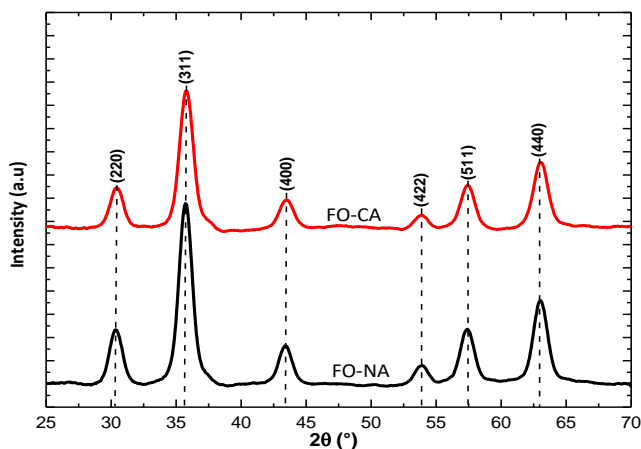


**Fig.3.12:** XRD patterns of samples synthesized in nitrogen (FO-CA, red line) and in air (FO-NA, black line).

Transmission electron microscopy (TEM) measurements (details in section 2.2) of spinel iron oxide nanoparticles prepared in nitrogen and in air reported in **Figure 3.13**, indicate the presence of aggregates of nanoparticles with mean size distribution of 9.0(9) and 11(9) for FO-CA and FO-NA respectively. High-resolution TEM (HR-TEM) observations, show a quasi-spherical shape for FO-CA particles while the FO-NA ones are faceted. Typically, in colloidal chemistry, the formation of crystals is discussed based on nucleation and growth theory [125]. It is commonly known that for the formation of monodisperse crystal, a separation of these two steps is required. However, in the co-precipitation method, the nucleation and the growth usually proceed simultaneously. Chemical phase, particle morphology and size distribution are strongly dependent on the control of the synthesis conditions, such as the pH. By controlling the value and the addition condition of the pH (e.g. continually or rapidly), different formation pathways of the nanoparticles can be observed [126,127].

In our case study, with co-precipitation, the base was added in abrupt way (i.e., pH quickly increases from 2 to 9.2), that leads to a significant pH gradient and then to the formation of lepidocrocite( $\gamma$ -FeOOH) in some zones in the pH range 7–8 [128]. After the lepidocrocite will be transformed into spinel iron oxide with the complete mixing and at higher pH. When the reaction atmosphere is the air, the presence of oxygen promoting the oxidation of  $\text{Fe}^{2+}$  ions to  $\text{Fe}^{3+}$  [129]. By changing the reaction atmosphere (nitrogen) different particles shape have been obtained. The surface structure passes from faceted in FO-NA sample to quasi-spherical for FO-CA sample. In case or air, the excess of  $\text{O}_2$  leads to higher  $\text{Fe}^{2+}/\text{Fe}^{3+}$  oxidation rate, favoring the formation  $\gamma$ -FeOOH as an intermediate then transforms into magnetite/maghemite [128]. This results in an irregularly shaped particle. On the other hand, if the reaction atmosphere is inert, the oxidation rate is slow leads to direct formation of magnetite/maghemite resulting in more spherical shape.

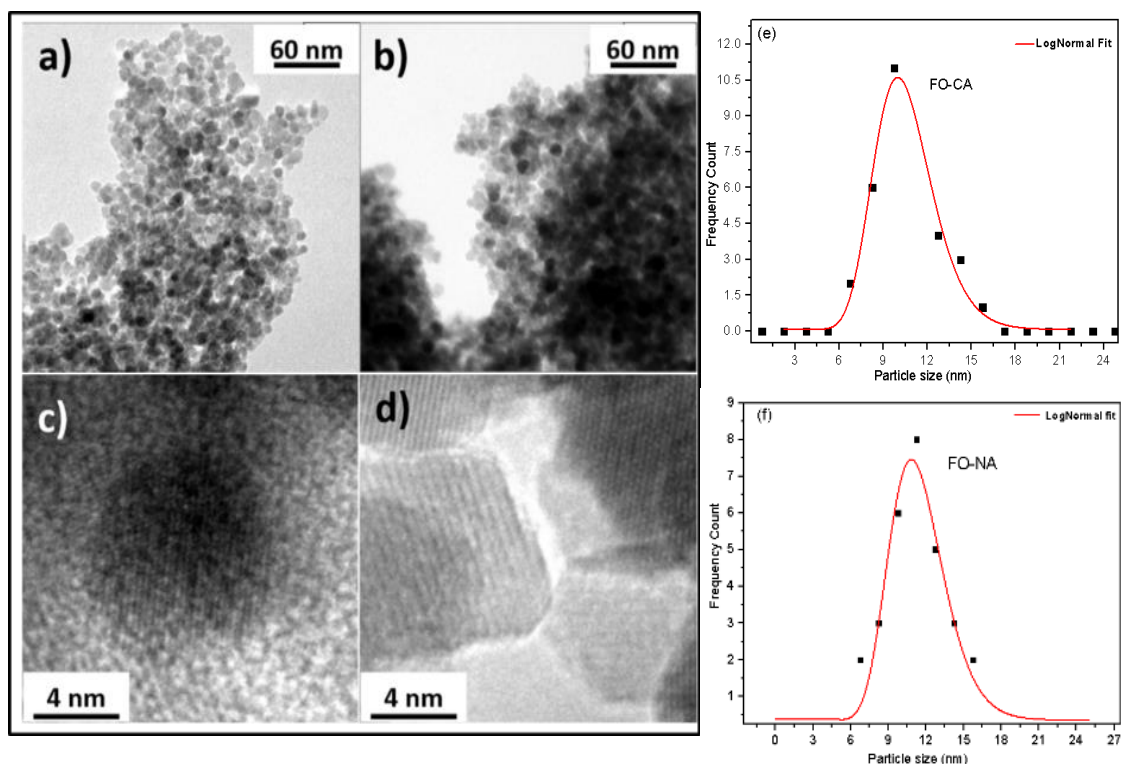


**Fig.3.13:** Bright field TEM image of (a) FO-CA and (b) FO-NA showing the nanoparticle structure of the samples. High resolution TEM image of (c) FO-CA and (d) FO-NA revealing the quasi-spherical and faceted shape of the particles synthesized in nitrogen or air reaction atmosphere, respectively, (e,f) Particle size distribution fitted with log-normal function.

Field dependence of magnetization has been reported at 300 K and 5 K, **Figure 3.14**. The obtained Saturation magnetization values, are the same within the experimental error for FO-CA and FO-NA. The high  $M_s$  values (**Table 3.2**), similar to the bulk one, confirm the good magnetic ordering of the samples. The obtained low values of reduced remanence magnetization ( $M_r/M_s$ ) and coercive field ( $H_c$ ) are typical for monodomain spinel iron oxide nanoparticles [130]. At 300 K, the two samples are in superparamagnetic regime.

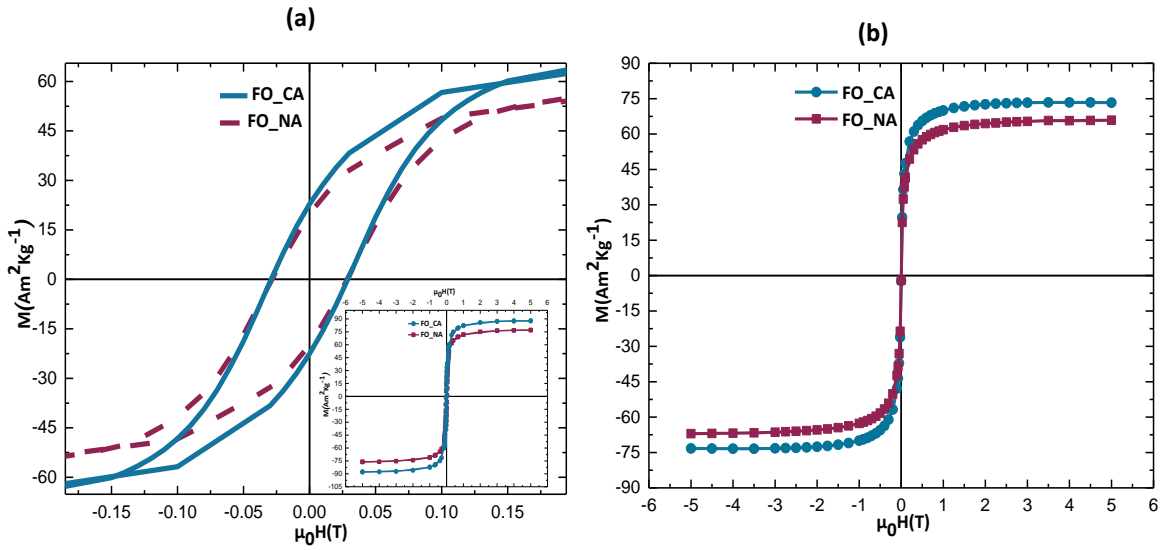


**Fig. 3.14:** M vs H measured at (a) 5K and (b) 300K under air atmosphere (violet color) and nitrogen atmosphere (blue color).

Sample	$M_s$ ( $\text{Am}^2\text{kg}^{-1}$ ) 300K	$M_s$ ( $\text{Am}^2\text{kg}^{-1}$ ) 5 K	$M_r/M_s$	$H_c$ (mT)
FO-CA	70.9(7)	88(3)	0.25	28.7(3)
FO-NA	69.4(1)	77(3)	0.25	28.1(3)

**Tab.3.2:** Saturation magnetization ( $M_s$ ) at 5 K and 300 K, reduced remanence magnetization ( $M_r/M_s$ ) and coercive field ( $H_c$ ) for FO-CA and FO-NA samples, uncertainties on the last digit are given in parentheses.

### 3.3.3.2 Magnetic Structure

The magnetic structure of the sample has been investigated by means of Mössbauer spectrometry performed at low temperature, (12 K) under intense magnetic field (8T), applied parallel to the  $\gamma$  –beam (details in section 2.4). The spectrum (**Figure 3.15**), confirm the inverse spinel structure. According to the obtained fitting parameters reported in **Table 3.3**, the low isomer shifts ( $\delta$ ) values confirm the high oxidation degree of nanoparticles in study. The non-zero intensity of the second and fifth lines reveal the presence of a canted spins with

small canting angle ( $\Theta$ ) in tetrahedral and octahedral sites suggesting the high crystallinity and less disordered magnetic structure for FO-CA and FO-NA particles.

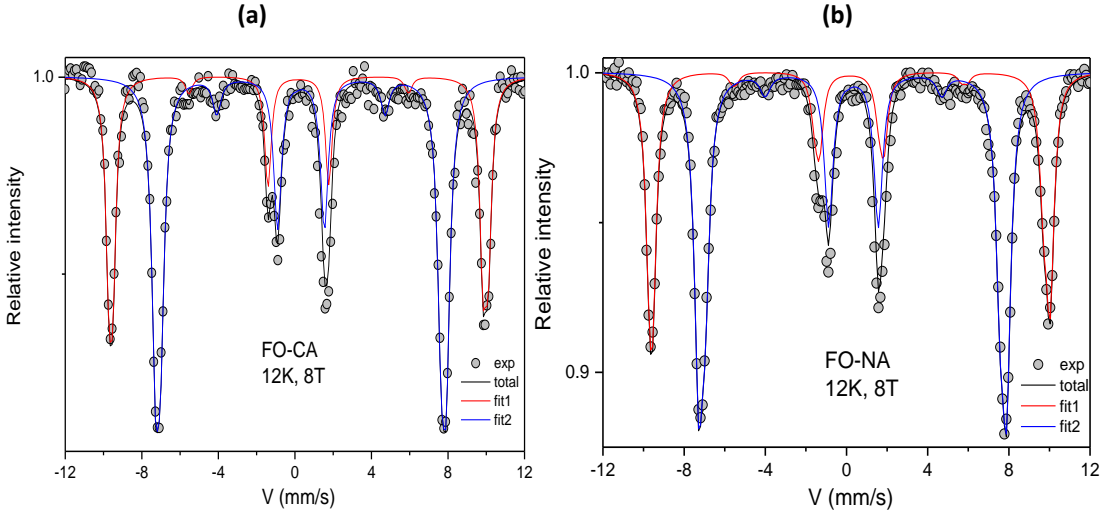


**Fig. 3.15:**  $^{57}\text{Fe}$  Mössbauer spectra measured at 12 K under high magnetic field (8 T) and fitted with 2 sextets corresponding to iron in A-site, and B-site for (a) FO-CA and (b) FO-NA.

**Tab.3.3:** Hyperfine parameters (Isomer Shift, Quadrupolar Shift, Effective and Hyperfine fields, Angle  $\theta$ , and weight) obtained from Mössbauer spectra recorded at 12 K under external field of 8T.

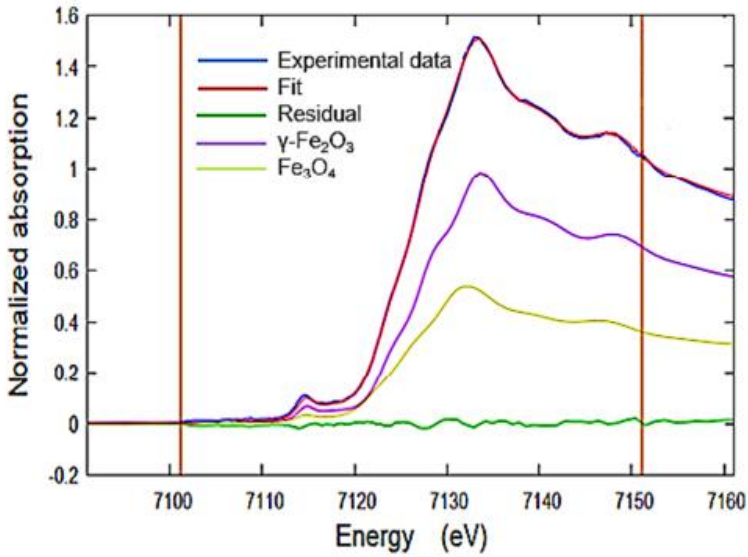
Sample	Sites	$\delta$ (mm.S-1)	$2\varepsilon$ (mm.S-1)	$B_{eff}$ (T)	$B_{hyp}$ (T)	$\theta$ ( $^{\circ}$ )	%
FO-CA	A	0.36	-0.01	60.5	52.8	16	38
	B	0.50	-0.00	46.2	53.8	20	62
FO-NA	A	0.35	-0.03	60.4	52.8	16	39
	B	0.51	-0.03	46.1	53.9	15	61

Fe-K edge XANES analysis to individuate and quantify the maghemite and magnetite phases in iron oxide MNPs is reported in **Figure 3.16**, (details in section 2.6). The analysis was performed on FO-CA sample in order to verify its oxidation state. The oxidation state and average local coordination chemistry of the Fe cation in maghemite ( $\gamma\text{-Fe}_2\text{O}_3$ ) is 3+ with 6 Oxygen nearest neighbors

octahedrally coordinated ( $\text{Fe}^{3+}\text{O}_6$ ). In magnetite ( $\text{Fe}_3\text{O}_4$ ) Fe is found either as octahedral coordinated ( $\text{Fe}^{2+}\text{O}_6$ ) 2+ cations and as a combination of octahedral ( $\text{Fe}^{3+}\text{O}_6$ ) and tetrahedral ( $\text{Fe}^{3+}\text{O}_4$ ) coordinated cations. Such a different local coordination chemistry and valence state, make the Fe K edge XANES of maghemite and magnetite clearly distinguishable. In this study we used the Linear Combination Fit (LCF) method to understand the Fe phase composition of NPs. In LCF the experimental XANES spectrum of unknown sample  $\mu_{exp}$  is fitted to a linear combination of XANES spectra of reference compounds:

$$\mu_i^{\text{ref}} = \sum_i \alpha_i \mu_i^{\text{ref}} \quad (3.3)$$

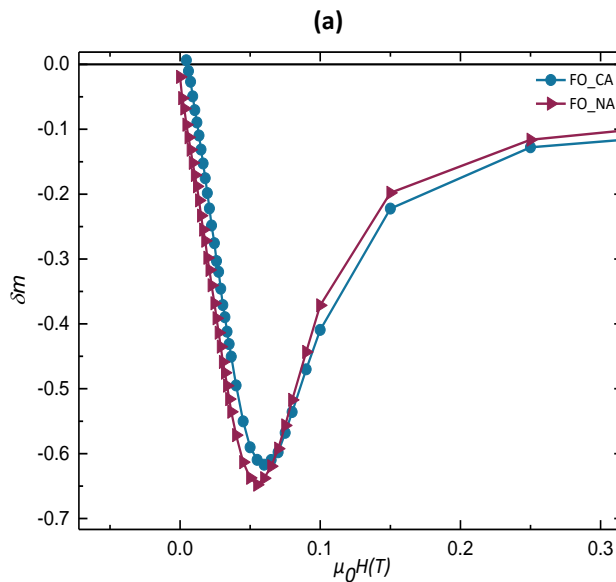
here the  $\alpha_i$  represent the fraction of Fe in the sample being in the i-th phase. The LCF was performed using Athena program (from Demeter package), data were fitted in the 7090-7160 eV energy region around the Fe K edge (7112 eV). After check we found a combination of  $\gamma\text{-Fe}_2\text{O}_3$  and  $\text{Fe}_3\text{O}_4$  reference spectra enough to achieve satisfactory fit , and the best fit gives 65%  $\gamma\text{-Fe}_2\text{O}_3$  and 35%  $\text{Fe}_3\text{O}_4$  meaning that in this sample about 2/3 of Fe ions reside in a local environment close to that of  $\gamma\text{-Fe}_2\text{O}_3$  and about 1/3 close to that of  $\text{Fe}_3\text{O}_4$  local structure [131].



**Fig. 3.16:** Linear Combination fit analysis of FO-CA nanoparticles.

### 3.3.3.3 Interparticle Interactions

Interparticle interactions (type and strength) have been evaluated through  $\delta m(H)$  plots at 5 K, using direct current demagnetization (DCD) and isothermal remnant magnetization (IRM) protocols.  $\delta m$  plots reported in **Figure 3.17**, show the prevalence of demagnetizing interaction, i.e., dipolar interactions, with equal strength within the experimental error.



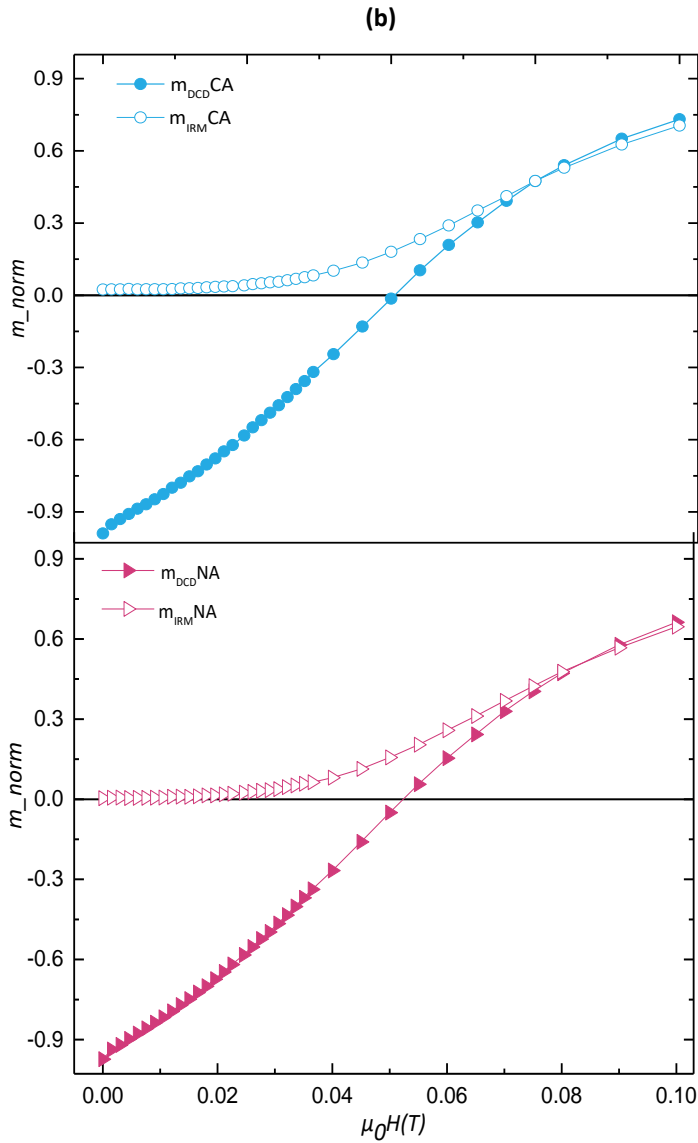


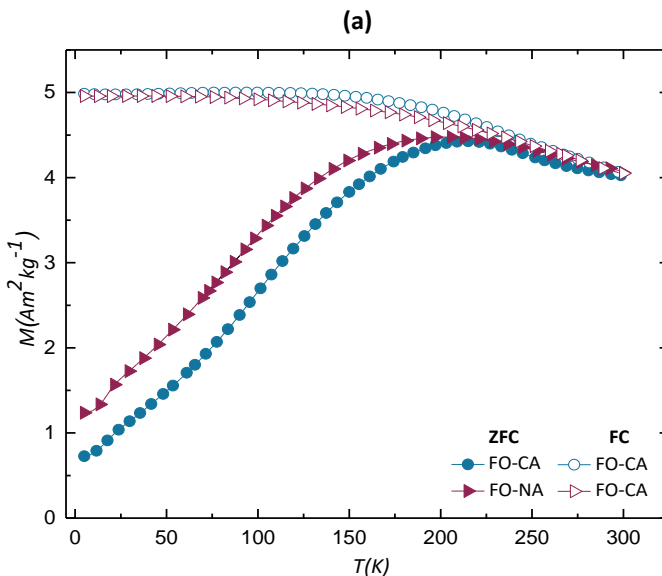
**Fig. 3.17:** (a)  $\delta m$  plots, (b) IRM and DCD curves measured at 5 K corresponding to FO-CA and FO-NA samples.

The presence of interparticle interactions was confirmed by the zero field cooled /field cooled measurements, reported in **Figure 3.18a**. The plateau-like shape at low temperatures in FC curves, confirming the strong contribution of the

interparticle interactions. The samples also show high values of the irreversible temperature ( $T_{irr}$ ), ascribed to the blocking temperature of the biggest particles. The temperature dependence of thermoremanent magnetization (TRM) and its derivative where used to estimate the blocking temperature  $T_B$ , **Figure 3.18b, c**, (details in section 2.3.3). The latter is directly proportional to  $T_{max}$  [44], and it is defined as the temperature for which the relaxation time is equal to the measuring time of the experimental technique used to perform the measurement.

When the investigated system is composed by non-interacting nanoparticles with uniaxial anisotropy, the derivative of  $M_{TRM}$  is used to determine the anisotropy energy barrier distribution which is in turn related to the blocking temperature [46], details in section 2.3.3.

As previously mentioned, that in real system, interparticle interactions are present, therefore the derivative of  $M_{TRM}$  is only a rough estimation of the anisotropy energy distribution and the blocking temperature is determined as the temperature at which 50% of the particles are in superparamagnetic state. The obtained values are reported in **Table 3.4**. All the obtained values of the characteristic temperatures are similar within the experimental error between the two samples suggesting the non-significant difference in magnetization dynamics. At low temperature small peak in the distribution of anisotropy energy barrier curve has been detected (i.e.,  $T_{Low} \sim 25$  K), this correspond to the surface effects as observed in other maghemite samples [118].



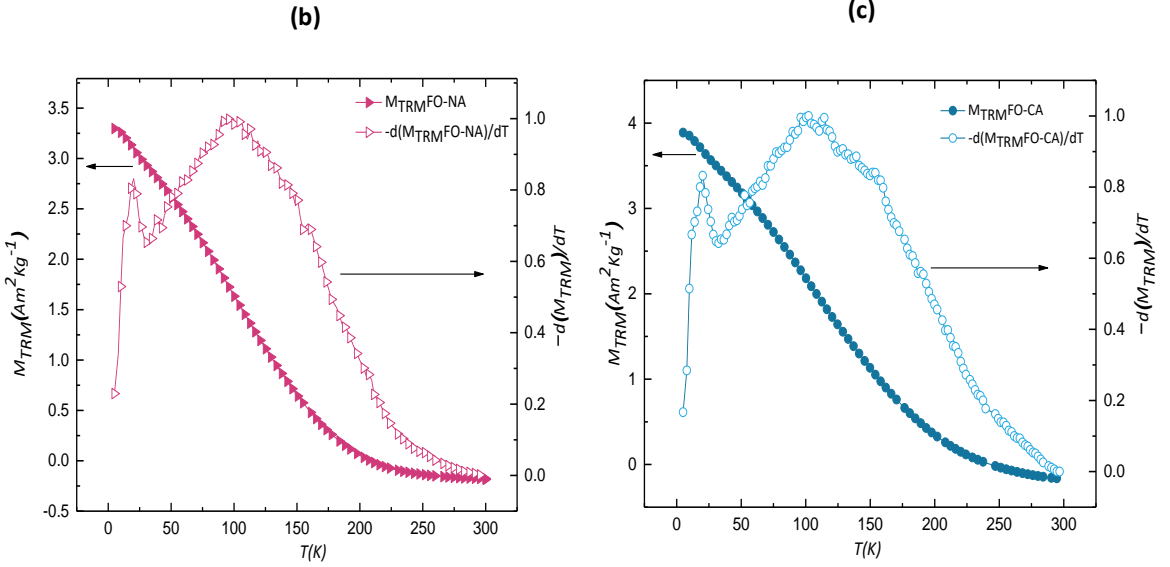


**Fig. 3.18:** (a) ZFC (full) and FC (empty) magnetization curves and  $M_{TRM}$  curves (full), with anisotropy energy barrier distribution (empty) for (b) FO-NA and (c) FO-CA samples measured at 2.5 mT.

As a second estimation of the energy barrier distribution, a phenomenological approach of Hansen and Mørup (H.M) [45]. This model is based on the extraction of the parameters of the log-normal distribution of the barrier energy from the ZFC/FC magnetization curves. According to Hansen and Mørup approach the blocking temperature can be expressed by:

$$\langle T_{B.H.M} \rangle = T_{max} [1.792 + 0.186 \ln(\frac{T_{irr}}{T_{max}} - 0.918)] - 1 + 0.0039 T_{irr} \quad (3.4)$$

Similarly, to the TRM results, the obtained  $T_B$  values from H.M model are equal within the experimental error between the two samples.

Sample	$T_{\max}$ (K)	$T_{B-TRM}$ (K)	$T_{irr}$ (3%) (K)	$T_{B,H.M}$ (K)
FO-CA	203(20)	104(10)	270(27)	125(12)
FO-NA	202(20)	100(10)	273(27)	124(12)

**Tab.3.4:** Temperature corresponding to the maximum in ZFC curve ( $T_{\max}$ ), blocking temperature estimated from TRM measurement ( $T_{B-TRM}$ ), irreversibility temperature ( $T_{irr}$ ) and blocking temperature estimated from Hansen and Mørup approach, uncertainties on the last digit are given in parentheses.

### 3.3.4 Doping effect

In addition to investigation of the reaction atmosphere effect, we have studied the doping effect that relates the structural properties with the magnetic properties of the particles through the effect it imposes upon the final nanoparticles of optimum properties. In  $MFe_2O_4$  structure, the use of different type divalent cation ( $Mg^{2+}$ ,  $Fe^{2+}$ ,  $Co^{2+}$ ,  $Ni^{2+}$  etc.) allows a relative tunability of the magnetic properties such as saturation magnetization or/and magnetic anisotropy. We carry out our studies on  $Fe_3O_4$  sample doped with different amount of cobalt.  $Co^{2+}$  has been chosen since it can make our sample magnetically harder (i.e., tune the anisotropy) and the saturation magnetization relatively high [132,133]. Thus, a series of cobalt doped magnetite were prepared using the co-precipitation of a mixture of iron chloride ( $FeCl_3$ ) and cobalt chloride ( $CoCl_2$ ) via the addition of ammonia solution (30%) acting as the precipitating agent, leads to a pH of 9.2. The starting concentrations of  $FeCl_3$  and  $CoCl_2$  were varied to produce four different samples corresponding to 0 %, 25%, 50%, and 100% referred to as samples FeO, Co25, Co50, and Co100 respectively. After two hours, under homogenous stirring and a temperature of 60°C, the resulting

precipitates were washed with deionized water for several cycles and dried at 60°C for an overnight.

Powder X-ray diffraction (XRD) was used to characterize the produced phases, spectra are illustrated in **Figure 3.19a**. FeO, Co25 and Co50 show reflections characteristic of spinel structure (database code ICSD 257981). Samples with the highest cobalt concentrations (Co100) very broad reflections indistinguishable from the background noise, that can be due to a reduction of particles size or to the increase of the amorphous phase. The incorporation of cobalt shows a significant effect on the particle size as reported in **Figure 3.19b**. This particle size change cannot be directly due to the cobalt substitution since Cobalt has a comparable ionic radius to iron (0.074 and 0.077 nm for Co (II) and Fe (II) in octahedral coordination, respectively [134]).

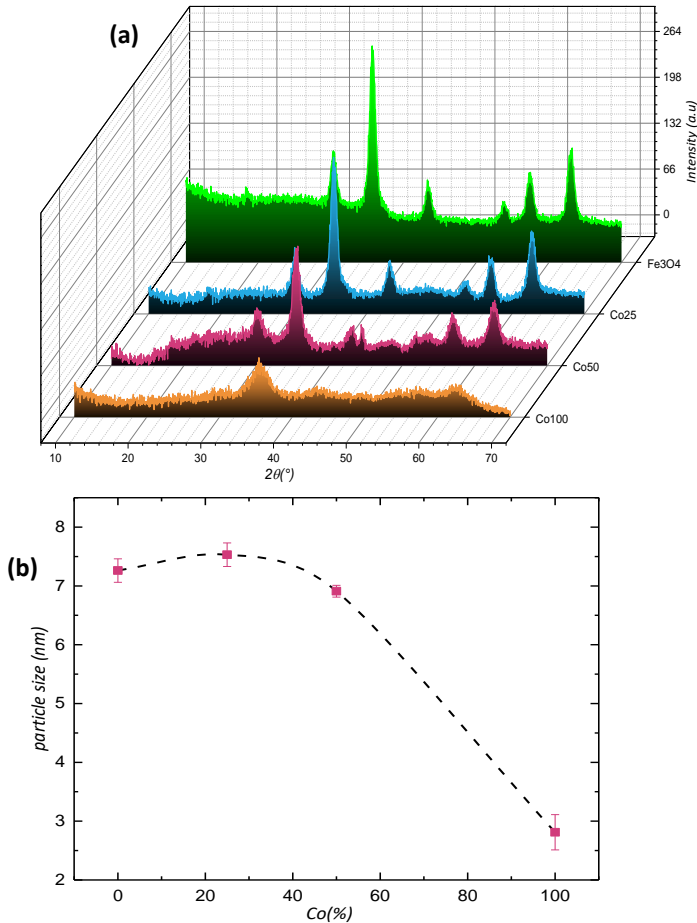


**Fig. 3.19:** (a) XRD patterns (b) Crystallite Size from X-ray diffraction (XRD).

Field dependence of magnetization were carried out at 300 K and 5 K, the obtained hysteresis loops are reported in **Figure 3.20**. As expected At 5K the measurements show a large increase in the coercivity ( $H_c$ ) as the cobalt dopant concentration increases. Reduced remanence values show an increment from about 0.24 to 0.7, indicating that we have passed from sample with uniaxial anisotropy to cubic anisotropy, which is probably due to the increase in the interparticle interactions in a soft material. On the other hand the observed uniaxial anisotropy for bulk  $\text{CoFe}_2\text{O}_4$  sample is due to the ultrafine particle size of this sample, which is confirmed by the XRD analysis [135].  $M_s$  increases with increasing Co amount with respect to pure FeO sample, **Table 3.5**. This increase reaches a maximum at Co50 before a big decrease for Co100, the behavior of the Co100 sample will be deeply discussed in section 3.5. The increase in saturation is due to the difference in the spin of  $\text{Co}^{2+}$  and  $\text{Fe}^{2+}$  and  $\text{Fe}^{3+}$ . In addition The very high saturation magnetization values can be related to the different cationic distribution of  $\text{Co}^{2+}$  in tetrahedral and octahedral sites [136,137]. The room temperature measurements (**Figure 3.20b**) show superparamagnetic behavior for all the samples (i.e.,  $H_c = 0$ ,  $M_r/M_s = 0$ ). Saturation magnetization also follow the same trend observed at 5 K.

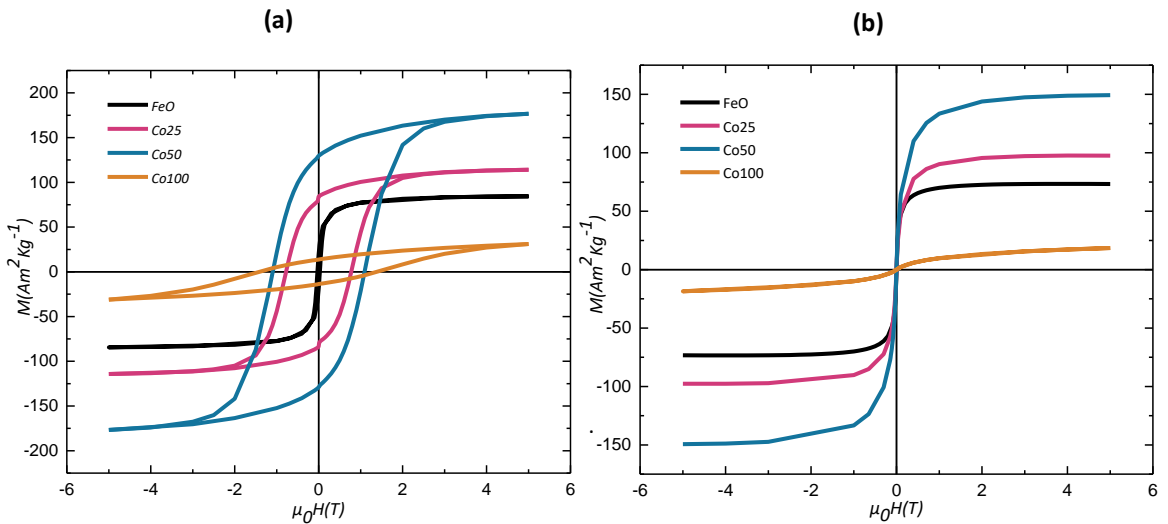


**Fig. 3.20:** Hysteresis loop recorded at (a) 5K (b) 300K.

Sample	Ms (Am <sup>2</sup> Kg <sup>-1</sup> ) 300K	Ms (Am <sup>2</sup> Kg <sup>-1</sup> ) 5 K	Mr/Ms	Hc(mT)
FeO	71(3)	88(3)	0.24	28.7(3)
Co25	96(6)	119(5)	0.7	770(3)
Co50	150(6)	188(2)	0.68	1091(8)
Co100	23(4)	38(1)	0.36	1400(2)

**Tab.3.5:** Saturation magnetization (Ms) at 300K and 5K, reduced remanence magnetization (Mr/Ms) and coercive field (Hc), uncertainties on the last digit are given in parentheses.

### 3.4 Magnetic mesoporous silica based Hybrid-Material: Investigation of the magnetic properties

Since their discovery in the late 1970s, mesoporous silica has attracted quite a bit of attention. This is mainly due to their peculiar properties [138]. Unlike traditional porous silica, mesoporous silica exhibit exceptionally ordered pores that arises from the nanotemplating approach applied during synthesis of these materials, very high specific surface areas, present different morphologies such as spheres rods, discs, powders, etc. Mesoporous silica structures are currently being employed in a number of applications, includes indoor air cleaning [139], catalysis [140], drug delivery [141], bioanalytical sample preparation. On the other hand, magnetic nanoarchitecture have also been extensively exploited in different research field due to their unique properties in particular the control via external magnetic field [142,143]. Recent reports on the design of platforms for drug delivery shown that mesoporous silica functionalized magnetic nanoparticles have proven to be excellent vehicles to carry this task, where the surface of mesoporous silica can be easily functionalized and the presence of the magnetic nanoparticles leads to more controlle/release the molecules in the presence of alternative magnetic field (AMF) [103,144]. Therefore, understanding the effect of mesoporous silica coating on magnetic properties of nanoparticles in the perspective to tune them which will advance the design of

AMF-stimulated applications. Here we report the effect of  $\text{CoFe}_2\text{O}_4$  (synthesized with polyol method) and  $\text{Fe}_3\text{O}_4$  (synthesized with co-precipitation) surface modification with mesoporous silica in tuning the magnetic features of the mesoporous silica based magnetic hybrid materials.

#### 3.4.1 Synthesis process: Polyol chemical method

Polyol is a versatile liquid phase process that typically involves the thermal reduction of a precursor salt to synthesize metals, oxides and semiconductors [105,145,146]. Polyols play a triple role, as reducing agent, solvent and ligand, and offer excellent advantages in various aspects: excellent colloidal stabilization at high boiling points due to the excessive amount of solvent in the polyol; good chelating ability which is a beneficial factor in controlling particle nucleation, growth and agglomeration that can occur during synthesis. As a result, the synthesis of polyols can be considered as a one-pot reaction [105]. In general, the preparation of nanostructured materials with polyol is highly dependent on the boiling point and reduction potential of the polyol. Previous studies reported by Carroll et al. show the significant effect of different types of polyols (e.g. EG, PG, BG, DEG, and TEG) on the final morphology of Cu nanoparticles [147].

Unfunctionalized  $\text{CoFe}_2\text{O}_4$  magnetic nanoparticles (MNPs) were synthesized using polyol chemical method with a small modification [145,148,149]. In brief, 2 mmol of  $\text{Fe}(\text{NO}_3)_3 \cdot 9\text{H}_2\text{O}$  and 1 mmol of  $\text{Co}(\text{NO}_3)_2 \cdot 6\text{H}_2\text{O}$  were dissolved in 1 ml of distilled water. The mixture was added to 100ml of TEG under magnetic stirring and heated to the boiling point of the solvent using a mantle. Once the boiling point is attended, the solution was kept under reflux for 2 hours. After the solution was cooled to room temperature, then the nanoparticles were washed with acetone and collected by centrifugation (10 min, 6000rpm). The removal procedure was repeated three times and the nanoparticles were dried in the oven at  $60^\circ\text{C}$  overnight.

### 3.4.2 Surface Coating: Mesoporous Silica

Magnetic mesoporous silica nanoparticles are very versatile systems (i.e. for the delivery and release of molecules), due to their large surface area and pore volume, the simplicity of their surface functionalization, the variable size of their mesopores and their high resistance to heat and mechanical stress, are all properties that make them suitable for different fields of application. To study the effect of these system on magnetic nanoparticles mesoporous silica coated magnetic nanoparticles have been investigated.

Mesoporous silica (MS) coated  $\text{CoFe}_2\text{O}_4$  MNPs was prepared following sol-gel method based on the hydrolysis and poly-condensation of silica precursor (TEOS) in a basic environment. Briefly, 250mg of CTAB were dissolved and sonicated for 30 min in 20 mL of water, followed by the addition of 100 ml of 2M NaOH solution under stirring. The solution was heated at 80 °C. After the temperature stabilized, 1,25  $\mu\text{L}$  of TEOS was added dropwise. The solution was kept at 80 °C with stirring for 2 h. After the solution was cooled to room temperature, the coated nanoparticles were washed and collected by filtration then dried at 60°C overnight. The obtained sample was named MNPs@MS. A sketch of the coating process is illustrated in **Figure 3.21**.

The same functionalization process was repeated with  $\text{Fe}_3\text{O}_4$  nanoparticles prepared coprecipitation method [150].

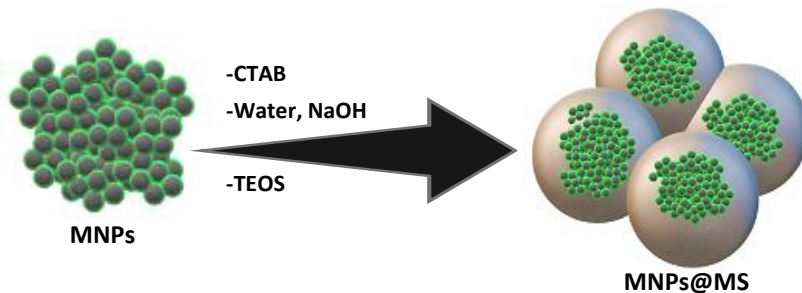


**Fig. 3.21:** Schematic presentation of mesoporous silica (MS) coating.

### 3.4.3 Experimental investigation

#### 3.4.3.1 Mesoporous silica coated $\text{CoFe}_2\text{O}_4$

The cobalt ferrite spinel structure [151] was confirmed by X-ray power diffraction (JCPDS 3-864), **Figure 3.22a**. The main size of the as synthesized MNPs, 4.8(5) nm was obtained from TEM analysis by statistical analysis using log-normal function. After MS coating, TEM image shows nearly monodisperse, spherical MNPs@MS nanoparticles. High-resolution imaging indicates an agglomerates of CFO nanoparticles within the mesoporous silica structure, which results in high average size of 245(50) nm for MNPs@MS sample.

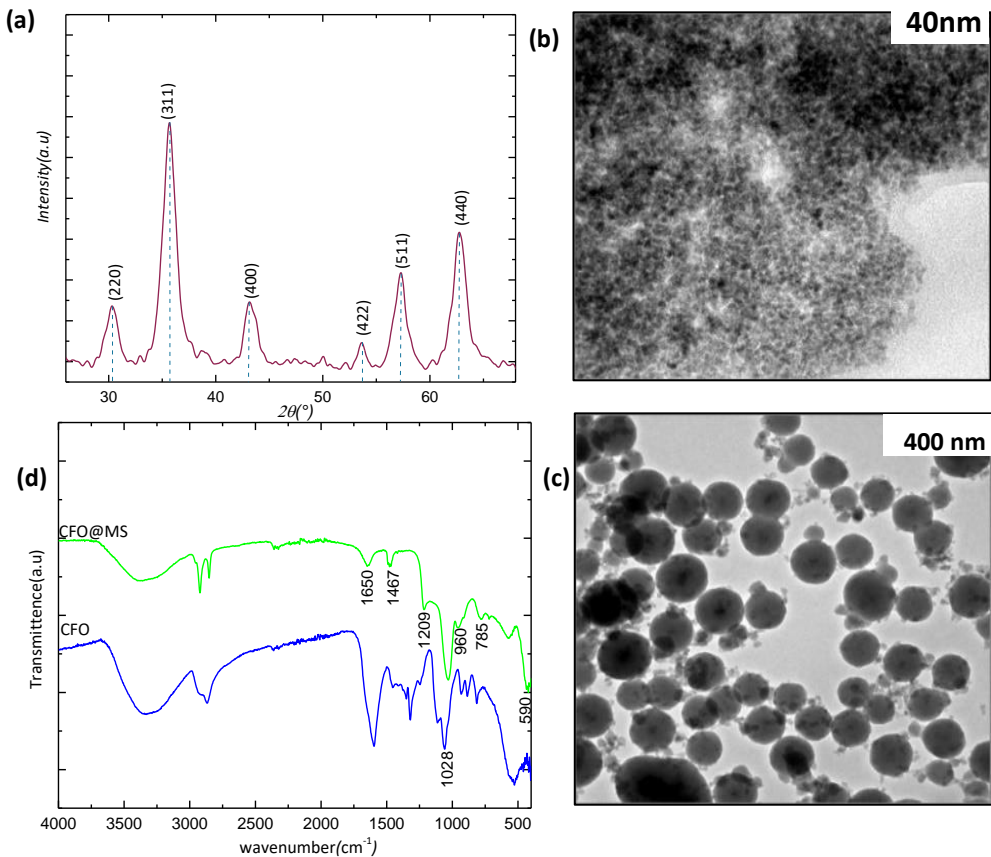


**Fig. 3.22:** (a) XRD pattern, (b, c) TEM images, (d) FT-IR spectra of bare and coated particles.

The MS-coating on the nanoparticle surface was investigated through FT-IR transmission measurements. The spectra of MNPs@MS sample featured  $\text{SiO}_2$  characteristic vibrations in the region between  $1250$  and  $700\text{ cm}^{-1}$ ,  $1031$  and  $1035\text{ cm}^{-1}$  are ascribed to asymmetric Si-O-Si stretching for MNPs-MS. After deconvolution, four components are obtained: two longitudinal (LO) and two transversal (TO) optic modes, related with siloxane rings arrangements. LO and TO peak positions and relative intensity changes can be ascribed to introduction of functional groups or CFO nanoparticles inside the silica structure and subsequent ring re-arrangement. A shift of the Si-O-Si asymmetric stretching band frequency ( $1050\text{ cm}^{-1}$ ) to lower wavelengths ( $1033\text{ cm}^{-1}$ ) was detected, owing to the deformation of silica network after the introduction of the magnetic core.

**Figure 3.23a**, show the thermal behavior of both samples. The Blocking temperature was estimated from the derivative of  $M_{\text{FC}}-M_{\text{ZFC}}$  curve as shown in **Figure 3.23b** (details in section 2.3.2). All the obtained characteristic temperature (**Table 3.6**), were equal within the experimental error within the experimental error before and after MS coating, suggesting that silica presence does not affect the magnetic features of the nanoparticles.

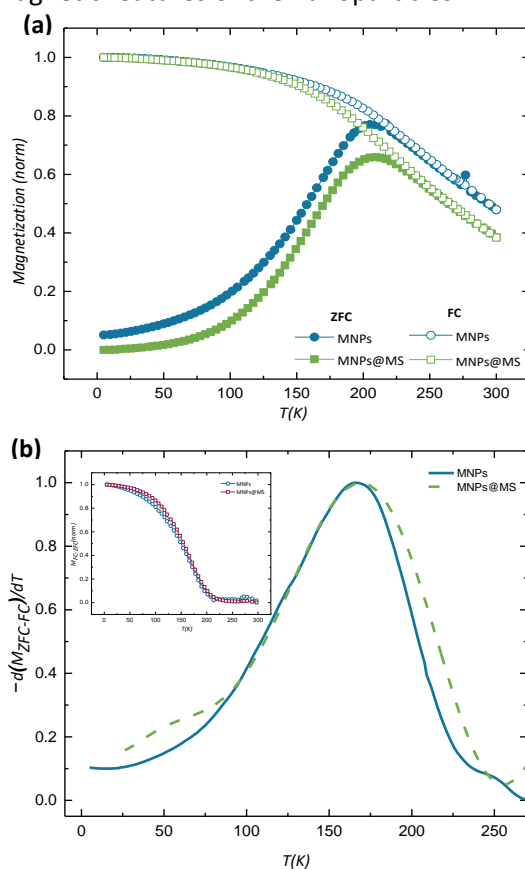


**Fig. 3.23:** (a) M vs (T) measured in zero field cooled (ZFC, full symbols) field cooled (FC, empty symbols) at 2.5mT, (b) Distribution of anisotropy energy barrier.

Sample	H <sub>c</sub> (mT)	M <sub>s</sub> (Am <sup>2</sup> Kg <sup>-1</sup> )	T <sub>max</sub> (K)	T <sub>irr</sub> (K)	T <sub>B</sub> (K)
MNPs	930(93)	90(9)	205(20)	218(21)	166(16)
MNPs@MS	900(9)	88(8)	209(20)	222(22)	167(16)

**Tab.3.6:** coercive field (H<sub>c</sub>), Saturation magnetization (M<sub>s</sub>) at 5K, reduced remanence magnetization (M<sub>r</sub>/M<sub>s</sub>) and temperature corresponding to the maximum in ZFC curve (T<sub>max</sub>), blocking temperature estimated from ZFC-FC measurement (T<sub>B</sub>), irreversibility temperature (T<sub>irr</sub>), uncertainties on the last digit are given in parentheses.

All the characteristic temperature (**Table 3.6**), were equal within the experimental error before and after MS coating, suggesting that silica presence does not affect the magnetic features of the nanoparticles.

**Figure 3.24a** illustrate the field-dependent magnetization curves measured at 5K, the magnetic behavior of bare nanoparticles was in agreement with the magnetic properties of the CoFe<sub>2</sub>O<sub>4</sub> nanoparticles previously reported in the literature. Similarly, to the trend of the characteristic temperatures reported before, it was found that the magnetic properties of the nanoparticles were preserved after the mesoporous silica coating which resulted in equal M<sub>s</sub> and the H<sub>c</sub> values within the experimental error. The reason behind that MNPs@MS still present high saturation magnetization similar to the uncoated particles can be owing to the presence of the TEG shell that lead to the protection of the outer surface of the nanoparticles.

δm plots are reported as a further measurement to investigate interparticle interactions before and after coating, **Figure 3.24b**. The results indicate the

prevalence of dipolar interactions for both samples with a small decrease in interaction intensity that can be considered within the experimental error.

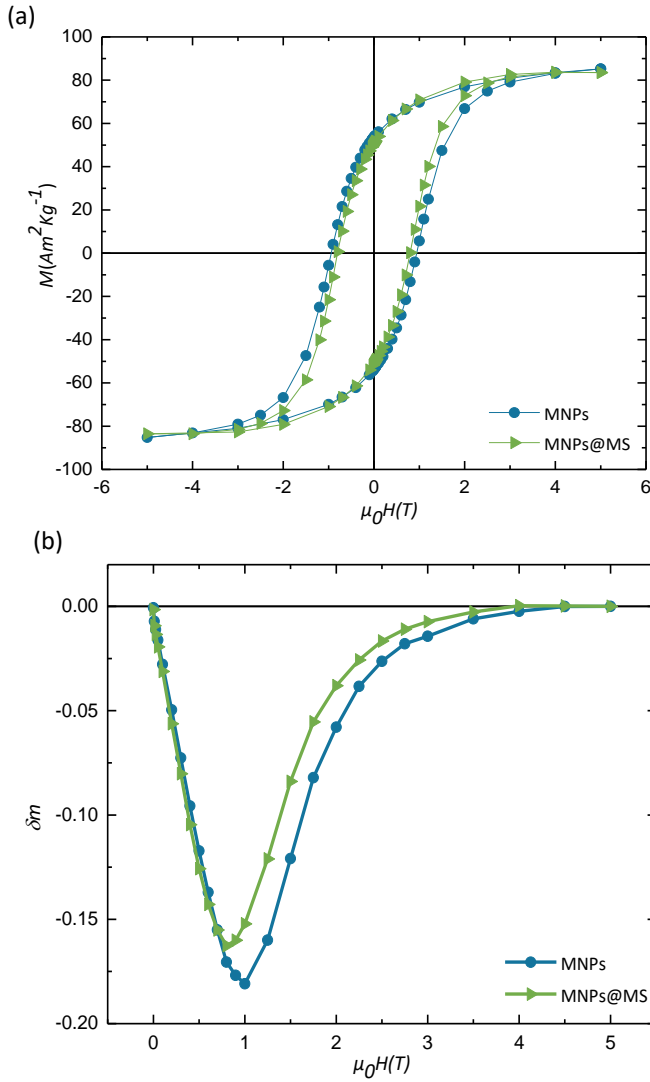


**Fig. 3.24:** (a)  $M$  vs  $(H)$  measured at 5K, (b)  $\delta m$  plots at 5K for uncoated and coated particles.

### 3.4.3.2 Mesoporous silica coated Fe<sub>3</sub>O<sub>4</sub>: Magnetic investigation

Every nanostructure exhibits different magnetic properties from each other which become more exotic after particle surface modification in some cases. In order to further investigate the effect of mesoporous silica shell on the features of the magnetic core, we follow our study with a magnetic investigation on bare

magnetite nanoparticles (FO) and mesoporous silica coated magnetite (FO@MS) [150]. Fe<sub>3</sub>O<sub>4</sub> nanoparticles was prepared with coprecipitation (detailed in chapter 2) deeply analyzed [108], and functionalized with mesoporous silica according to the process reported in section 3.4.2. Thus, we will report in this part just the magnetic investigation.

#### 3.4.3.2.1 Magnetization Dynamic

Zero field cooled (ZFC) field cooled (FC) measurements under an applied magnetic field  $H=2.5\text{mT}$ , are presented in **Figure 3.25a** for bare and coated samples. The shape of these curves depends considerably on the particular nanoparticles distribution, i.e., the interactions among particles. As a main feature, the blocking temperature  $T_B$ , as well  $T_{\text{max}}$  and irreversible temperature ( $T_{\text{irr}}$ ) become lower as the interparticle interactions of the material is reduced. We notice that higher temperatures values (**Table 3.7**) are for bare particles, in agreement with the idea of the prevalence of interparticle interactions for uncoated Fe<sub>3</sub>O<sub>4</sub> nanoparticles. As a usual observation, the low temperature flat part of the FC curves suggests the presence of inter-particle interactions in both samples but with different strength.

The anisotropic energy barrier distribution was reported for both samples from the ZFC/FC curves, **Figure 3.25b**. The two selected samples show different behaviors. A narrower anisotropy distribution is obtained for FO@MS compared to the FO sample. This result likely confirms the change of the nanoparticle arrangement after silica coating, since the magnetic core was the same for both samples (i.e., no change in the particle size distribution or in the intrinsic magnetic anisotropy of the material)

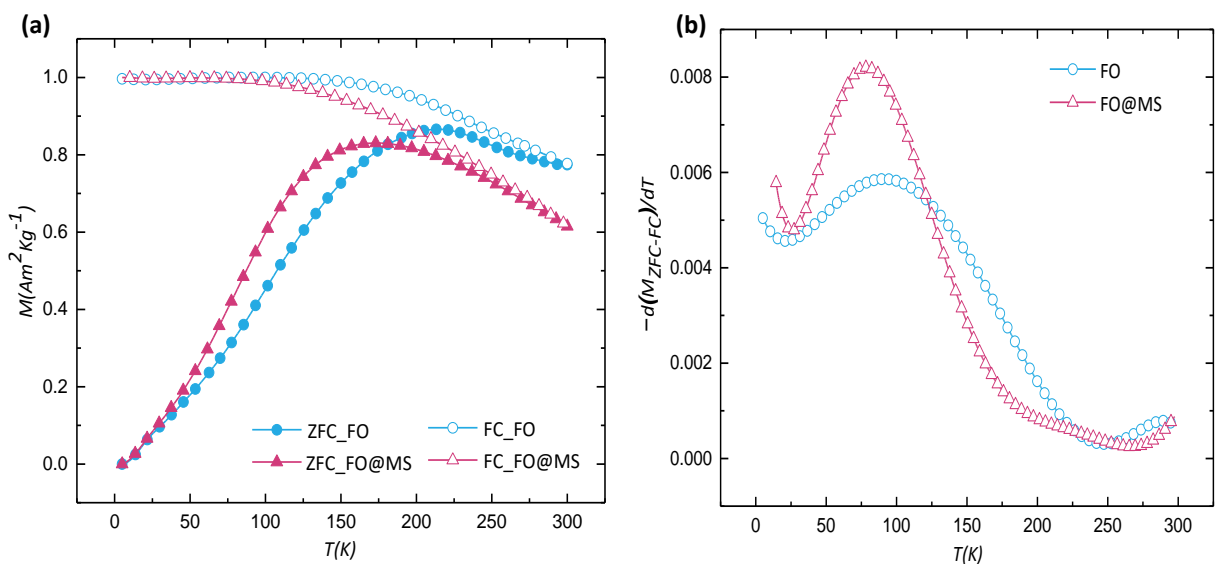


**Fig. 3.25:** (a) ZFC-FC magnetization curves, (b) anisotropy energy barrier distribution.

Sample	$H_c$ (mT)	$M_s$ ( $\text{Am}^2 \text{Kg}^{-1}$ )	$M_r/M_s$	$T_{\max}$ (K)	$T_{\text{irr}}$ (K)	$T_B$ (K)
FO	0.28(3)	92(6)	0.20	213(21)	290(29)	98(9)
FO@MS	0.29(8)	90(9)	0.28	173(15)	229(23)	85(8)

**Tab.3.7:** coercive field ( $H_c$ ), Saturation magnetization ( $M_s$ ) at 5K, reduced remanence magnetization ( $M_r/M_s$ ) and temperature corresponding to the maximum in ZFC curve ( $T_{\max}$ ), blocking temperature estimated from ZFC-FC measurement ( $T_B$ ), irreversibility temperature ( $T_{\text{irr}}$ ), uncertainties on the last digit are given in parentheses.

### 3.4.3.2.2 Nanoparticles arrangement

If particles are in superparamagnetic regime and in the limit of small field, the magnetization of an assembly of isolated particles with uniaxial anisotropy is given by [152]:

$$M = \frac{\langle \cos^2 \beta \rangle}{k_B T} M_S^2(T) n(V) V^2 H \quad (3.4)$$

Where  $\beta$  is the angle between the easy magnetic axis and the applied field,  $n(V)$  is the volume distribution.

When the temperature tends to zero, according to eq 3.4,  $M_{FC}$  is given by:

$$M_{FC} = \langle \cos^2 \beta \rangle \frac{M_S^2(0)}{k} \ln \left( \frac{\tau_w}{\tau_0} \right) n(V) V H \quad (3.5)$$

For real sample with random distribution of particles easy axis,  $\cos^2 \beta \geq 1/3$ , and supposing that  $\alpha$  present the fraction of nanoparticles with aligned distribution of easy axis and  $(1-\alpha)$  is the fraction of present the random easy axis, then MFC can be written as:

$$M_{FC}^{align} = \frac{M_S^2(0)}{3k} \ln \left( \frac{\tau_w}{\tau_0} \right) n(V) V H (1 - \alpha + 3\alpha \cos^2 \beta) \quad (3.6)$$

$$\frac{M_{FC}^{align}}{M_{FC}} = 1 + \alpha(3 \cos^2 \beta - 1) \quad (3.7)$$

In case  $\alpha=0$ ,  $\frac{M_{FC}^{align}}{M_{FC}} = 1$ , then all particles are randomly oriented.

In case  $\frac{M_{FC}^{align}}{M_{FC}} \neq 1$ , then a fraction of nanoparticles with oriented easy axis is present.

Accordingly, for 10K we found that for bare nanoparticles  $\frac{M_{FC}^{align}}{M_{FC}} = 0.996$ , indicating the random distribution of the magnetic moment within the experimental error. While for FO@MS sample the ratio is equal to 6. Despite the fact that this gives just qualitative information, the obtained value indicates that a portion of nanoparticles are with oriented easy axis [153]. This probably

corresponds to the effect of the magnetic stirring during the coating process. The easy axis can be partially aligned by the magnetic field from the stirrer and the configuration is fixed by the mesoporous silica structure.

ZFC/FC measurement has followed by field dependence of the magnetization measured at 5K and the hysteresis loops are shown in **Figure 3.26**. The obtained values of the saturation magnetization were the same within the experimental error for both bare and coated particles, suggesting that the presence of the mesoporous silica structure does not affect the magnetic characteristics of the MNPs, on the other hand it contributes to the reduction of interparticle interactions.

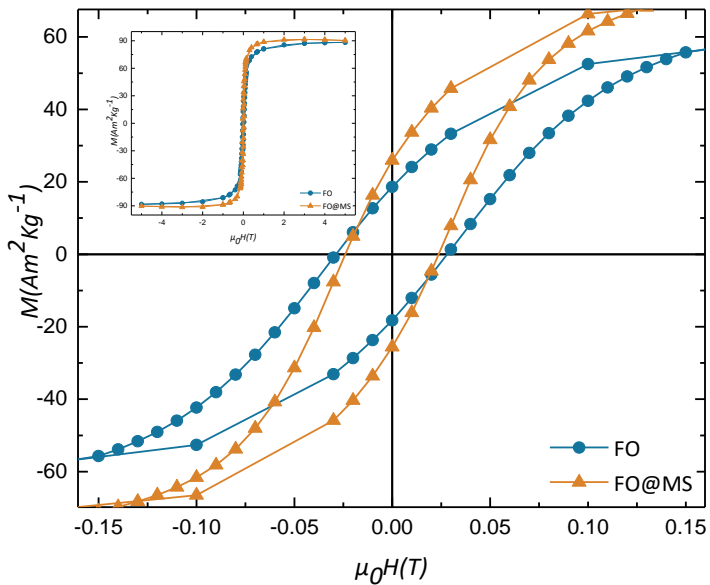


**Fig. 3.26:** (a) M vs (H) measured at 5K.

In order to fully understand the effect of the mesoporous silica coating on the interparticle interactions, delta  $\delta M$  plots were studied, **Figure 3.27**. The results show an obvious reduction of the interparticle dipolar interactions [154] (details in section 1.5) after the silica coating.

The change in the type or strength of the interparticle interaction can be attributed to the change in the interparticle distance, saturation magnetization

or volume of the nanoparticles. However, in our case, the magnetic core of the FO and FO@MS samples comes from the same synthesis batch (i.e., there is no change in the size distribution), with no change in the saturation magnetization even after the coating process. Consequently, the results obtained can be explained by a change in the interparticle distance. To estimate this change, the ratio  $d_{\text{FO@MS}}/d_{\text{FO}}$  is calculated:

$$\frac{d_{\text{FO@MS}}}{d_{\text{FO}}} = \sqrt[3]{\frac{E_{\text{dipFO}}}{E_{\text{dip FO@MS}}}} \approx \sqrt[3]{\frac{\delta M_{\text{FO}}}{\delta M_{\text{FO@MS}}}} \quad (3.8)$$

we obtained a value of 1.05, which confirms that the average interparticle distance increases after mesoporous silica coating by 5%.

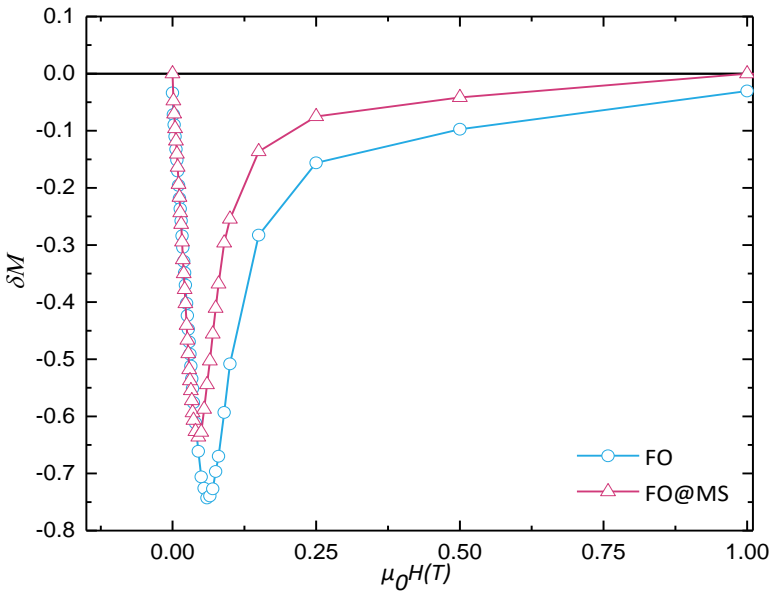


**Fig. 3.27:**  $\delta M$  plots of bare (FO) and coated (FO@MS) particles.

## 3.5 Magnetism in Hybrid Materials: Design New Magnetic properties.

In this section, we demonstrate that the magnetic properties of a hybrid material are not only the sum of the different individual contributions, but that they can also lead to the emergence of new properties. To cover this aspect, we report here a study on a cobalt ferrite-based hybrid system combining a crystalline and an amorphous parent material. The morpho-structural, the magnetic properties and the micromagnetic model of crystalline/amorphous  $\text{CoFe}_2\text{O}_4$  nanocomposite were investigated. The choice of the material tends also to show the active role of amorphous phase to tune the magnetic properties, in particular magnetic anisotropy. Generally, amorphous phase is considered a drawback and often depicted as a dead layer in the nanostructured magnetic materials due to its contribution to reduce the saturation magnetization. However, we have demonstrated the active role of the amorphous phase which contribute to improve the magnetic properties of our material.

### 3.5.1 Experimental investigation

#### 3.5.1.1 Sample Preparation

The crystalline/amorphous cobalt ferrite nanocomposite was prepared by coprecipitation method (details in section 3.3.1) with some modifications. In brief, 100 mL of HCl solution poured into 2-necked glass flask, one connected to a vacuum and a gas inflow port, and the other used for the materials' transfer. The reaction was carried out at 60°C under a homogenous stirring (630 rpm). Before adding the salts, the HCL solution was purified alternating between vacuum and nitrogen ( $\text{N}_2$ ) gas three times. Afterwards, a mixture of 3.15 mmol  $\text{CoCl}_2 \cdot 4\text{H}_2\text{O}$  and 6.21 mmol  $\text{FeCl}_3 \cdot 6\text{H}_2\text{O}$  was added to the balloon, and the  $\text{N}_2$  flow was remained until the end of the reaction. After mixing for 60 min, 20 mL of ammonium hydroxide (30%), previously deoxygenated (10 min under  $\text{N}_2$  reflux), was added rapidly, which lead to an abrupt transition from pH = 2–9.5, results visually in change in the color to reddish-brown. The value of pH was chosen to favor the formation of non- stoichiometric hydroxide precipitate in the solution.

After 60 min from ammonium adding, the resulting precipitates were collected using a centrifuge and washed for several cycles with distilled water (15 min, 6000 rpm). Finally, the magnetic nanoparticles were dried at 60 °C overnight to obtain the crystalline-amorphous nanocomposite in form of powder [155].

### 3.5.1.2 Morpho-structural Investigation

Phase identification was carried out by X-ray powder diffraction (XRD), the results was analyzed with Rietveld refinement of the XRD pattern, using MAUD software. The obtained pattern illustrated in **Figure 3.28** shows reflections confirm the crystalline phase of the cobalt ferrite (fcc structure) in pH = 9.5 (database code ICSD 257981), accompanied by the presence of a wide hump of the amorphous phase. This result suggests the presence of small crystalline cobalt ferrite nanoparticles embedded within an amorphous parent material matrix. The average crystalline size was estimated by applying the Debye–Scherrer formula (details in section 2.1) to the most intense reflection of the XRD pattern peak to be 3 nm.

The refinement was performed considering the sample as a two phase-system, a crystalline cobalt ferrite phase with the standard bulk parameters and an amorphous phase with the starting value of the grain size manually adjusted to reproduce the amorphous humps visible under the crystalline peaks, which were not reproducible with a simple second order polynomial background. The refinement of the microstructure of the sample confirms the presence of regular crystalline grains of 3.4(5) nm representing about 25% of the total volume of the sample. The residual volume (75%) is occupied by the amorphous parent material having similar structure, but a very small granular size of 0.9(5) nm, responsible of the missing long-range order. Interestingly, both phases exhibit little to no microstrain, estimated in  $0(5) \times 10^{-5}$  and  $9(5) \times 10^{-5}$  for the crystalline and amorphous component, respectively.

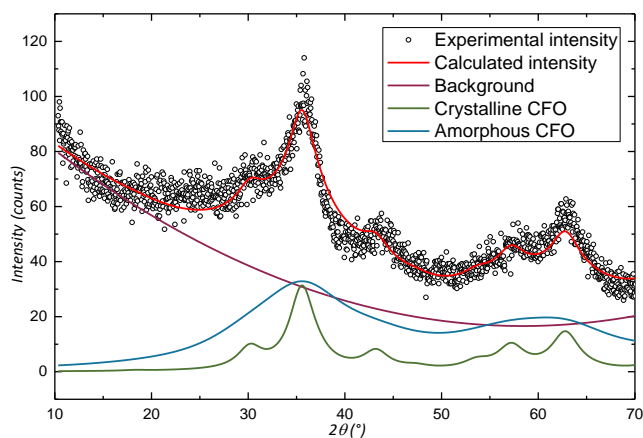


**Fig. 3.28:** Experimental XRD pattern (black dots) and its Rietveld refinement (red line) using a crystalline cobalt ferrite component (black line) and a corresponding amorphous one (blue line). The calculated background intensity is reported as a green line.

Transmission electron microscopy (TEM) measurements reported in Figure 3.29 indicate the presence of large aggregates with the dimension of about 100 nm with granular structure (**Figure 3.29a**). The SAED pattern corresponding to the area of the same sample reported in **Figure 3.29b** shows poorly crystallized aggregates, composed of diffraction rings having a diffuse intensity typical of a large number of small crystals randomly oriented and dispersed inside an amorphous matrix. In agreement with the XRD diffraction, the lattice distances associated with the diffraction rings confirm the presence of the fcc cobalt ferrite phase. The dark-field TEM image was obtained by selecting a portion of the diffraction ring encircled in the previous figure. **Figure 3.29c** bright spots related to the presence of fine and uniform dispersion of very small crystalline particles. For a further investigation of the crystalline/amorphous nature of the sample high-resolution (HR) TEM analysis have been reported in **Figure 3.29d**. The major part of the sample shows a granular contrast ascribable to amorphous phase, with the presence of the atomic planes of a small particle (the encircled region in the figure), confirming the dispersion of nanocrystals inside an amorphous matrix.

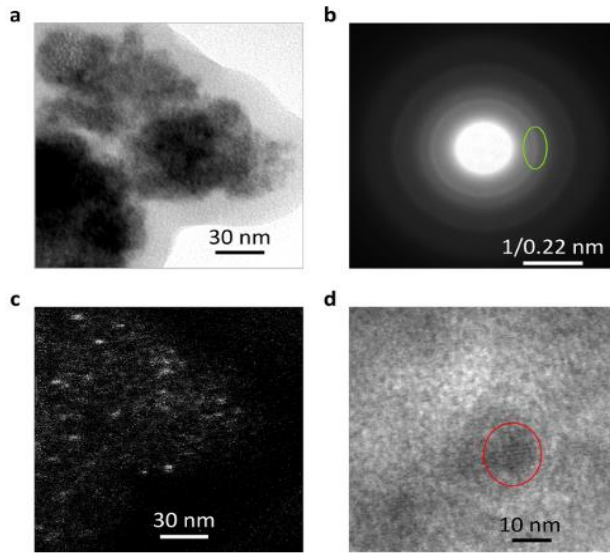


**Fig.3.29:** (a) Bright-field TEM image showing the powdered sample composed of primary aggregates (~100 nm) having a granular structure. (b) Corresponding selected area electron diffraction pattern. The diffuse intensity of the diffraction rings suggests the presence of small crystals in an amorphous matrix. (c) Dark-field image obtained with the portion of the diffraction ring encircled in (b) revealing the presence of small crystalline nanoparticles (bright spots) uniformly dispersed in the amorphous granular matrix. (d) High-resolution TEM image showing the atomic planes of a crystalline nanoparticle inside the amorphous matrix.

### 3.5.1.3 Magnetic Properties

Mössbauer spectroscopy under an intense magnetic field, 8T parallel to the  $\gamma$ -ray direction at 12K, have been carried out to investigate the magnetic structure of the sample. Interestingly, since the magnetic field is applied parallel to the  $\gamma$ -ray direction, the noncollinear magnetic moment of  $\text{Fe}^{3+}$  cations to the applied field give rise to the intensity of the second and the fifth lines as an indication of the presence of the spin canting within the structure, apart from that, they are equal to zero. **Figure 3.30a** illustrate the sample spectrum. The latter shows a broad asymmetrical line referring to the disordered magnetic structure, with the presence of large number of canted spins results in a sign can't average canting angle Tale2.6. The mean hyperfine values ascribed to  $\text{Fe}^{3+}$  in both sites,

determined through the hyperfine field distribution correlated to a canting angle distribution as illustrated in **Figure 3.30b**.

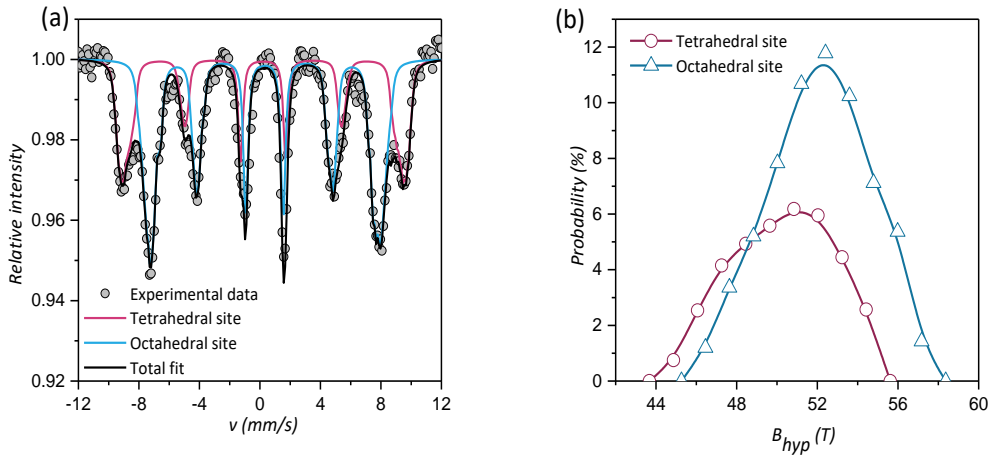


**Fig.3.30:** (a) Mössbauer spectrum recorded at 12 K with an applied field of 8 T. (b) Distribution of the hyperfine field ( $B_{hyp}$ ) observed for both Td and Oh sites obtained by the fitting procedure.

Component	$\delta$ (mm.S-1)	$2\varepsilon$ (mm.S-1)	$B_{eff}$ (T)	$B_{hyp}$ (T)	$\theta$ (°)	%
T <sub>d</sub>	0.41	0.01	57.0	50.8	37	36
O <sub>h</sub>	0.49	0	46.8	52.2	51	64

**Tab.3.8:** Mean Values of the Hyperfine Parameters Extracted from the Fit to the Experimental Data: Isomer shift ( $\delta$ ), quadrupole splitting ( $2\varepsilon$ ), effective magnetic field ( $B_{eff}$ ), average canting angle ( $\theta$ ), hyperfine field ( $B_{hyp}$ ), and the % occupancy of each site.

The magnetic behavior of cobalt ferrite nanoparticles dispersed within amorphous parent material matrix was investigated. Magnetization measurements under a magnetic field at 5K and 300K are present in **Figure 3.31**. At 5k the hysteresis loop shows considerable dependence from the amorphous

phase contribution, resulting in high coercive field,  $\mu_0 H_C \approx 1.4$  T and unsaturated loop. As a rough estimation of the saturation magnetization, law of approach to saturation was applied giving a value of about  $40 \text{ A m}^2 \text{ kg}^{-1}$ . Considering that only 25% of the total volume represent the crystalline phase and even by attributing to it the bulk value ( $85 \text{ A m}^2 \text{ kg}^{-1}$ ), an additional magnetization contribution about  $13 \text{ A m}^2 \text{ kg}^{-1}$  at 5 T still required to reproduce the experimental value. At 300k, the hysteretic behavior is absent and the sample shows superparamagnetic state.

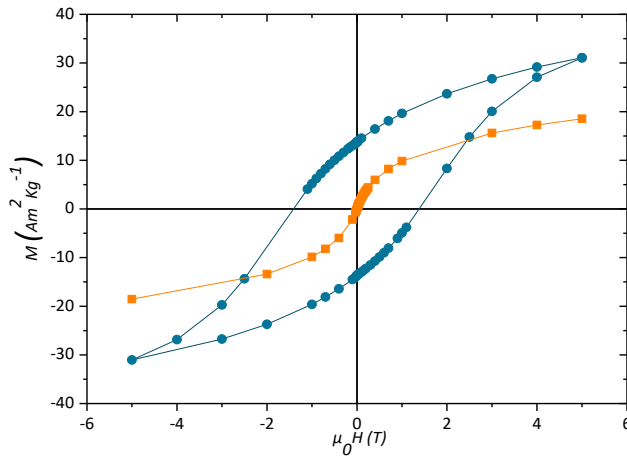


**Fig.3.31:** Magnetization versus field curve measured at 5 K (bleu circles) and 300 K (orange squares).

Thermal dependence of magnetization (**Figure 3.32a**) recorded with zero field-cooled (ZFC) and field cooled (FC) protocols have proved that the magnetic structure of individual crystalline cobalt ferrite is modified by the presence of its amorphous phase, resulting in a very high interparticle interacting regime. The blocking temperature was estimated from the derivative of  $M_{ZFC}-M_{FC}$  with respect the temperature (**Figure 3.32b**). In most of the cases the real samples exhibit a distribution of  $T_B$ , accordingly the average blocking temperature is conventionally defined as the temperature at which 50% of the sample overcome their energy barrier.  $T_B$  is determined when the integral of the  $f(\Delta E_a)$

reaches 50% of its maximum value. Later, a modified formulation has been proposed (Figure 3.32c):

$$\mathcal{F}(\Delta E_a) \propto -\frac{1}{T} \frac{d(M_{FC} - M_{ZFC})}{dT} \quad (3.9)$$

The additional  $1/T$  term in the new formulation is referring to the renormalization of the contribution of large particles volume, which reverse in the bias of  $T_B$  to highest values due to their large magnetic moment. Taking into account both approaches, the average effective blocking temperature was found to be about 95 and 60k for conventional and modified formulation respectively. However, both reported values are considered large than that of particles with similar size(20K). This result suggests the significant effect of the interparticle interaction on the thermal behavior of the sample, which appear through the presence of the flat part at low temperature of FC curve, typical of strongly interacting particles.

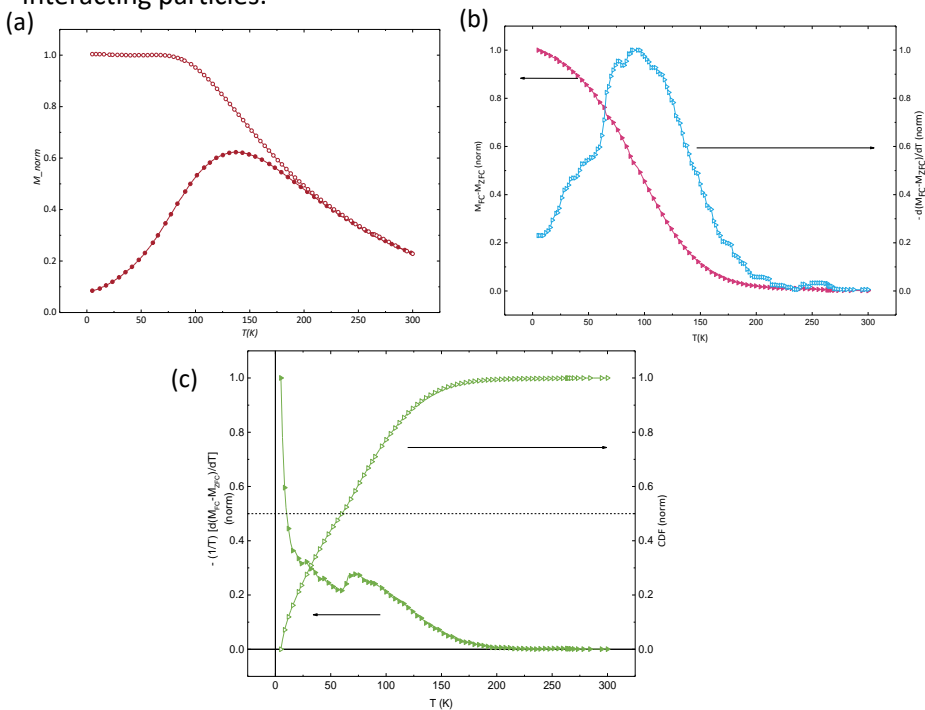


**Fig.3.32:** (a) ZFC (empty black squares) and FC (full red circles) curves measured with an applied field of 2.5 mT, (b) The corresponding FC- ZFC curve (empty black triangles) and the negative derivative representing the blocking temperature distribution (reversed full

red triangles) and (c) The corresponding  $-(1/T) [d(MFC - MZFC)/dT]$  curve (empty green triangles) and its cumulative distribution function (CDF) (full blue stars).

To carefully study the interparticle interactions,  $\Delta M$ -plots and the random anisotropy model (RAM) have been analyzed. Magnetization remanence was measured according to the Isothermal remanent magnetization (IRM) and direct current magnetization (DCD) protocols, details in section 2.3.4. Although the applied magnetic field (5T) in the experimental protocols didn't fully saturate the sample (**Figure 3.33a**), it shows a demagnetizing effect due to the presence of strongly interaction regime, as illustrated in **Figure 3.33b**.

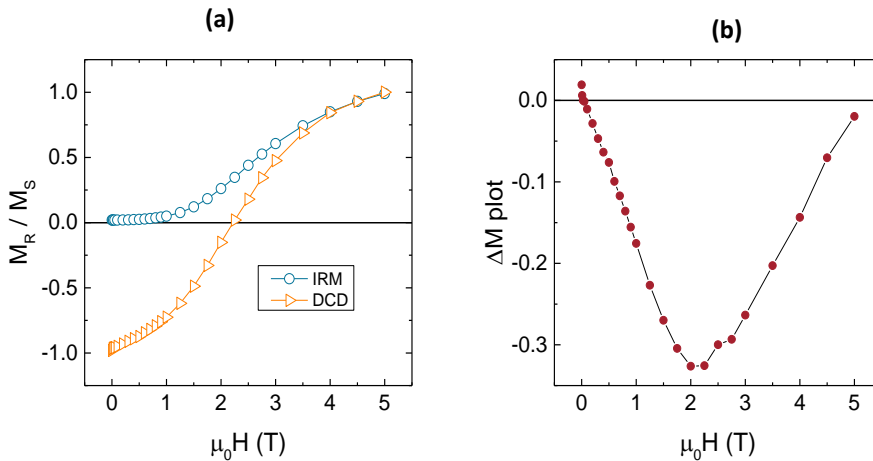


**Fig.3.33:** (a) IRM and DCD curves measured at 5 K and corresponding (b)  $\Delta M$  plot.

### 3.5.2 Random anisotropy model (RAM)

Complementary random anisotropy model (RAM) that analyzes the field dependence of the effective distribution of blocking temperature also confirms the interparticle interactions scenario in the nanocomposite. For interacting magnetic nanoparticles, the effective anisotropy results from the average contribution of the individual interacting elements in a so-called random anisotropy model (RAM). The model has been largely demonstrated for exchange-coupled grains [156]. Recently, it has been successfully proposed to

investigate the interplay between the individual particles anisotropy energy and the interparticle interactions for purely dipolar coupled particles [157].

For an ensemble of non-interacting particles, the dependence of  $T_B$  on the applied field  $H$  is described by the law [158,159]:

$$T_B = \frac{KV}{k_B \ln\left(\frac{\tau_m}{\tau_0}\right)} \left[1 - \frac{\mu_0 H}{\mu_0 H_K}\right]^{1.5} \quad (3.10)$$

where  $K$  is the intrinsic anisotropy constant of the material,  $V$  the nanoparticle volume,  $\tau_m \sim 60$  s (i.e., the typical experimental time in SQUID dc magnetization measurements),  $\tau_0 = 10^{-11}$  s (commonly used for ferromagnetic particles),  $H_K$  the anisotropy field,  $\mu_0 = 4\pi \cdot 10^{-7}$  H/m the vacuum permeability, and  $k_B = 1.38065 \cdot 10^{-23}$  J/K is the Boltzmann constant. For ensembles of interacting nanoparticles, their interactions extend over a magnetic correlation length ( $L_{corr}$ ) [160] that can be expressed as a function of the applied field [159,161]:

$$L_{corr} = D + \left[ \frac{2A_{eff}}{M_S \mu_0 H + C} \right]^{1/2} \quad (3.11)$$

where  $A_{eff}$  represents an effective interaction intensity [162],  $D$  is the average particle diameter, and  $M_S$  the saturation magnetization. The parameter  $C$  is needed to solve the divergence at  $\mu_0 H = 0$  T. It considers the influence of particles concentration on interactions, assuming a value close to zero for clustered particles and the form  $C \approx 2A_{eff} - M_S \mu_0 H$  for non-interacting ones [158,159].  $L_{corr}$  defines the physical extension of the interactions. One can determine the number of correlated particles considering the volume fraction  $x$  effectively occupied by the particles in the ensemble:

$$N = 1 + x \frac{(L_{corr}^3 - D^3)}{D^3} \quad (3.12)$$

Therefore, those  $N$  particles form an effective volume  $V_N$  of magnetic material interacting within the correlation length  $L_{corr}$ :

$$V_N = \frac{\pi}{6} [D^3 + x(L_{\text{corr}}^3 - D^3)] \quad (3.13)$$

Within this correlation volume the effective anisotropy constant  $K_{\text{eff}}$  results from the random walk effect of the anisotropy of the  $N$  correlated particles [162]:

$$K_{\text{eff}} = \frac{K_a}{\sqrt{N}} \quad (3.14)$$

As the interparticle interactions increase, the correlation length expands and the anisotropy averages out over a larger volume, thus reducing its effective magnitude. On the other hand, an external magnetic field reduces the correlation length [161]. For an ensemble of interacting particles, one should consider the effective anisotropy field  $\mu_0 H_K^N$  of the cluster of  $N$  correlated particles, which is linked to its effective average anisotropy  $K_{\text{eff}}$  [158,159]:

$$\mu_0 H_K^N = 2 \frac{K_{\text{eff}}}{M_S} \quad (3.15)$$

Finally, equation (3.10) can be re-written by substituting  $K$ ,  $V$ , and  $H_K$  with the effective values for the cluster  $K_{\text{eff}}$ ,  $V_N$ , and  $H_{KN}$ , respectively, to define the field dependence of the effective blocking temperature of the NPs' ensemble:

$$T_B(H) = \frac{K \frac{\pi}{6} [D^3 + x(L_{\text{corr}}^3 - D^3)]}{6 k_B \ln\left(\frac{\tau_m}{\tau_0}\right) \sqrt{1 + x \frac{(L_{\text{corr}}^3 - D^3)}{D^3}}} \left[ 1 - \frac{\mu_0 H M_S \sqrt{1 + x \frac{(L_{\text{corr}}^3 - D^3)}{D^3}}}{2K} \right]^{1.5} \quad (3.16)$$

where  $D$  is the individual particle diameter,  $L_{\text{corr}}$  is the average magnetic correlation length,  $x$  is the volume fraction of particles,  $K$  is the intrinsic anisotropy constant of the individual particles, and  $M_S$  is the saturation magnetization.

The experimental values of  $T_B(H)$  were extracted using FC and ZFC curves measured at different applied fields, and the effective energy barrier distribution (**Figure 3.34b**) was estimated from the  $M_{FC}-M_{ZFC}$  curve (**Figure 3.34a**).

The model was applied on the distribution of the blocking temperature calculated with both methods, according to the eq.3.16.

In the RAM model we have considered only the crystalline CFO nanoparticles since they are the responsible for the superparamagnetic relaxation in the sample. The saturation magnetization was fixed to the bulk value, the average particle size is 3 nm and fixing the crystalline volume occupancy to 25% according to Rietveld refinement results. Although in our case the model is limited to the crystalline fraction, **Figure 3.34e** shows good agreement between the fitting and the experimental data, obtaining a first qualitative description of the magnetic organization inside the sample. Even that two sets of the field dependence of the blocking temperature data were used, the fits gave similar results within the experimental error and the fitting parameters suggest a correlated volume including an average of 8 nanoparticles resulting from a correlation length of about 10 nm. The similarity in the obtained results is quite reasonable since the RAM analyzes the trend of  $T_B$  versus  $H$ , which is similar for both sets of experimental data and not affected by the used formulation of  $T_B$ . The intrinsic  $T_B$  for an individual particle suggested by the RAM of about 30(5)K, which is the same of an experimental value for cobalt ferrite particles with the same size. Besides, the magnitude of the effective coupling was 1.5(1) pJ/m, which is at least one order of magnitude higher than that observed in spinel ferrites with strong dipolar interactions.

The intrinsic anisotropy constant calculations gave values of about 510(20) kJ/m<sup>3</sup> versus 823(9) kJ/m<sup>3</sup> for the conventional and modified formulation, respectively. This corresponds to the different weights attributed to the largest particles.

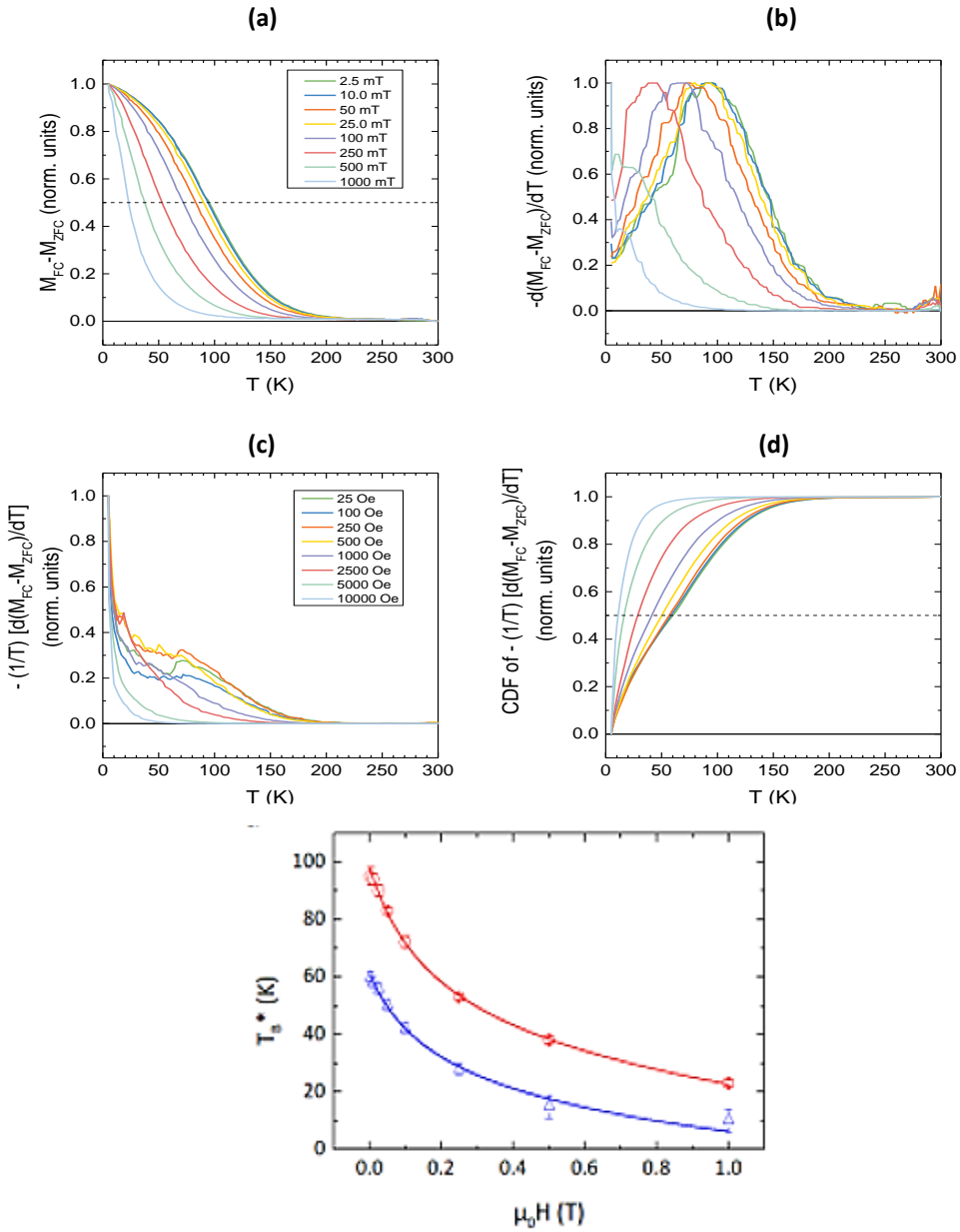


**Fig.3.34:** (a) MFC-MZFC curves as a function of the applied field and (b) the corresponding negative derivative and (c) the corresponding negative derivative from the modified formulation (d) cumulative distribution function of the modified formulation (e) the variation of the blocking temperature calculated with the conventional formulation (empty red circles) and the modified formulation (empty blue triangles) as a function of the applied field with the corresponding fit of eq 3.16 to the experimental data (red and blue line, respectively).

### 3.5.3 Micromagnetic model

In order to properly understand the complex magnetic structure of the nanocomposite ( $\text{CoFe}_2\text{O}_4$  + amorphous), micromagnetic simulations study has been carried out using the Mumax3 code [163] to reproduce the  $M(H)$  curve recorded at 5K. Large aggregates were represented by a simulation box of  $96 \times 96 \times 96 \text{ nm}^3$  formed by cubic cells of 3 nm edge. The sample was represented by an ensemble of grains of 10 nm, with effective uniaxial anisotropy each, with a random easy axis orientation, illustrated in **Figure 3.35a**. 3 nm crystalline particles was reproduced using 8192 cells (**Figure 3.35b**).

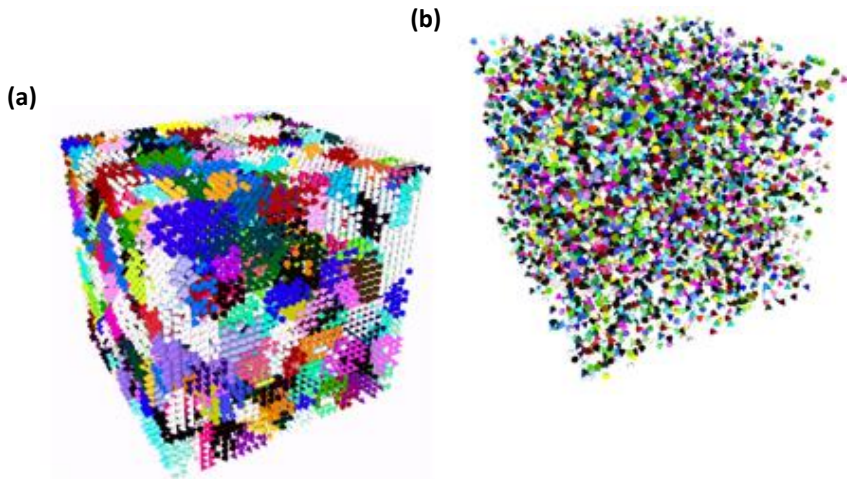


**Fig.3.35:** (a) The matrix and (b) the crystalline elements are represented with cones with different colors indicating the directions of the anisotropy easy axis.

The crystalline phase is described with bulk parameters, i.e., exchange stiffness of  $12 \text{ pJ/m}$ , saturation magnetization of  $85 \text{ A m}^2 \text{ kg}^{-1}$ , and cubic anisotropy of  $290 \text{ KJ/m}^3$ , with a random direction of easy axis in each 3 nm element. For the amorphous phase, the parameters are defined according to the experimental observations collected from structural (XRD, TEM) and magnetic (SQUID magnetometry, Mössbauer spectroscopy) measurements. While the saturation

magnetization of the amorphous matrix was not directly experimentally accessible, a starting value has been estimated through the fit of the high field part of the  $M(H)$  curve with the law of approach to saturation (LAS). We have used it as a suggestion for a reasonable interval of confidence for the saturation magnetization of the sample. Taking into account also the canting angle from the Mössbauer measurement and the relative experimental error, this range was estimated between about 40 and 60  $\text{A m}^2 \text{kg}^{-1}$ . Considering that the crystalline fraction represents a fully collinear structure and the amorphous phase is the canted one, the saturation magnetization of the amorphous matrix ( $M_{\text{Smatrix}}$ ) should be between  $\approx 30$  and  $50 \text{ A m}^2 \text{kg}^{-1}$ . Hence, the only real free parameter was the magnetic anisotropy, optimized with  $M_{\text{Smatrix}}$  to reproduce the experimental  $M(H)$  curve recorded at 5 K. A simulation at 8 T has been also performed as a further validation of the model. The best result illustrated in **Figure 3.36a** was obtained using  $M_{\text{Smatrix}} = 38 \text{ A m}^2 \text{kg}^{-1}$  and using a log-normal distribution of magnetic anisotropy values with a mean of  $3.0 \text{ MJ/m}^3$  and standard deviation of  $2.0 \text{ MJ/m}^3$ , resulting in a mode of  $1.7 \text{ MJ/m}^3$  (**Figure 3.36b**). The obtained results suggested that the applied field allows the magnetization reversal of a small part of the amorphous matrix and an irreversible contribution was given by a large part of the sample responsible for the large coercive field measured and the unsaturation of the sample, (**Figure 3.36c**).

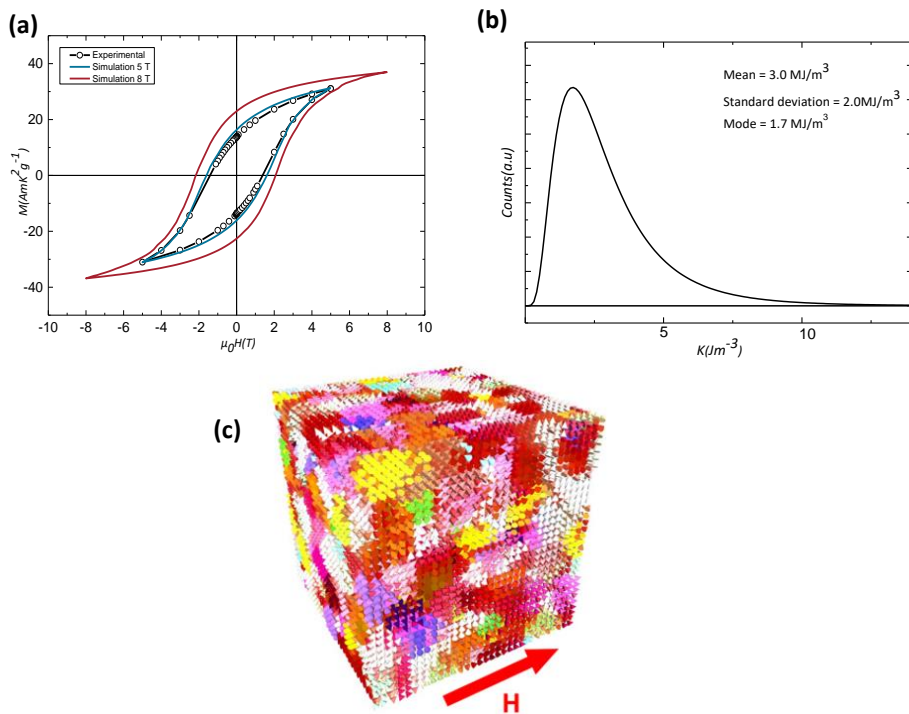


**Fig.3.36:** (a)  $M(H)$  curves obtained averaging over 10 different simulation seeds is compared to the experimental curve, (b) Optimized anisotropy constant distribution for the amorphous grainy matrix and (C) micromagnetic model with an applied field of +5 T (direction indicated by the red arrow), the sample is not fully saturated (full saturation along the field direction indicated with red color).

Individual simulations were performed to investigate the role of the coupling between the component. The simulations have been carried out by removing exchange and dipolar interactions contributions. This corresponds to minimal effects. In all the cases, the coercivity has a slight tendency to increase, since all three interactions have a weak effect on reducing the role of the individual amorphous grains high anisotropy averaging down the effective anisotropy value (**Figure 3.37a**). On the other hand, the exchange between crystalline and amorphous elements plays the main role. With its strong magnitude, it induces a single-phase magnetic behavior. In the absence of this exchange, a double phase magnetization reversal is strongly evident, with a low reversal field for the

crystalline grains and only partial reversal of the matrix in the range of magnetic field used (**Figure 3.37b**).

The model also has been verified by attributing the large anisotropy to the crystalline phase and the low like value to the matrix in the simulation. As shown in **Figure 3.37b**, this will lead to an easy saturation at 5 T with no residual canted structure. On the other hand, the low fraction of crystalline elements will not lead to the large coercivity measured, despite the large value of anisotropy used, compatible with what experimentally observed for similar individual particles with large surface anisotropy [164].

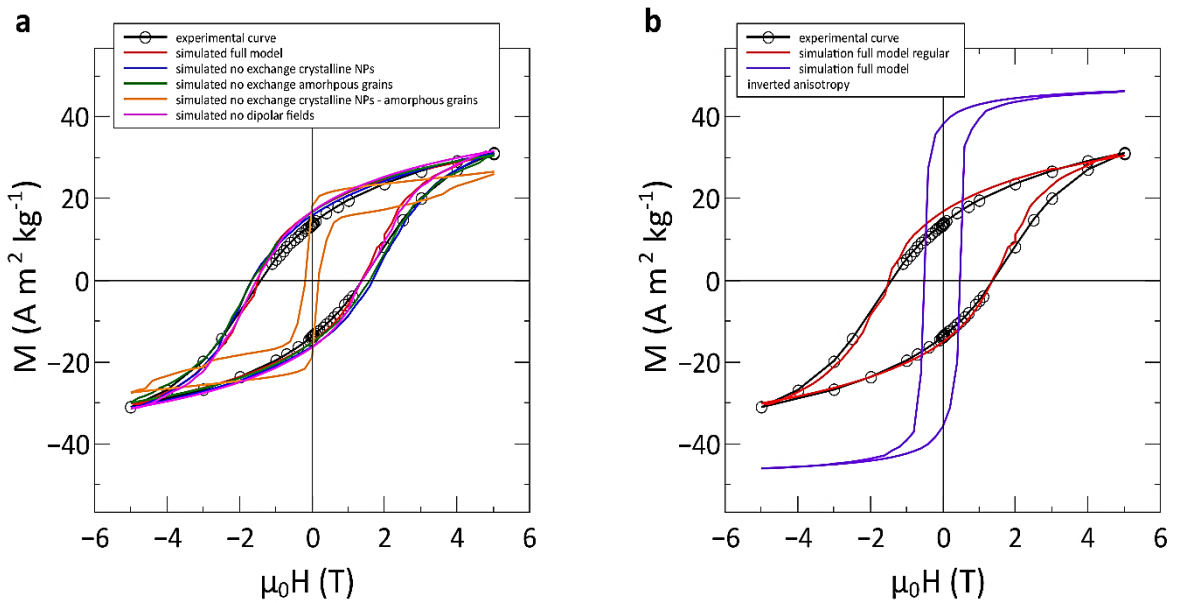


**Fig.3.37:** (a) The experimental curve (black circles and line) is compared to the simulated one using the full model (red line) and with removing exchange contribution among crystalline elements (blue line), among amorphous grains (green line), between crystalline and amorphous components (orange line), and turning off the dipolar fields (magenta line). (b) The experimental curve (black circles and line) is compared with the simulated one using the full model (red line) and an equivalent one with inverted anisotropy between the crystalline and amorphous phase (purple line).

### 3.6 Chapter conclusions

The design of magnetic hybrid materials through adequate engineering of the different constituent compositions can offers an inexpensive route for their optimization for different applications. We present a review of the state of the art of the research on hybrid materials in literature, followed by a more specific classification of hybrid magnetic materials and a brief description of each class. We continue with an investigation of the magnetic properties of magnetic nanoparticles (MNPs) /mesoporous silica (MS) hybrid material. Two studies have been reported with two different magnetic cores:  $\text{CoFe}_2\text{O}_4$  and  $\text{Fe}_3\text{O}_4$  prepared with polyol and coprecipitation synthesis method respectively. Finally, we have shown the novel physics and the potential technological perspectives involved in crystalline -amorphous cobalt ferrite nanocomposite, which may provide clues for to the development of advanced magnetic nanoparticles-based hybrid materials.

We have first synthesized the magnetic core, (i.e., spinel iron oxide nanoparticles by coprecipitation methods. We conclude that the magnetic properties of single particles can be tuned by changing the synthesis parameters. Very different saturation and coercive field values are observed in cobalt-doped magnetite nanoparticles, almost all of which favor an increase in magnetocrystalline anisotropy and saturation magnetization. There is no correlation between particle size and Co doping (up to 50%), which is not surprising since Cobalt has an ionic radius comparable to iron (0.074 and 0.077 nm for Co (II) and Fe (II) in octahedral coordination, respectively). However, this is interpreted as a consequence of the specific cationic distribution due to the partial substitution of  $\text{Co}^{2+}$  ions in the spinel structure.

On the other hand, we studied the effect of temperature and atmosphere. We have shown that the shape of the particles can be changed by varying the reaction atmosphere, as indicated by the TEM observations in **Figure 3.13**. As the reaction atmosphere changes, the magnetite particles change shape from a quasi-spherical particle to a faceted one, while the magnetic properties are

similar within the experimental error. The final product was significantly affected by the abrupt way of base addition that leads to a pH gradient within the solution, then to the formation of lepidocrocite( $\gamma$ -FeOOH) as an intermediate to form spinel iron oxide nanoparticles. However, the presence of nitrogen as a reaction atmosphere, decrease the Fe<sup>2+</sup>/Fe<sup>3+</sup> oxidation rate favoring then the formation magnetite/maghemite directly, which results in more regularly shaped particle.

For the magnetite nanoparticles prepared under controlled atmosphere (N<sub>2</sub>), the pattern in XMCD observation in **Figure 3.16**, indicates that the resulting structure is formed by about 2/3 of Fe ions reside in a local environment close to that of  $\gamma$ -Fe<sub>2</sub>O<sub>3</sub> and about 1/3 close to that of Fe<sub>3</sub>O<sub>4</sub> local structure. This result is also in agreement with the low isomer shifts ( $\delta$ ) values reported in **Table 3.3**.

We discussed the possible effects of the mesoporous silica shell on the magnetic characteristics of the nanoparticles. CoFe<sub>2</sub>O<sub>4</sub> and Fe<sub>3</sub>O<sub>4</sub> nanoparticles, synthesized by polyol and co-precipitation chemical methods, respectively, were chosen to perform this study. Overall, the experimental data proved the obvious effect of the mesoporous silica shell in reducing the interparticle interactions through a 5% increase in the average distance between particles without affecting the saturation magnetization of the magnetic core. Moreover, the magnetic analysis indicates that in the case of the coated Fe<sub>3</sub>O<sub>4</sub> sample, the presence of silica maintains the configuration of partially aligned easy axis (results of the effect of the magnetic stirrer) contrary to the coated CoFe<sub>2</sub>O<sub>4</sub> sample, whose this effect was not observed.

For magnetic hybrid, the physical properties are usually determined by the combination of the properties of each constituent. Generally, when two compositions with different phases meet, their properties should be protected and the resulting material can combine both properties. Here we report a new type of magnetic hybrid material composed of crystalline CoFe<sub>2</sub>O<sub>4</sub> with amorphous parent material. This structure leads to large effective anisotropy that prevents the full saturation of the nanocomposite in the range of field +5 T/-5 T as indicated in the magnetization measurements in **Figure 3.31**. Our study

offers a new perspective of the active role of the amorphous phase which can be important for the design of magnetic hybrid materials aiming to multiple technological applications.

The modelling of the crystalline/amorphous cobalt ferrite nanocomposite indicates that the hybrid configuration of the crystalline and amorphous phases exhibits a high magnetic anisotropy value. To the best of our knowledge, this is the first study that reports a hybrid nanoarchitecture combining the crystalline cobalt ferrite with the amorphous parent material and confirms the active role of the amorphous phase, presenting a large part of the total moments. A value with a mean of  $3.0 \text{ MJ/m}^3$  and a standard deviation of  $2.0 \text{ MJ/m}^3$ , resulting in a mode of  $1.7 \text{ MJ/m}^3$  are theoretically obtained. From the micromagnetic results, we also conclude that the exchange between the crystalline and amorphous matrices is strong enough to produce rigid exchange-coupled composites and can preserve the coupling to an extremely long range, therefore the amorphous structure can no longer be considered as an undesirable product but can be seen as an integral element, where it achieves the quality of a very hard medium that cannot be found in the parent crystalline material.

## Surface and Interface Magnetism: The Role of Molecular Coating

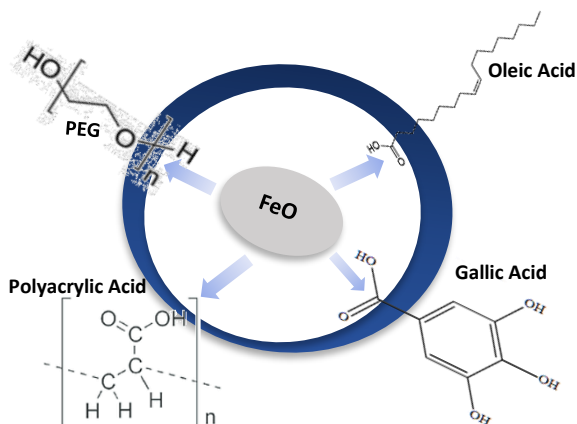
**M**agnetic nanoparticles functionalization have been proposed in the literature for different purposes, as efficient catalysts [165], enhanced storage capacity [166], etc. Particularly, in the field of nanomedicine, functionalization of magnetic nanoparticles is considered as an essential step to improve the biocompatibility and the delivery of molecules [167–169]. However, the effect of surface modification at nanoscale becomes more significant and can strongly affect the whole magnetic behavior of the material. In some cases, a clear effect of surfactant on the hysteresis parameters have been reported [170,171]. In general, the reduction in particle size leads to the breaking of lattice symmetry, which creates incomplete atomic coordination with respect to the bulk state and the inner core of the particle. This can induce a disordered surface structure that contributes to the magnetic properties of the material. On the other hand, as a way to control the surface structure, molecular coating can be considered as a good strategy based on the interaction of the nanoparticle surface with another phase that can replace the missing bonds. Depending on the type of molecules used, i.e., functional group, chain length, and electron donating ability, different magnetic properties can be obtained [172,173].

In this framework we study in this chapter, the effect of molecular coating to tune the magnetic properties of a given material. Here we introduce a deep investigation of superficial modified magnetite nanoparticles prepared with the co-precipitation method. We choose to work with different type of ligands, in order to investigate the effect of the coating that shows a notable change in the features of the materials based on the interaction between the ligand and the nanoparticle surface. The study is divided in two sections: The first section investigates the effect of coating using mono and multi shell of different polymers and oleic acid on  $\text{Fe}_3\text{O}_4$  nanoparticles and the second section is devoted to the effect of using DNA molecules. Furthermore, we report the relationship between the colloid stability and the magnetic properties of some investigated samples.

## 4.1 Role of organic coating to tune the magnetic properties

### 4.1.1 Ligand exchange process

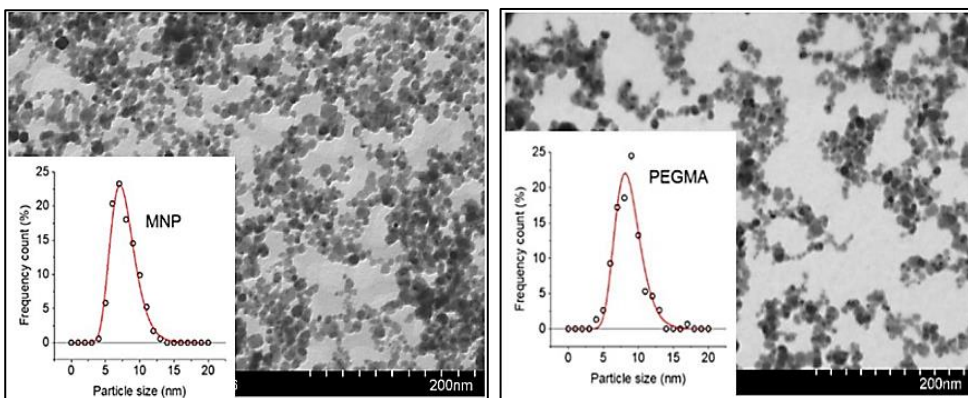
To perform this study, magnetite nanoparticles were prepared by co-precipitation method (details in section 3.3.1) then coated with polyacrylic acid (PAA, Mw = 1800 Da), gallic acid (GA), oleic acid (OA) and polyethylene glycol (PEG, Mw =4000 Da)[174,175]. In brief, the samples were labelled as PAA@MNP, PGA@MNP, OAOA@MNP, PEG-OA@MNP and PEGMA@MNP). For the coating process 1 mmol PAA, 1 mmol PGA, 1mmol PEGMA, 2 mmol OA and 5 mmol PEG were used. In particular, for PEG-OA@MNP sample, the coating process was performed in two main steps: after their synthesis, magnetic nanoparticles were initially coated by oleate layer, then the PEG molecules were attached to the surfacted particles. Since as a part of our study is to investigate the probable mutual relationship between the colloid stability and the magnetic properties, the ligands above have been chosen accordingly to further facilitate the electrosteric stabilization of the materials in aqueous medium.



**Fig.4.1:** Schematic presentation magnetite nanoparticles (FeO) with different ligands.

#### 4.1.2 Morphological Study

Results of Transmission electron microscopy (TEM) analysis are illustrated in **Figure 4.2**. TEM image of uncoated sample indicate the presence spherical-shape nanoparticles with an average particle size = 10(1) nm (details in section 2.2). After coating, no change in the average particle size is determined, due to the used mild chemical conditions (pH~6.5, 10mM NaCl) in the absorption process, preserving the original structure of the magnetic core.



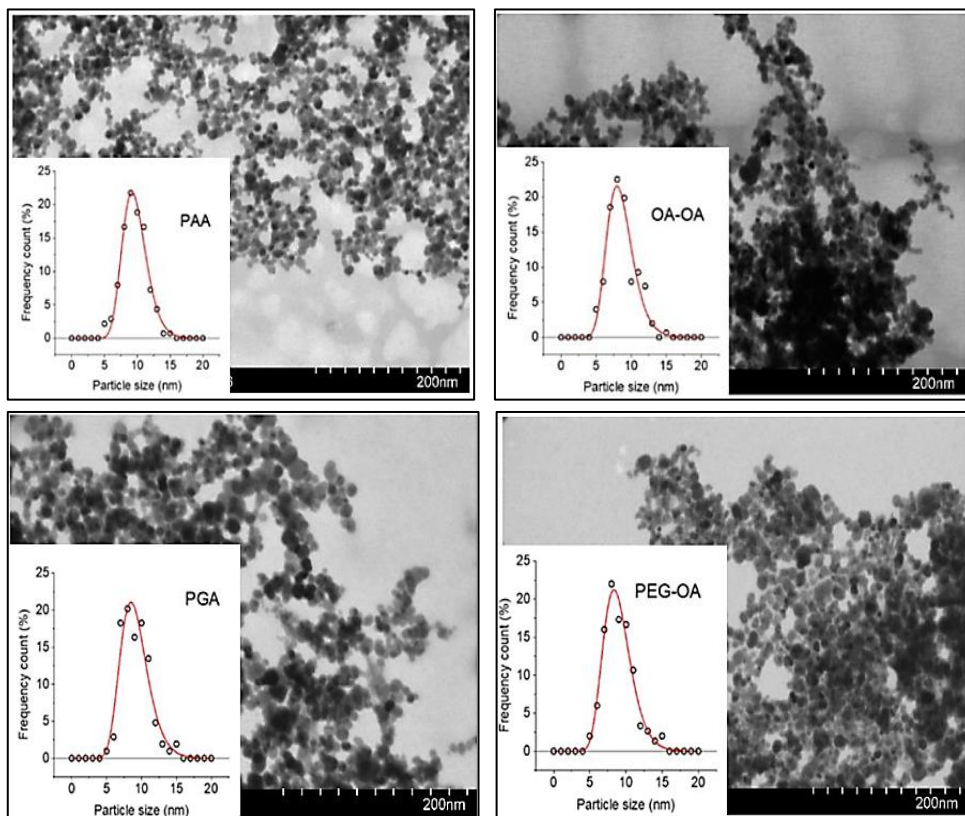


**Fig.4.2:** TEM analysis of bare and coated FeO nanoparticles.

#### 4.1.3 Effect of organic coating: investigation of the magnetic properties

The magnetization of bare and functionalized magnetite nanoparticles as a function of the applied magnetic field has been presented in **Figure 4.3**.  $M$  vs  $(H)$  carried out at 5K for MNPs, PAA@MNP and PGA@MNP samples show similar hysteresis parameters (**Table 4.1**) within the experimental error, suggesting that the molecular coating in this case doesn't affect the magnetic features of the nanoparticles. Whereas measurements on OA-OA@MNP, PEG-OA@MNP and PEGMA@MNP show similar behaviour and values among them but significant change than to bare nanoparticles. The difference in

magnetization is ascribed to structural changes in the magnetization configuration induced by the chemical composition of the coating molecules. In presence of oleic acid (OA) The carboxylic acid terminal group, -COOH, can react with iron oxides and form a magnetically disordered layer [171,176] that can lead to a decrease of the magnetization with respect to the bulk value [177–179]. However, for MNPs@PAA and MNPs@PGA, the coating molecules take the positions of the missing oxygen atoms, making the symmetry and the crystal field of the surface closely resembling to that of the uncoated magnetic core and therefore reduces the spin disorder. In contrary, for MNPs@PAA and MNPs@PGA, coating molecules take the positions of the missing oxygen atoms, making the symmetry and the crystal field of the surface closely resembling to that of the uncoated magnetic core and therefore reduces the spin disorder.

The coercivity trend at low temperature is not straightforward to understand. The expected coercivity for the samples MNPs@OA-OA, MNPs@PEG-OA would be higher than that for MNPs@PAA, MNPs@PGA and MNPs@PEGMA samples. A similar interpretation of this difference would be the noticeably larger  $X_d$  values for MNPs@OA-OA, MNPs@PEG-OA and MNPs@PEGMA samples, which are in agreement with our interpretation, that these samples present more magnetically disordered layer, results in lower saturation magnetization  $M_s$ .

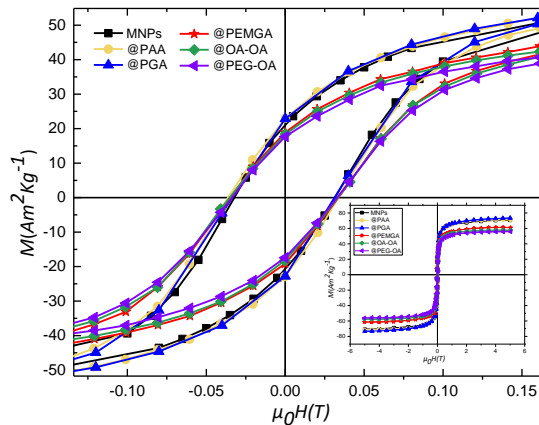


**Fig.4.3:** Magnetization versus field curve measured at 5 K of bare and coated nanoparticles.

Sample	$M_s$ ( $\text{Am}^2\text{Kg}^{-1}$ )	$H_c$ (mT)	$\chi_d$ ( $\text{Am}^2\text{Kg}^{-1}$ )
MNP	72.6(1)	320	2.0(3) E-5
@OA-OA	60.3(6)	351	8.5(2)E-5
@PAA	72.5(2)	361	3.6(2)E-5
@PEG-OA	57.6(2)	335	7.7(2)E-5
@PEGMA	62.3(6)	348	6.1(2)E-5
@PGA	72.1(1)	320	2.7(3)E-5

**Tab.4.1:** The saturation magnetization  $M_s$ , the coercive field ( $H_c$ ), and the susceptibility for all samples are compared.

#### 4.1.4 Interparticle Interactions

Furthermore, the analysis of  $\Delta M$  plots for MNPs, PAA@MNPs and PEG-OA@MNPs indicates that the surface coating modulates the interparticle interactions, **Figure 4.4**. The obtained results show a strong negative deviation for all samples, indicating the prevalence of magnetic dipolar interactions, with large signal for bare particles, then PEG-OA and PAA coated particles respectively. This corresponds to the effect of coating layer on the distance between magnetic nanoparticles.

Since in all the investigated samples, the used magnetic nanoparticles are coming from the same synthesis batch, the observed change in the interparticle intensity is due to the change in the particles distance, as the chain length of the coating molecule increase as the distance between the particles increases.

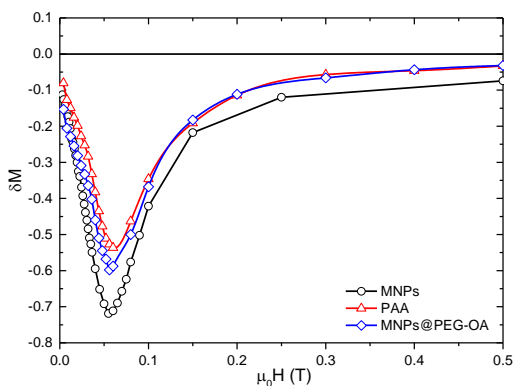


**Fig.4.4:**  $\Delta M$  plots

#### 4.1.5 Mutual relationship between the colloid stability and magnetic properties

Most of the research carried out on the effect of molecular coating on colloidal stability mainly based on the chemical explanation but the probable mutual relationship between the colloid stability and the magnetic properties was not deeply discussed. Accordingly, the colloidal stability was investigated as a function of the time, and a series of photographs were taken of all the dispersions as illustrated in **Figure 4.5**, starting from dispersions in mild chemical conditions (pH~6.5, 10mM NaCl) to strong saline medium to demonstrated the large influence of the change in the magnetic properties on the colloidal stability. After one hour and at low salt content all the samples (bare and coated particles) show deep, brown dispersions implying that all the samples retain their stability and no precipitation have been detected. As the salt concentration increases, bare MNP and OA-OA@MNP are destabilized, while an homogeneous aspect still observed in case of the other samples. This change is ascribed from one side to the homoaggregation processes that take place upon salt-induced charge screening, which results in the formation of aggregates of a broad size distribution and a concomitant variation of their linear settling velocities, and on the other side to the strong interparticle interactions reported by these two samples. Maintaining the strong saline conditions (500 mM), as time evolution, further changes in the visual appearance of MNP dispersions occurred, however PAA@MNP still retaining its colloidal stability after 45 days, which can be attributed to the low interparticle interactions that this sample present. Due to their high surface energy, magnetic nanoparticles tend to adhere to each other in order to reduce their surface energy results in increase in the magnitude of the dipole-dipole energy among themselves, thus to the presence of agglomeration that is almost unavoidable in presence of high magnitude of dipole-dipole interactions [180,181], which explain the good colloidal stability of some samples than others in our study.



**Fig.4.5:** Photographs of undisturbed magnetic nanoparticle dispersions.

## 4.2 Magnetic nanoparticles coated with DNA molecules: study of the magnetic properties

This research study has been carried out in collaboration of University Norwegian University of Science and Technology (NTNU), Norway. 10 nm magnetite nanoparticles synthesized with co-precipitation and functionalized with DNA molecules is investigated. After the synthesis of magnetite nanoparticles, and to insure the bonding of the DNA, particle surface was first positively charged with tetramethylammonium hydroxide solution (TMAH) then coated with DNA molecules, followed by silanization. A more detailed description about the morphostructural characterization can be found elsewhere [182].

### 4.2.1 Magnetic Properties

Magnetization measurements versus magnetic field has been recorded at 5 and 300K. At 5k (**Figure 4.6a**) bare magnetite (Mag) nanoparticles and coated magnetite (Mag\_TMAH, Mag\_DNA and Mag\_Silica) show similar hysteresis parameters (i.e.,  $M_s$ ,  $H_c$ ) within the experimental error (**Table 4.2**), suggesting that the coating process was successfully achieved without affecting the characteristics of the magnetic core. At 300K, superparamagnetic behavior (i.e.  $M_r=0$  and  $H_c=0$ ) have been reported for bare and coated nanoparticles as illustrated in **Figure 4.6b**.

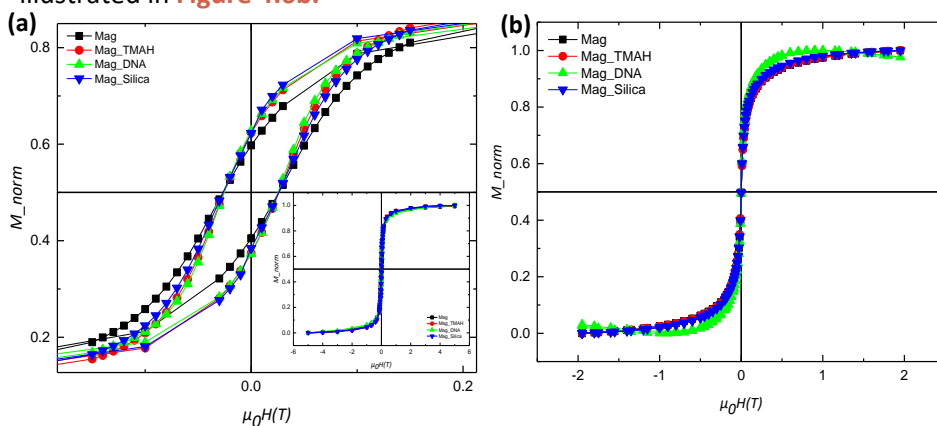


**Fig.4.6:** M vs (H) for bare and coated nanoparticles measured at (a) 5K and (b) 300K.

Sample	$M_S$ ( $\text{Am}^2\text{Kg}^{-1}$ ) 5K	$H_C$ (mT)	$T_{\text{max}}$ (K)	$T_{\text{irr}}$ (K)	$T_B$ (K)
Mag	77(8)	26(2)	228(22)	283(28)	90(9)
Mag@TMAH	75(8)	25(5)	236(23)	243(24)	92(9)
Mag@DNA	85(9)	25(2)	202(20)	207(20)	92(9)
Mag@Silica	83(9)	20(2)	228(22)	242(24)	102(10)

**Tab.4.2:** The saturation magnetization  $M_S$  at 5K, the coercive field ( $H_C$ ), Temperature corresponding to the maximum in ZFC curve ( $T_{\text{max}}$ ), irreversibility temperature ( $T_{\text{irr}}$ ) and blocking temperature estimated from  $M_{\text{FC}}-M_{\text{ZFC}}$  curve, uncertainties on the last digit are given in parentheses.

#### 4.2.2 Effect of DNA coating: Interparticle Interaction

To shed light on the possible scenario of interparticle interactions, we have analyzed the variation of  $\Delta M$ -plots. **Figure 4.7a** indicates that before coating, magnetite nanoparticles show the presence of the dipolar interactions. After coating the dominance of dipolar interactions still observed, however after DNA coating a significant reduction of the peak intensity (as absolute value) can be seen, reflecting the increase of interparticle distance, which confirms the efficiency of the coating process. Interaction field values of -16.89; -13.275; -4.265 mT were obtained for Mag, Mag\_TMAH ; Mag\_DNA respectively, **Figure 4.7b** . These results can be explained by the change in the interparticle distance we obtained a value of 1.016, 1.041 and 0.934 for Mag, Mag\_TMAH ; Mag\_DNA and Mag\_Silica respectively. This confirms that the average interparticle distance increases after coating process by 1% and 4% for Mag\_TMAH and Mag\_DNA samples, while for Mag\_Silica sample a decrease in the interparticle distance by 6% was reported. The behavior of the Mag\_Silica was not expected, and more investigation of this sample still required.

The presence of interparticle interactions have been also confirmed by the flat plateau at low temperature in FC curves, **Figure 4.7c**

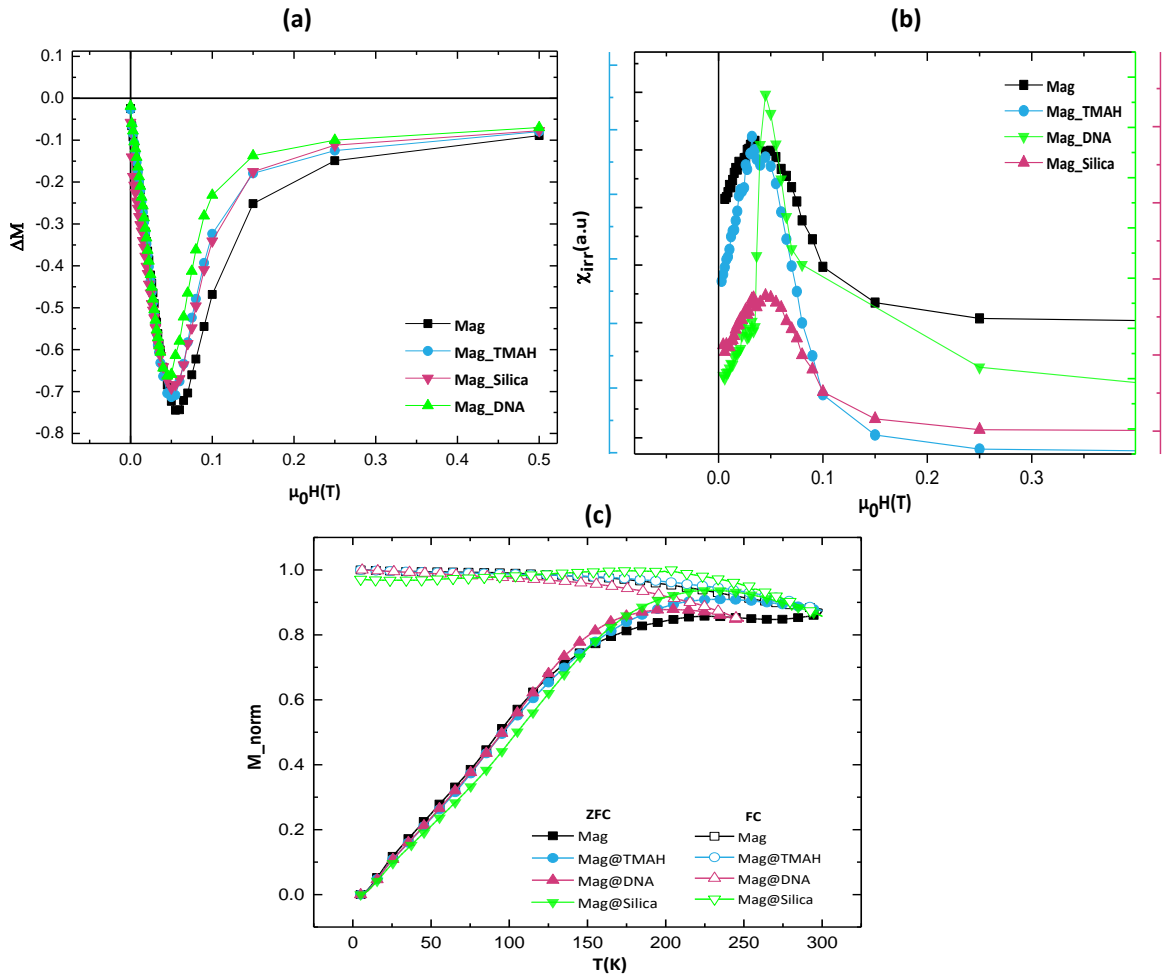


**Fig.4.7:** (a)  $\Delta M$  plots, (b) irreversible susceptibility ( $\chi_{irr} = dM/dH$ ) derived by DCD, (c) ZFC (Full symbols) and FC (empty symbols) curves measured with an applied field of 2.5 mT.

### 4.3 Chapter conclusions

To conclude, the magnetic study on 10 nm magnetite coated with different ligands (i.e., PAA@MNP, PGA@MNP, OAOA@MNP, PEG-OA@MNP, and PEGMA@MNP) proved that depending on the type of ligand used, i.e., functional group, chain length, and electron donating ability, different magnetic properties are obtained. For example, PAA@MNP, PGA@MNP samples show a  $M_s$  similar to that of the bare sample, while OAOA@MNP, PEG-OA@MNP samples show a decrease in saturation after the coating, which is attributed to structural changes in the magnetization configuration induced by the chemical composition of the coating molecules.

In a study carried out after 45 days on the colloidal stability of the coated samples (**Figure 4.5**), we have highlighted the mutual relationship between the colloid stability and the magnetic properties, which was directly affected by the presence of high magnitude of dipole-dipole interactions in some samples.

we have discussed the possible effects of surface modification with DNA molecule. The magnetic properties of magnetite sample coated with DNA molecule followed by silanization were investigated at each step of the coating process. we have determined the occurrence of significant changes in the interparticle interactions after each coating step, due to the increase in the interparticle distance by a percentage of 1% and 4% with respect to the pre-coated magnetite sample as demonstrated by  $\Delta M$  plots, **Figure 4.7a**.

## Interaction Magnetic Core-Magnetic Field

The objective of this chapter is to develop and demonstrate a system for laboratory experiments under dynamic conditions. The system is based on the testing of magnetic materials prepared to deliver and/or harvest molecules for specific applications by simulating real-world conditions. This experimental setup gives the possibility to integrate different magnet configurations to characterize the magnetic signature of the materials. The data processing and analysis processes have been developed to reduce or suppress noise signatures and maximize detection thresholds.

Initial stages involved defining the used permanent magnets, configurations optimization (i.e., 2D simulation), that would lead to get better results. Particularly for this chapter, we report preliminary experimental measurements performed with our circuit (with and without external magnetic field), on a solution of  $\text{Fe}_3\text{O}_4$  nanoparticles that were prepared in our group.

## 5.1 Experimental motivation

The motivation of the performed experiments comes from the fact that the control of magnetic materials through an applied magnetic field (i.e., harvesting and delivering molecules) in different applications always based on the trials to optimize the magnetic properties of the material. Here we prove also that by optimizing the magnetic configuration, better control we get. We follow by testing our system magnetic nanoparticles-permanent magnet for harvesting/delivering molecules using a homemade dynamic circuit. In addition, this study is performed as the final part of my thesis topic.

## 5.2 Magnetic nanoparticle in a magnetic field

The magnetic force acting per unit volume on a set of nanoparticles subjected to a magnetic field is given by:

$$F_M = C \frac{4\pi a^3}{3} \frac{\mu_0 \chi}{\left(1 + \frac{\chi}{3}\right)} \left[ \frac{d\vec{H}}{dx} \right] \vec{H} \quad (5.1)$$

C is the particles concentration, H is the applied magnetic field,  $\frac{d\vec{H}}{dx}$  is the gradient of the field and  $\chi$  is the susceptibility. In order to evaluate the magnetic force required to concentrate nanoparticles at a point, several factors must be taken in consideration, the flow velocity, the particles diffusion etc. The concentration over time of nanoparticles inside a vechial at a given point is expressed by [183] :

$$\frac{dc(x, y, t)}{dt} = -\vec{v} \left[ -D_{tot} \vec{\nabla} C + C \vec{V}_B(y) + Ck \vec{\nabla} (|\vec{H}(x, y)|^2) \right] \quad (5.2)$$

The first term is related to total diffusion, the second to liquid convection, and the third to the magnetic field. Generally, three type of magnets can be used to produce the magnetic field: electromagnets, superconducting magnets and permanent magnets. The best choice depends on overall costs, size and achievable profiles for the magnetic field and its gradient. For our experiment NdFeB permanent magnets were used.

### 5.3 Permanent Magnets

Permanent magnets are generally ferromagnetic, magnetized materials/alloys. There are different "grades" of them, whose identification number defines the intensity of the produced magnetic field. They have very high coercive field, to prevent the demagnetization of the magnet. The advantage of using permanent magnets in our experiment lies in their small size (even a few mm), which makes them very practical to be used for in vivo measurements. With permanent magnets it's also possible to build different configurations of multiple magnets as a way to increase the magnetic field strength and the field gradient [184].

### 5.4 Optimal Configuration of Magnets

To achieve good control over nanoparticles, in addition to susceptibility, the product between the magnetic field and its gradient must be also maximized. Accordingly, several configurations were investigated to increase the magnetic force; only good configuration results are reported here. All the reported calculations have been performed using the following formulas:

$$\vec{\nabla}(B_z) = \left( \frac{\Delta B_z(x)}{\Delta x}, \frac{\Delta B_z(y)}{\Delta y} \right) \quad (5.3)$$

$$|\vec{\nabla}(B_Z)| = \sqrt{\left(\frac{\Delta B_Z(x)}{\Delta x}\right)^2 + \left(\frac{\Delta B_Z(y)}{\Delta y}\right)^2} \quad (5.4)$$

$$B_Z \cdot |\vec{\nabla}(B_Z)| = B_Z \cdot \sqrt{\left(\frac{\Delta B_Z(x)}{\Delta x}\right)^2 + \left(\frac{\Delta B_Z(y)}{\Delta y}\right)^2} \quad (5.5)$$

Two configuration of cubic magnets South-South (SS) and North-South (NS) are investigated, **Figure 5.1**. NS configuration shows the highest values, **Table5.1**, suggesting that this configuration can exert a higher magnetic force on the magnetic nanoparticles than SS configuration.

Configuration	$\max( \mathbf{B}_Z \cdot \text{grad}(\mathbf{B}_Z) )$ $\mp 0.1 \times 10^4 (\text{G}^2/\text{mm})$
SS	$1.3 \times 10^7$
SN	$1.4 \times 10^7$

**Tab.5.1:** obtained Values from the different configuration (Z=0).

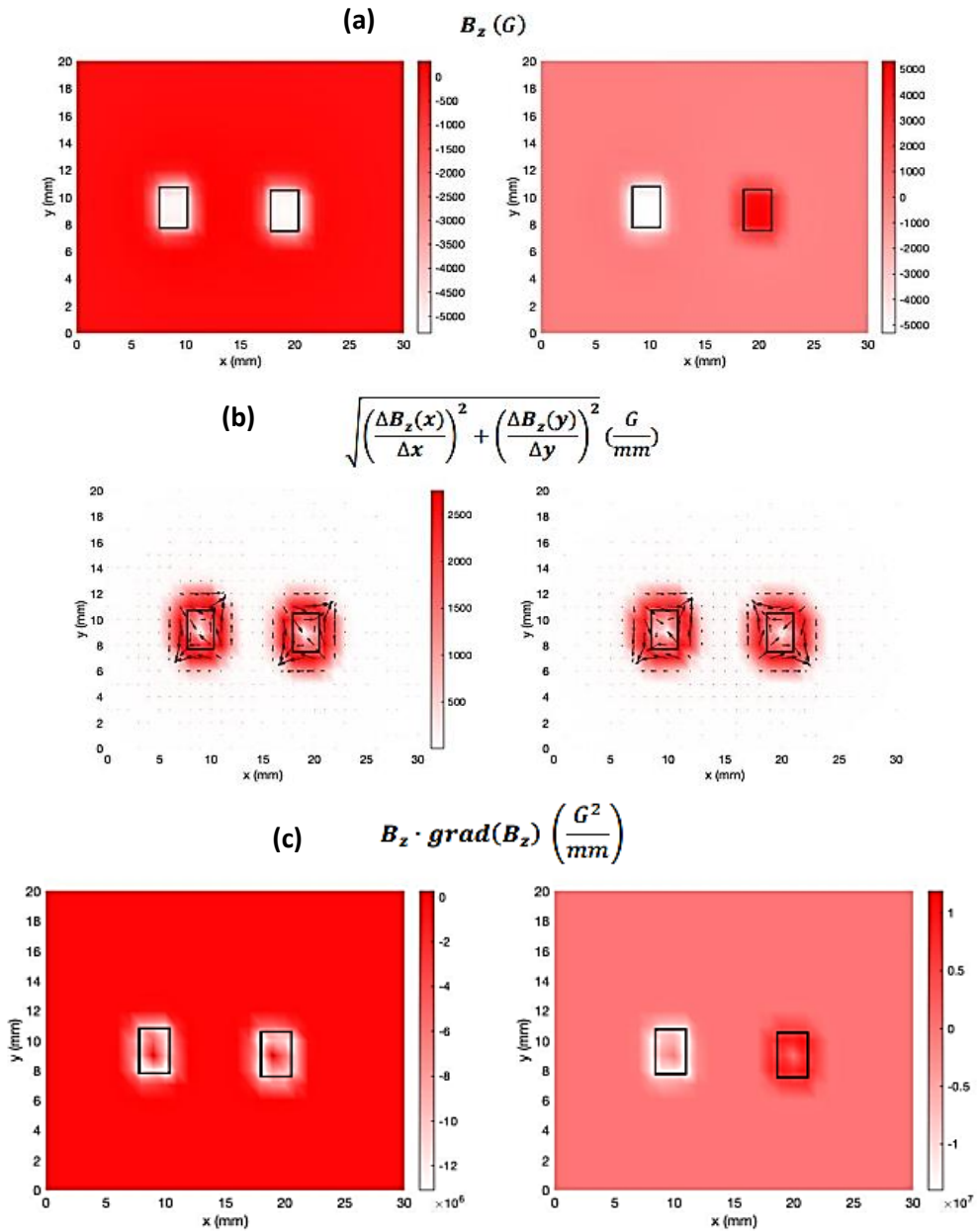


**Fig.5.1:** (a) magnetic field flux, (b) field gradient and (c) product between the flux and the gradient performed on a pair of cubic magnets at  $Z=0$ .

## 5.5 Circuit for experiments in Dynamic Condition

A circuit for simulation in a dynamic condition was made to test the efficacy of our materials for the delivery and harvesting process. The homemade circuit is shown in **Figure 5.2a**. Measurements of six hours, using an aqueous solution of magnetite, with a concentration of 0.025 g/L, was performed and absorbance measurement is collected each quarter of an hour for more modeled trend.

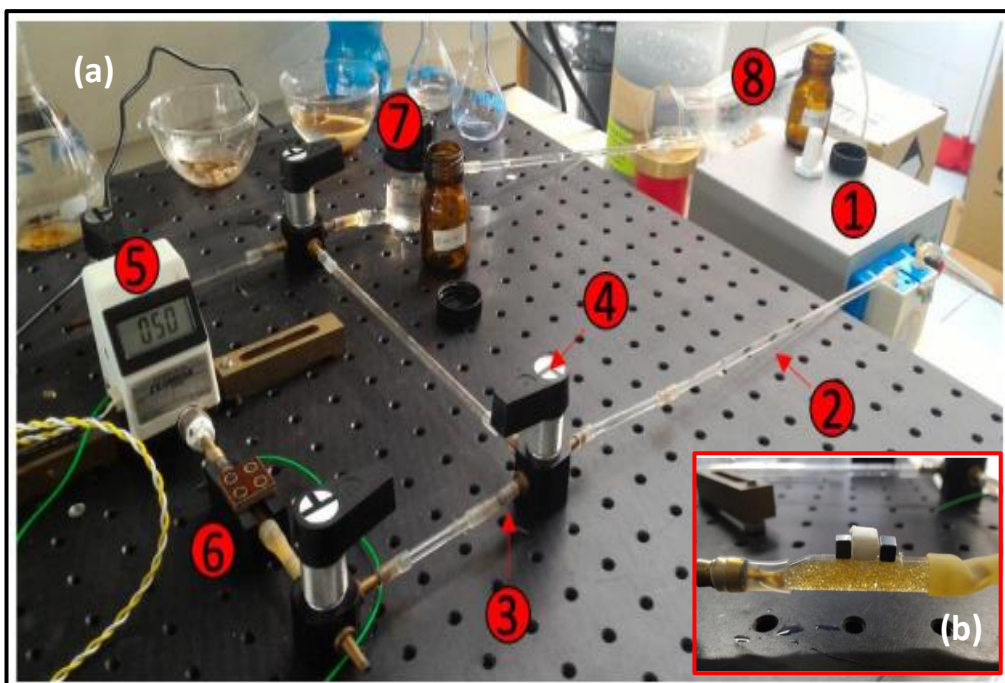


**Fig.5.2:** (a) homemade circuit for simulation in dynamic condition, (b) NS configuration consisting of a pair of magnets with PTFE separator.

- |   |  |
|---|--|
| (1) Peristaltic pump (VELP® Scientific SP311) | (5) Flowmeter (OMEGA® FLR 1000-9D)                               |
| (2) Glass tubing (internal diameter 2 mm)     | (6) Glass simulation of an animal organ and magnet configuration |
| (3) Rubber tubing (for connection)            | (7) Solution withdrawal site                                     |
| (4) Taps                                      | (8) Solution Container   |

Experiments are reported with and without NS configuration (studied in the section above) attached to the surface of the organ, **Figure 5.2b**. Experimental data with two different flow speed were modeled using two types of fits: exponential and rational, i.e., given by the ratio of two polynomials of first degree in the time characterized by different proportionality coefficients:

$$C(t) = 1 - e^{(-b_e \cdot t)} \quad \text{exponential} \quad (5.6)$$

$$C(t) = 1 - \left[ \frac{(a_r \cdot t) + b_r}{(c_r \cdot t) + b_r} \right] \quad \text{rational} \quad (5.7)$$

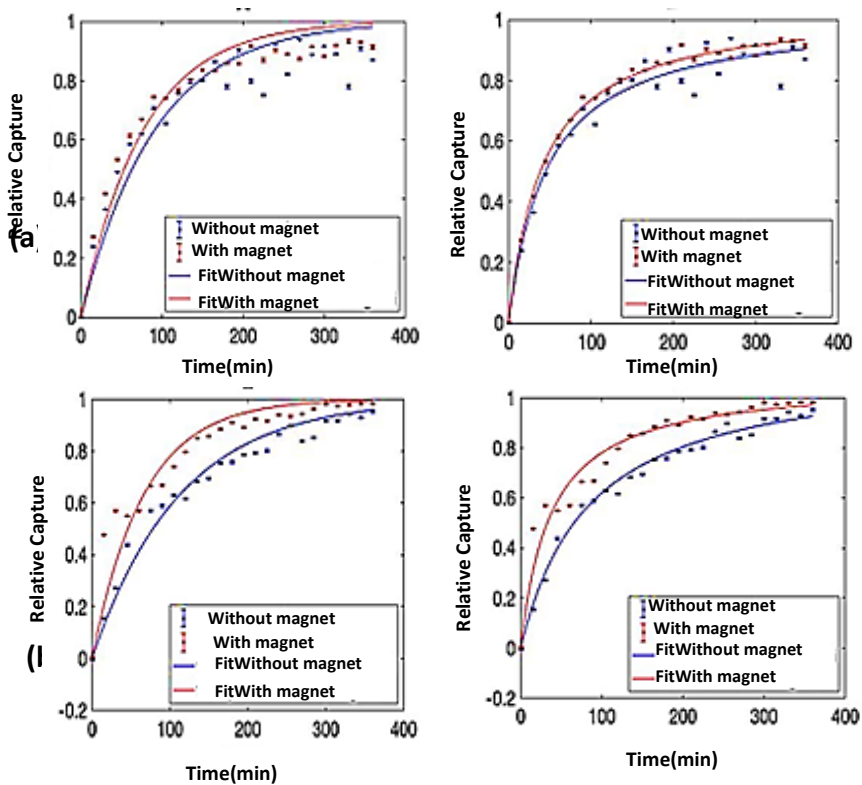


**Fig.5.3:** fitted data with and without magnets, with a flow rate of (a) 55ml/min and (b) 25 ml/min.

## 5.6 Chapter conclusions

To summarize, this chapter introduces a theoretical investigation of permanent magnets with cubic geometry disposed in different configurations. Specifically, we have focused on the study of the magnetic field strength and its gradient for optimal performance for each proposed configuration.

A quantitative characterization of the response of solution of magnetic nanoparticles in presence of magnetic field (i.e., with the best obtained configuration of magnets) has been carried out using a home-made circuit, along with the development of a simple method for data treatment that enable to understand the behavior of the nanoparticles under an external applied magnetic field.

To conclude, supplementary investigation and model corrections may be required to provide a higher precision and improvement in the experiments. Thus, help to more understand the magnetic interaction of nanoparticles with an external magnetic field, which can lead to potential improvements in the application areas.

## Conclusions

This thesis focus on the investigation of morphological, structural and magnetic properties of single and hybrid materials based on a spinel iron oxide structure ( $\text{MeFe}_2\text{O}_4$ ; Me:  $\text{Fe}^{2+}$ ;  $\text{Co}^{2+}$ ), in the perspective to tune/design new magnetic properties. Modified Co-precipitation method is used to synthesize  $\text{Fe}_3\text{O}_4$  nanoparticles. We have determined that by the substitution of  $\text{Fe}^{2+}$  with  $\text{Co}^{2+}$  ions leads to a change in the magnetic anisotropy and the saturation magnetization as a result of the new cationic distribution in the spinel structure. Whereas, the change in the reaction atmosphere (nitrogen), magnetite particles show a change in shape from a quasi-spherical particle to a faceted one, while the magnetic properties are similar within the experimental error.

Another way to adjust the magnetic properties is to combine the magnetic phase with another phase, and the coupling between the different phases induces a significant change in the magnetic properties, and sometimes new properties in other cases.

A nanoparticle-based hybrid material was prepared with two different strategies. In the first case, the surface of  $\text{Fe}_3\text{O}_4$  nanoparticles (prepared by co-precipitation) was modified using mesoporous silica, oleic acid, DNA molecules and polymers (e.g. PAA, PEG, PGA). The main results obtained from the field dependence of the magnetization show an equal saturation magnetization within the experimental error for most ligands, while the surface coating with

oleic acid leads to a more magnetically disordered particle surface, resulting in a reduction of the saturation compared to the bare particle. The most common effect in all these samples is the reduction in interparticle interaction, due to the increase in interparticle distance. The interaction field values show an increase of 1%, 4% and 5% for different samples. Moreover, in the case of mesoporous silica, a partial alignment of the easy axis was observed.

In case of  $\text{CoFe}_2\text{O}_4$  prepared with polyol and coated with mesoporous silica no significant change in the magnetic properties is observed, due to the presence of the TEG protection layer.

As a second strategy, we modified the co-precipitation synthesis process of cobalt ferrite nanoparticles by adjusting the pH value (9.5) to promote the formation of a non-stoichiometric hydroxide precipitate in the solution, which leads to a hybrid crystalline/amorphous cobalt ferrite material. The resulting hybrid material exhibits very high anisotropy, a value with a mean of  $3.0 \text{ MJ/m}^3$ . To the best of our knowledge, this is the first study that reports a hybrid nanoarchitecture combining crystalline cobalt ferrite with the amorphous parent material and confirms the active role of the amorphous phase in tuning the magnetic properties.

supplementary investigation of the behavior of magnetic nanoparticle in the presence of magnetic field for possible use of the studied materials in this thesis for delivering and harvesting molecules is performed. We report preliminary results with North-South magnet configuration that show higher magnetic force compared to South-South configuration, and the experiment were preformed using homemade circuit.

## Conclusions (Italian)

Questa tesi si concentra sull'indagine delle proprietà morfologiche, strutturali e magnetiche di materiali singoli e ibridi basati su una struttura di ossido di ferro spinello ( $\text{MeFe}_2\text{O}_4$ ; Me:  $\text{Fe}^{2+}$ ;  $\text{Co}^{2+}$ ), nella prospettiva di progettare nanomateriali ibridi con proprietà magnetiche ottimizzate. Per sintetizzare le nanoparticelle di  $\text{Fe}_3\text{O}_4$  è stato utilizzato il metodo di Co-precipitazione modificato. Abbiamo determinato che la sostituzione di  $\text{Fe}^{2+}$  con ioni  $\text{Co}^{2+}$  porta ad un cambiamento nell'anisotropia magnetica e nella magnetizzazione di saturazione come risultato della nuova distribuzione cationica nella struttura spinello. Mentre, il cambiamento nell'atmosfera di reazione (azoto), le particelle di magnetite mostrano un cambiamento di forma da una particella quasi sferica a una sfaccettata, mentre le proprietà magnetiche sono simili entro l'errore sperimentale.

Un altro modo per regolare le proprietà magnetiche è quello di combinare la fase magnetica con un'altra fase, e l'accoppiamento tra le diverse fasi induce un cambiamento significativo nelle proprietà magnetiche,

Un materiale ibrido basato su nanoparticelle è stato preparato con due strategie diverse. Nel primo caso, la superficie delle nanoparticelle  $\text{Fe}_3\text{O}_4$  (preparate per co-precipitazione) è stata modificata utilizzando silice mesoporosa, acido oleico, molecole di DNA e polimeri (per esempio PAA, PEG, PGA). I principali risultati ottenuti dalla dipendenza dal campo della magnetizzazione mostrano una magnetizzazione di saturazione uguale entro l'errore sperimentale per la maggior parte dei ligandi, mentre il rivestimento superficiale con acido oleico porta a una superficie delle particelle più disordinata magneticamente, con una conseguente riduzione della saturazione rispetto alla particella nuda. L'effetto più comune in tutti questi campioni è la riduzione dell'interazione interparticellare, dovuta all'aumento della distanza tra le particelle. I valori del campo di interazione mostrano un aumento dell'1%, 4% e 5% per diversi campioni. Inoltre, nel caso della silice mesoporosa, è stato osservato un parziale allineamento dell'asse di facile magnetizzazione

Nel caso di  $\text{CoFe}_2\text{O}_4$  preparato con poliolo e rivestito con silice mesoporosa non si osserva alcun cambiamento significativo nelle proprietà magnetiche, a causa della presenza dello strato di protezione TEG.

Come seconda strategia, abbiamo modificato il processo di sintesi per coprecipitazione di nanoparticelle di ferrite di cobalto regolando il valore del pH (9,5) per promuovere la formazione di un precipitato di idrossido non stechiometrico nella soluzione, che porta a un materiale ibrido cristallino/amorfo di ferrite di cobalto. Il materiale ibrido risultante presenta un'anisotropia molto elevata, un valore con una media di  $3,0 \text{ MJ/m}^3$ . Per quanto ne sappiamo, questo è il primo studio che riporta una nanoarchitettura ibrida che combina la ferrite di cobalto cristallina con il materiale genitore amorfo e conferma il ruolo attivo della fase amorfa nella regolazione delle proprietà magnetiche.

Viene eseguita un'indagine supplementare sul comportamento delle nanoparticelle magnetiche in presenza di un campo magnetico per un possibile utilizzo dei materiali studiati in questa tesi per la consegna e la raccolta di molecole. Riportiamo i risultati preliminari con la configurazione del magnete Nord-Sud che mostrano una forza magnetica maggiore rispetto alla configurazione Sud-Sud, e l'esperimento è stato eseguito utilizzando un circuito fatto in casa.

## Publications and contributions

IN THIS SECTION a list of the works published in Peer-reviewed journals during the PhD is included. Oral and poster presentations have been also listed in order to put on the record conferences and important scientific meetings where the work derived from thesis has been spread.

### 7.1 List of publications

1. Alessandra Scano, Edmond Magner, Martina Pilloni, Davide Peddis, Franca Sini, **Sawssen Slimani**, and Guido Ennas. High Energy Ball Milling and Liquid Crystal Template Method : A Successful Combination for the Preparation of Magnetic Nano-Platforms. *J. Nanosci. Nanotechnol.* 21, 2930–2934 (2021).
2. A. Talone, L. Ruggiero, **S. Slimani**, P. Imperatori, G. Barucca, M.A. Ricci, A. Sodo, D. Peddis. Magnetic mesoporous silica nanostructures: investigation of magnetic properties. *Nanotechnology* 31, 465707 (2020). (I.F. 2019: 3.551)
3. Elena Castagnotto, Federico Locardi, **Sawssen Slimani**, Davide Peddis, Laura Gaggero, Maurizio Ferretti. Characterization of the Caput Mortuum purple hematite pigment and synthesis of a modern analogue. *Dye. Pigment.* 185, 108881 (2021). (I.F. 2019: 4.613)
4. M.Smari; R.Hamdi; **S.Slimani**, A.Bajorek; D.Peddis; I.Walha; U.Koneva; E.Dhahri; Yousef Haik . Enhancement of the Magnetotransport Behavior in a Phase-Separated LaAgCaMnO<sub>3</sub>Polycrystalline: Unraveling the Role of a Multi-Double-Exchange Mechanism. *J. Phys. Chem. C* 124, 23324–23332 (2020). (I:F. 2018: 4.309)
5. Anuvansh Sharma, Jan Willem Foppen, Abhishek Banerjee, **Sawssen Slimani**, Nirmalya Bachhar, Davide Peddis and Sulalit Bandyopadhyay. Magnetic Nanoparticles

to Unique DNA Tracers: Effect of Functionalization on Physico-chemical Properties. *Nanoscale Res. Lett.* 16, (2021).(I:F. 2019: 3.581)

6. **Slimani Sawssen**; Concas Giorgio; Congiu Francesco; Barucca Gianni ; Yaacoub Nader ; Talone Alessandro ; Smari Mourad ; Dhahri Essebti ; Peddis Davide ; Muscas Giuseppe. Hybrid Spinel Iron Oxide Nanoarchitecture Combining Crystalline and Amorphous Parent Material. *J. Phys. Chem. C* (2021). doi:10.1021/acs.jpcc.1c00797.(I:F. 2018: 4.309).
7. **S. Slimani\***; C. Meneghini, M.Abdolrahimi, A. Talone, Jean Pierre Miranda Murillo, G. Barucca, N. Yaacoub; P. Imperatori, E. Illés, M. Smari, E. Dhahri and D. Peddis, Spinel iron oxide by co-precipitation method: effect of reaction atmosphere . *Appl. Sci.*, 2021, 11, 5433.(I:F. 2018: 4.309).
8. M. Abdolrahimi, M. Vasilakaki, **S. Slimani**, N. Ntallis, G. Varvaro, S. Laureti, C. Meneghini, K. N. Trohidou, D. Fiorani and D. Peddis. Magnetism of Nanoparticles: Effect of the Organic Coating, *Nanomaterials*, 2021, 11, 1787.(I:F. 2019: 4.446).

## 7.2 Oral and poster presentations

Date	Conference	Abstract
2019-07	<b>XLVII Congresso Nazionale di Chimica Fisica.</b> Rome, Italy.	<b>S. Slimani</b> ; A.Talone ;M. Abdolrahimi; P. Imperatori; M. Smari; E. Dhahri; D.Peddis. Spinel iron oxide nanoparticles synthesized by chemical co-precipitation method: effect of reaction temperature and atmosphere. <b>(Oral)</b>
2019-10	<b>International Conference on smart nanostructured materials: from molecular self-assembly to advanced applications.</b> Rome, Italy.	<b>S.Slimani.</b> Magnetic nanoarchitectures for controlled drugs release <b>(Invited talk)</b>
2020-02	<b>Super Fox Conference on Superconductivity and Functional Oxides.</b> Santa margherita Liguria, Italy	<b>S. Slimani</b> , A. Talone, M. Abdolrahimi, M. Smari, E. Dhahri, D. Peddis . Mesostructured silica/spinel iron Oxides nanoarchitectures: investigation of the magnetic properties. <b>(Oral)</b>
2020-09	<b>Nanoinnovation International Conference</b> Rome, Italy.	<b>S.Slimani.</b> Caput Mortuum pigment : a magnetic investigation <b>(Invited talk)</b>

2020-12	<b>Joint European Magnetic Symposia</b> Lisbon, Portugal.	<b>S.Slimani</b> , A.Talone, L.Ruggiero, P.Imperatori G.Barucca, M A.Ricci, A.Sodo ,D.Peddis . Magnetic mesoporous silica nanostructures: Investigation of magnetic properties. <b>(Oral)</b>
2021-06	<b>Advances in Magnetics Conference-AIM2021.</b> Moena, Italy.	<b>S.Slimani</b> , G.Concas, F.Congiu, G.Barucca N.Yaacoub, A.Talone, M.Smari, E.Dhahri, D.Peddis, G.Muscas . Hybrid spinel iron oxide nanoarchitecture combining crystalline and amorphous parent material. <b>(Oral)</b>
2021-08	<b>International Baltic Conference On magnetism (IBCM): Focus on nanobiomedicine and smart materials.</b> Svetlogorsk, Russia .	<b>S.Slimani</b> , A.Talone, L.Ruggiero, P.Imperatori G.Barucca , M A.Ricci, A.Sodo ,D.Peddis. Magnetic mesoporous silica nanostructures: Investigation of magnetic properties. <b>(Oral)</b>
2021-09	<b>XXVII Congresso Nazionale della Società Chimica Italiana (SCI2021).</b> Italy.	<b>S.Slimani</b> , E.Castagnotto, F.Locardi, L.Gaggero, F.Canepa, D.Peddis, M.Ferretti. Caput Mortuum purple hematite: Investigation of magnetic properties. <b>(Oral)</b>
2021-09	<b>XXVII Congresso Nazionale della Società Chimica Italiana (SCI2021).</b> Italy.	<b>S.Slimani</b> , G.Concas, F.Congiu, G.Barucca N.Yaacoub, A.Talone, M.Smari, E.Dhahri, D.Peddis, G.Muscas . Hybrid spinel iron oxide nanoarchitecture combining crystalline and amorphous parent material. <b>(Oral)</b>
2019-06	<b>10th Young Researcher Meeting</b> Rome,Italy.	<b>S.Slimani</b> , A. Talone, M. Abdolrahimi, M.Smari, E. Dhahri; D.Peddis. Designing Spinel Ferrite Nanoparticles by co-precipitation method. <b>(Poster)</b>
2020-02	<b>V-Italian School on Magnetism</b> Rome,Italy.	<b>S.Slimani</b> , A. Talone, L. Ruggiero, P. Imperatori G. Barucca, M.A. Ricci, A.Sodo, M.Smari, E.Dhahri ,D.Peddis,. Spinel iron oxide /SiO <sub>2</sub> nanoarchitectures for drug delivery: investigation of the magnetic properties. <b>(Poster)</b>
2021-02	<b>The 7th Italian Conference on Magnetism.</b> Florence, Italy.	<b>S.Slimani</b> , M. Smari, R. Hamdi, A. Bajorek D. Peddis, I. Walha, U. Koneva, E.Dhahri, Y. Haik. Enhancement of the magneto-transport behavior in phase-separated LACMO polycrystalline: unraveling the Role of multi-double exchange mechanism. <b>(Poster)</b>

### 7.3 Event Organization

1. Member of the Organizing Committee of the V -Italian National Conference on Magnetism 2020 (Rome).
2. Member of the Publishing Committee of the International Baltic Conference on Magnetism (IBCM): Focus on nanobiomedicine and smart materials, 2021, Svetlogorsk, Kaliningrad region, Russia.

### 7.4 Schools and Workshops

1. February. 2020 International School “V-Italian School on Magnetism”, February 3- 7, 2020 Rome, Italy.
2. Sept. 2020 International online Summer School” Electric and Magnetic Field-assisted Processing of Inorganic Materials”, September 14-16,2020, Germany.

Have you noticed any inaccuracy in the manuscript?  
Please let me know at the email [slimanisawssen@gmail.com](mailto:slimanisawssen@gmail.com).  
I will gladly include your name in the acknowledgement.

Yours sincerely  
-Sawssen.S-

## Bibliography

- [1] Z.A. Chubykalo-Fesenko O, Gonzalez J, Hernando B, Nanomagnetism., J. Nanosci. Nanotechnol. (2008).
- [2] J. Kudr, Y. Haddad, L. Richtera, Z. Heger, M. Cernak, V. Adam, O. Zitka, Magnetic nanoparticles: From design and synthesis to real world applications, Nanomaterials. 7 (2017). <https://doi.org/10.3390/nano7090243>.
- [3] M. Salvador, Á. Gallo-Cordova, A. Moyano, J.C. Martínez-García, M.C. Blanco-López, M. Puerto Morales, M. Rivas, Improved magnetic lateral flow assays with optimized nanotags for point-of-use inductive biosensing, Analyst. 145 (2020) 5905–5914. <https://doi.org/10.1039/d0an00849d>.
- [4] S. Bedanta, O. Petravic, W. Kleemann, Supermagnetism, Elsevier, 2015. <https://doi.org/10.1016/B978-0-444-63528-0.00001-2>.
- [5] Stephen Blundell, Magnetism in Condensed Matter, Oxford Univ. Press. (2001).
- [6] J.M.D. Coey, magnetism and magnetic materials, 2009.
- [7] N.M. Louis, Propriétés Magnétiques Des Ferrites, Ferrimagnétisme et antiFerromagnétisme, Ann. Phys. (1948).
- [8] K.H.J. Buschow and F.R. De Boer, physics of magnetism and magnetic materials, 2004.
- [9] P. Weiss, L'hypothèse du champ moléculaire et la propriété ferromagnétique, J. Phys. Théorique Appliquée. 6 (1907) 661–690. <https://doi.org/10.1051/jphysap:019070060066100>.
- [10] L. Néel, Some theoretical aspects of rock-magnetism, Adv. Phys. 4 (1955) 191–243. <https://doi.org/10.1080/00018735500101204>.
- [11] S.A. Majetich, T. Wen, O.T. Mefford, Magnetic nanoparticles, MRS Bull. 38 (2013) 899–903. <https://doi.org/10.1557/mrs.2013.230>.
- [12] C. Kittel, Theory of the structure of ferromagnetic domains in films and small particles, Phys. Rev. 70 (1946) 965–971. <https://doi.org/10.1103/PhysRev.70.965>.
- [13] Chris Binns, nANOMAGNETISM : FUNDAMENTALS AND APPLICATIONS, 2014. <https://doi.org/10.1016/B978-0-08-098353-0.00004-X>.
- [14] C. Luna, M. Del Puerto Morales, C.J. Serna, M. Vázquez, Multidomain to single-

- domain transition for uniform Co<sub>80</sub>Ni<sub>20</sub> nanoparticles, *Nanotechnology*. 14 (2003) 268–272. <https://doi.org/10.1088/0957-4484/14/2/332>.
- [15] R.C. O’Handley, *Modern Magnetic Materials Principles and Applications*, 2000.
- [16] Q. Li, C.W. Kartikowati, S. Horie, T. Ogi, T. Iwaki, K. Okuyama, Correlation between particle size / domain structure and magnetic properties of highly crystalline Fe<sub>3</sub>O<sub>4</sub> nanoparticles, *Sci. Rep.* (2017) 1–4. <https://doi.org/10.1038/s41598-017-09897-5>.
- [17] S. Bedanta, W. Kleemann, *Supermagnetism*, *J. Phys. D. Appl. Phys.* 42 (2009). <https://doi.org/10.1088/0022-3727/42/1/013001>.
- [18] C.P. Bean, J.D. Livingston, *Superparamagnetism*, *J. Appl. Phys.* 30 (1959) S120–S129. <https://doi.org/10.1063/1.2185850>.
- [19] D. Peddis, *Magnetic Properties of Spinel Ferrite Nanoparticles: Influence of the Magnetic Structure*, in: *Magn. Nanoparticle Assem.*, Pan Stanford, 2014: pp. 159–198. <https://doi.org/10.1201/b15657-6>.
- [20] V. Kusigerski, E. Illes, J. Blanusa, S. Gyergyek, M. Boskovic, M. Perovic, V. Spasojevic, Magnetic properties and heating efficacy of magnesium doped magnetite nanoparticles obtained by co-precipitation method, *J. Magn. Mater.* 475 (2019) 470–478. <https://doi.org/10.1016/j.jmmm.2018.11.127>.
- [21] T. Review, *Nanomagnetics*, (2003).
- [22] S. Blundell, D. Thouless, Magnetism in Condensed Matter, *Am. J. Phys.* (2003). <https://doi.org/10.1119/1.1522704>.
- [23] D. Jonge, D. Breder, Magnetic anisotropy, magnetization and band structure, *Ultrathin Magn. Struct. I An Introd. to Electron. Magn. Struct. Prop.* (2005) 21–90. [https://doi.org/10.1007/3-540-27232-1\\_2](https://doi.org/10.1007/3-540-27232-1_2).
- [24] G. Bayreuther, Magnetic surfaces, *Hyperfine Interact.* 47–48 (1989) 237–249. <https://doi.org/10.1007/BF02351610>.
- [25] N. Pérez, P. Guardia, A.G. Roca, M.P. Morales, C.J. Serna, O. Iglesias, F. Bartolomé, L.M. García, X. Batlle, A. Labarta, Surface anisotropy broadening of the energy barrier distribution in magnetic nanoparticles, *Nanotechnology*. 19 (2008). <https://doi.org/10.1088/0957-4484/19/47/475704>.
- [26] L. NÉEL, ANISOTROPIE MAGNÉTIQUE SUPERFICIELLE ET SURSTRUCTURES D’ORIENTATION, *LE J. Phys. LE RADIUM.* 4 (1954) 225–239. <https://doi.org/http://dx.doi.org/10.1051/jphysrad:01954001504022500>.
- [27] S. Mørup, M.F. Hansen, C. Frandsen, Magnetic interactions between nanoparticles, *Beilstein J. Nanotechnol.* 1 (2010) 182–190. <https://doi.org/10.3762/bjnano.1.22>.
- [28] S. M, M.F. Hansen, C. Frandsen, K. Lyngby, 1.14 Magnetic Nanoparticles,

(2011).

- [29] M.F. Hansen, S. Mørup, Models for the dynamics of interacting magnetic nanoparticles, *J. Magn. Magn. Mater.* 184 (1998) L262-274. [https://doi.org/10.1016/s0304-8853\(97\)01165-7](https://doi.org/10.1016/s0304-8853(97)01165-7).
- [30] S. Laureti, G. Varvaro, A.M. Testa, D. Fiorani, E. Agostinelli, G. Piccaluga, A. Musinu, A. Ardu, D. Peddis, Magnetic interactions in silica coated nanoporous assemblies of CoFe<sub>2</sub>O<sub>4</sub> nanoparticles with cubic magnetic anisotropy, *Nanotechnology.* 21 (2010). <https://doi.org/10.1088/0957-4484/21/31/315701>.
- [31] L.B. and D.F. J L Dormann, A dynamic study of small interacting particles : superparamagnetic model and spin-glass laws A dynamic study of small interacting particles : superparamagnetic model and spin-glass laws, (1987).
- [32] D. Fiorani, D. Peddis, Understanding dynamics of interacting magnetic nanoparticles: From the weak interaction regime to the collective superspin glass state, *J. Phys. Conf. Ser.* 521 (2014). <https://doi.org/10.1088/1742-6596/521/1/012006>.
- [33] S. Mjrup, M.B. Madsen, J. Franck, C.J.W. Koch, A NEW INTERPRETATION OF MOSSBAUER SPECTRA OF MICROCRYSTALLINE O ), 40 (1983) 163–174.
- [34] M. Uhl, B. Siberchicot, A first-principles study of exchange integrals in magnetite, *J. Phys. Condens. Matter.* 7 (1995) 4227–4237. <https://doi.org/10.1088/0953-8984/7/22/006>.
- [35] M. A. RUDERMAN AND C. KITTEL, Indirect Exchange Coupling of Nuclear Magnetic Moments by Conduction Electrons\*, 96 (1954) 99–102.
- [36] K. YosIDA, Magnetic Properties of Cu-Mn Alloys, 106 (1957) 893–898.
- [37] B.E. Warren, X-ray Diffraction, n.d.
- [38] C. Suryanarayana, M.G. Norton, Practical Aspects of X-Ray Diffraction, in: *X-Ray Diffr.*, Springer US, Boston, MA, 1998: pp. 63–94. [https://doi.org/10.1007/978-1-4899-0148-4\\_3](https://doi.org/10.1007/978-1-4899-0148-4_3).
- [39] Y.T. Prabhu, K.V. Rao, V.S.S. Kumar, B.S. Kumari, X-Ray Analysis by Williamson-Hall and Size-Strain Plot Methods of ZnO Nanoparticles with Fuel Variation, *World J. Nano Sci. Eng.* 04 (2014) 21–28. <https://doi.org/10.4236/wjnse.2014.41004>.
- [40] O.R. Log, L o g - n o r m a l Distributions across the Sciences : Keys and Clues, 51 (2001) 341–352.
- [41] M. Mcelfresh, Fundamentals of magnetism and magnetic measurements, (1994).
- [42] T.J. Gamey, Development and Evaluation of an Airborne Superconducting

Quantum Interference Device-Based Magnetic Gradiometer Tensor System for Detection , Characterization and Mapping of Unexploded Ordnance SERDP Project MM-1316 N / A, Environ. Res. (2008).

- [43] O. Gutfleisch, T. Gottschall, M. Fries, D. Benke, I. Radulov, K.P. Skokov, H. Wende, M. Gruner, M. Acet, P. Entel, M. Farle, Mastering hysteresis in magnetocaloric materials, *Philos. Trans. R. Soc. A Math. Phys. Eng. Sci.* 374 (2016). <https://doi.org/10.1098/rsta.2015.0308>.
- [44] J.I. Gittleman, B. Abeles, S. Bozowski, Superparamagnetism and relaxation effects in granular Ni-SiO<sub>2</sub> and Ni-Al<sub>2</sub>O<sub>3</sub> films, *Phys. Rev. B.* 9 (1974) 3891–3897. <https://doi.org/10.1103/PhysRevB.9.3891>.
- [45] M.F. Hansen, S. Mørup, Estimation of blocking temperatures from ZFC/FC curves, *J. Magn. Magn. Mater.* 203 (1999) 214–216. [https://doi.org/10.1016/S0304-8853\(99\)00238-3](https://doi.org/10.1016/S0304-8853(99)00238-3).
- [46] E.H. El-Hilo, K. O’Grady, Spin-glass behavior in a fine particle system, *IEEE Trans. Magn.* 27 (1991) 3570–3578. <https://doi.org/10.1109/20.102929>.
- [47] A.J. Rondinone, C. Liu, Z. John Zhang, Determination of magnetic anisotropy distribution and anisotropy constant of manganese spinel ferrite nanoparticles, *J. Phys. Chem. B.* 105 (2001) 7967–7971. <https://doi.org/10.1021/jp011183u>.
- [48] A.J. Rondinone, A.C.S. Samia, Z.J. Zhang, Superparamagnetic relaxation and magnetic anisotropy energy distribution in CoFe<sub>2</sub>O<sub>4</sub> spinel ferrite nanocrystallites, *J. Phys. Chem. B.* 103 (1999) 6876–6880. <https://doi.org/10.1021/jp9912307>.
- [49] E.P. Wohlfarth, Relations between Different Modes of Acquisition of the Remanent Magnetization of Ferromagnetic Particles, *J. Appl. Phys.* 29 (1958) 595–596. <https://doi.org/10.1063/1.1723232>.
- [50] P.E. Kelly, K. O’Grady, P.L. Mayo, R.W. Chantrell, Switching mechanisms in cobalt-phosphorus thin films, *IEEE Trans. Magn.* 25 (1989) 3881–3883. <https://doi.org/10.1109/20.42466>.
- [51] A. You, M.A.Y. Be, I. In, Exchange-coupled FePt nanoparticle assembly, 2583 (2016) 10–13. <https://doi.org/10.1063/1.1467976>.
- [52] E. Tronc, P. Prené, J.P. Jolivet, J.L. Dormann, J.M. Grenèche, Spin Canting in  $\gamma$ -Fe<sub>2</sub>O<sub>3</sub> Nanoparticles, *Hyperfine Interact.* 112 (1998) 97–100. <https://doi.org/10.1023/a:1011092712136>.
- [53] J.M.D. Coey, Noncollinear Spin Arrangement in Ultrafine Ferrimagnetic Crystallites, *Phys. Rev. Lett.* 27 (1971) 1140–1142. <https://doi.org/10.1103/PhysRevLett.27.1140>.
- [54] C. Berthomieu, R. Hienerwadel, Fourier transform infrared (FTIR)

- spectroscopy, *Photosynth. Res.* 101 (2009) 157–170. <https://doi.org/10.1007/s11120-009-9439-x>.
- [55] Mobilio, S.; Boscherini, F.; Meneghini, *Synchrotron Radiation: Basics, Methods and Applications.*, Springer Berlin Heidelberg, 2015.
- [56] A. Di Cicco, G. Aquilanti, M. Minicucci, E. Principi, N. Novello, A. Cognigni, L. Olivi, Novel XAFS capabilities at ELETTRA synchrotron light source, *J. Phys. Conf. Ser.* 190 (2009). <https://doi.org/10.1088/1742-6596/190/1/012043>.
- [57] I. Schiesaro, C. Battocchio, I. Venditti, P. Proposito, L. Burratti, P. Centomo, C. Meneghini, *Physica E: Low-dimensional Systems and Nanostructures* Structural characterization of 3d metal adsorbed AgNPs, *Phys. E Low-Dimensional Syst. Nanostructures.* 123 (2020) 114162. <https://doi.org/10.1016/j.physe.2020.114162>.
- [58] L.M. Sanchez, Magnetic nanoparticles-based hybrid materials for hyperthermia cancer treatments, in: *Magn. Nanoparticle-Based Hybrid Mater.*, 2021. <https://doi.org/10.1016/b978-0-12-823688-8.00022-3>.
- [59] J. Nogués, I.K. Schuller, Exchange bias, *J. Magn. Magn. Mater.* 192 (1999) 203–232. [https://doi.org/10.1016/S0304-8853\(98\)00266-2](https://doi.org/10.1016/S0304-8853(98)00266-2).
- [60] K. Sartori, G. Cotin, C. Bouillet, V. Halté, S. Bégin-Colin, F. Choueikani, B.P. Pichon, Strong interfacial coupling through exchange interactions in soft/hard core-shell nanoparticles as a function of cationic distribution, *Nanoscale.* 11 (2019) 12946–12958. <https://doi.org/10.1039/c9nr02323b>.
- [61] H. Gu, C. Liu, J. Zhu, J. Gu, E.K. Wujcik, L. Shao, N. Wang, H. Wei, R. Scaffaro, J. Zhang, Z. Guo, Introducing advanced composites and hybrid materials, *Adv. Compos. Hybrid Mater.* 1 (2018) 1–5. <https://doi.org/10.1007/s42114-017-0017-y>.
- [62] M. V. Efremova, V.A. Naumenko, M. Spasova, A.S. Garanina, M.A. Abakumov, A.D. Blokhina, P.A. Melnikov, A.O. Prelovskaya, M. Heidelmann, Z.-A. Li, Z. Ma, I. V. Shchetinin, Y.I. Golovin, I.I. Kireev, A.G. Savchenko, V.P. Chekhonin, N.L. Klyachko, M. Farle, A.G. Majouga, U. Wiedwald, Magnetite-Gold nanohybrids as ideal all-in-one platforms for theranostics, *Sci. Rep.* 8 (2018) 11295. <https://doi.org/10.1038/s41598-018-29618-w>.
- [63] F. Pineider, C. de Julián Fernández, V. Videtta, E. Carlino, A. al Hourani, F. Wilhelm, A. Rogalev, P.D. Cozzoli, P. Ghigna, C. Sangregorio, Spin-Polarization Transfer in Colloidal Magnetic-Plasmonic Au/Iron Oxide Hetero-nanocrystals, *ACS Nano.* 7 (2013) 857–866. <https://doi.org/10.1021/nn305459m>.
- [64] D. Psimadas, G. Baldi, C. Ravagli, M. Comes Franchini, E. Locatelli, C. Innocenti, C. Sangregorio, G. Loudos, Comparison of the magnetic, radiolabeling, hyperthermic and biodistribution properties of hybrid nanoparticles bearing CoFe<sub>2</sub>O<sub>4</sub> and Fe<sub>3</sub>O<sub>4</sub> metal cores., *Nanotechnology.* 25 (2014) 025101.

<https://doi.org/10.1088/0957-4484/25/2/025101>.

- [65] E. Katz, I. Willner, Integrated nanoparticle-biomolecule hybrid systems: Synthesis, properties, and applications, *Angew. Chemie - Int. Ed.* 43 (2004) 6042–6108. <https://doi.org/10.1002/anie.200400651>.
- [66] B.P. Vinayan, S. Ramaprabhu, Platinum–TM (TM = Fe, Co) alloy nanoparticles dispersed nitrogen doped (reduced graphene oxide-multiwalled carbon nanotube) hybrid structure cathode electrocatalysts for high performance PEMFC applications, *Nanoscale.* 5 (2013) 5109. <https://doi.org/10.1039/c3nr00585b>.
- [67] M.A. Bavio, A.G. Lista, Synthesis and characterization of hybrid-magnetic nanoparticles and their application for removal of arsenic from groundwater, *Sci. World J.* 2013 (2013). <https://doi.org/10.1155/2013/387458>.
- [68] A. Baeza, E. Guisasaola, E. Ruiz-Hernández, M. Vallet-Regí, Magnetically triggered multidrug release by hybrid mesoporous silica nanoparticles, *Chem. Mater.* 24 (2012) 517–524. <https://doi.org/10.1021/cm203000u>.
- [69] R. Liu, J. Duay, S.B. Lee, Heterogeneous nanostructured electrode materials for electrochemical energy storage, *Chem. Commun.* (2011). <https://doi.org/10.1039/c0cc03158e>.
- [70] R. Manjunatha, A. Karajić, M. Liu, Z. Zhai, L. Dong, W. Yan, D.P. Wilkinson, J. Zhang, A Review of Composite/Hybrid Electrocatalysts and Photocatalysts for Nitrogen Reduction Reactions: Advanced Materials, Mechanisms, Challenges and Perspectives, Springer Singapore, 2020. <https://doi.org/10.1007/s41918-020-00069-0>.
- [71] P. Maltoni, T. Sarkar, G. Barucca, G. Varvaro, F. Locardi, D. Peddis, R. Mathieu, Tuning the Magnetic Properties of Hard – Soft SrFe<sub>12</sub>O<sub>19</sub> / CoFe<sub>2</sub>O<sub>4</sub> Nanostructures via Composition / Interphase Coupling, *J. Phys. Chem. C* 2021., 125 (2021) 5927–5936. <https://doi.org/10.1021/acs.jpcc.1c00355>.
- [72] P. Maltoni, T. Sarkar, G. Varvaro, G. Barucca, S.A. Ivanov, D. Peddis, R. Mathieu, Towards bi-magnetic nanocomposites as permanent magnets through the optimization of the synthesis and magnetic properties of SrFe<sub>12</sub>O<sub>19</sub> nanocrystallites, *J. Phys. D. Appl. Phys.* 54 (2021). <https://doi.org/10.1088/1361-6463/abd20d>.
- [73] E.E. Fullerton, J.S. Jiang, S.D. Bader, Hard/soft magnetic heterostructures: model exchange-spring magnets, *J. Magn. Magn. Mater.* 200 (1999) 392–404. [https://doi.org/10.1016/S0304-8853\(99\)00376-5](https://doi.org/10.1016/S0304-8853(99)00376-5).
- [74] G. Muscas, P. Anil Kumar, G. Barucca, G. Concas, G. Varvaro, R. Mathieu, D. Peddis, Designing new ferrite/manganite nanocomposites, *Nanoscale.* 8 (2016) 2081–2089. <https://doi.org/10.1039/c5nr07572f>.
- [75] E. Kozenkova, K. Levada, M. V. Efremova, A. Omelyanchik, Y.A. Nalench, A.S.

- Garanina, S. Pshenichnikov, D.G. Zhukov, O. Lunov, M. Lunova, I. Kozenkov, C. Innocenti, M. Albino, M.A. Abakumov, C. Sangregorio, V. Rodionova, Multifunctional Fe<sub>3</sub>O<sub>4</sub>-Au Nanoparticles for the MRI Diagnosis and Potential Treatment of Liver Cancer, *Nanomaterials*. 10 (2020) 1646. <https://doi.org/10.3390/nano10091646>.
- [76] M. Salvador, A. Moyano, J.C. Martínez-García, M.C. Blanco-López, M. Rivas, Synthesis of Superparamagnetic Iron Oxide Nanoparticles: SWOT Analysis Towards Their Conjugation to Biomolecules for Molecular Recognition Applications, *J. Nanosci. Nanotechnol.* 19 (2019) 4839–4856. <https://doi.org/10.1166/jnn.2019.16931>.
- [77] A.G. Roca, L. Gutiérrez, H. Gavilán, M.E. Fortes Brollo, S. Veintemillas-Verdaguer, M. del P. Morales, Design strategies for shape-controlled magnetic iron oxide nanoparticles, *Adv. Drug Deliv. Rev.* 138 (2019) 68–104. <https://doi.org/10.1016/j.addr.2018.12.008>.
- [78] N.A. Spaldin, R. Ramesh, Advances in magnetoelectric multiferroics, *Nat. Mater.* 18 (2019) 203–212. <https://doi.org/10.1038/s41563-018-0275-2>.
- [79] N.A. Spaldin, Multiferroics beyond electric-field control of magnetism, *Proc. R. Soc. A Math. Phys. Eng. Sci.* 476 (2020). <https://doi.org/10.1098/rspa.2019.0542>.
- [80] G. Catalan, J. Seidel, R. Ramesh, J.F. Scott, Domain wall nanoelectronics, *Rev. Mod. Phys.* 84 (2012) 119–156. <https://doi.org/10.1103/RevModPhys.84.119>.
- [81] M. Trassin, Low energy consumption spintronics using multiferroic heterostructures, *J. Phys. Condens. Matter.* 28 (2016). <https://doi.org/10.1088/0953-8984/28/3/033001>.
- [82] P. Wang, E. Zhang, D. Toledo, I.T. Smith, B. Navarrete, N. Furman, A.F. Hernandez, M. Telusma, D. McDaniel, P. Liang, S. Khizroev, Colossal Magnetoelectric Effect in Core–Shell Magnetoelectric Nanoparticles, *Nano Lett.* (2020). <https://doi.org/10.1021/acs.nanolett.0c01588>.
- [83] Y. Wang, H. Zhao, L. Zhang, J. Chen, X. Xing, PbTiO<sub>3</sub>-based perovskite ferroelectric and multiferroic thin films, *Phys. Chem. Chem. Phys.* 19 (2017) 17493–17515. <https://doi.org/10.1039/c7cp01347g>.
- [84] T. Sarkar, G. Muscas, G. Barucca, F. Locardi, G. Varvaro, D. Peddis, R. Mathieu, Tunable single-phase magnetic behavior in chemically synthesized AFeO<sub>3</sub>-MFe<sub>2</sub>O<sub>4</sub> (A = Bi or La, M = Co or Ni) nanocomposites, *Nanoscale*. 10 (2018) 22990–23000. <https://doi.org/10.1039/c8nr06922k>.
- [85] P. Martins, Y. V. Kolen’ko, J. Rivas, S. Lanceros-Mendez, Tailored Magnetic and Magnetoelectric Responses of Polymer-Based Composites, *ACS Appl. Mater. Interfaces*. 7 (2015) 15017–15022. <https://doi.org/10.1021/acsami.5b04102>.

- [86] L.A. Makarova, Y.A. Alekhina, A.S. Omelyanchik, V.V. Rodionova, O.V. Malyshkina, N.S. Perov, Elastically coupled ferromagnetic and ferroelectric microparticles: New multiferroic materials based on polymer, NdFeB and PZT particles, *J. Magn. Mater.* 470 (2019) 89–92. <https://doi.org/10.1016/j.jmmm.2017.11.121>.
- [87] C. Vázquez-Vázquez, M.A. López-Quintela, M.C. Buján-Núñez, J. Rivas, Finite size and surface effects on the magnetic properties of cobalt ferrite nanoparticles, *J. Nanoparticle Res.* 13 (2011) 1663–1676. <https://doi.org/10.1007/s11051-010-9920-7>.
- [88] A. Omelyanchik, M. Salvador, F. D’Orazio, V. Mameli, C. Cannas, D. Fiorani, A. Musinu, M. Rivas, V. Rodionova, G. Varvaro, D. Peddis, Magnetocrystalline and Surface Anisotropy in CoFe<sub>2</sub>O<sub>4</sub> Nanoparticles, *Nanomaterials*. 10 (2020) 1288. <https://doi.org/10.3390/nano10071288>.
- [89] A. Omelanchik, G. Singh, B.H. McDonagh, V. Rodionova, D. Fiorani, D. Peddis, S. Laureti, From Mn<sub>3</sub>O<sub>4</sub>/MnO core–shell nanoparticles to hollow MnO: evolution of magnetic properties, *Nanotechnology*. 29 (2018) 055703. <https://doi.org/10.1088/1361-6528/aa9e59>.
- [90] E. Ferreira-Vila, L. Iglesias, I. Lucas Del Pozo, N. Varela-Dominguez, C.T. Bui, B. Rivas-Murias, J.M. Vila-Fungueiriño, P. Jimenez-Cavero, C. Magen, L. Morellon, V. Pardo, F. Rivadulla, Apparent auxetic to non-auxetic crossover driven by Co<sup>2+</sup> redistribution in CoFe<sub>2</sub>O<sub>4</sub> thin films, *APL Mater.* 7 (2019). <https://doi.org/10.1063/1.5087559>.
- [91] W.H. Meiklejohn, C.P. Bean, New Magnetic Anisotropy, *Phys. Rev.* 105 (1957) 904–913. <https://doi.org/10.1103/PhysRev.105.904>.
- [92] Q.K. Ong, A. Wei, X.-M. Lin, Exchange bias in Fe/Fe<sub>3</sub>O<sub>4</sub> core-shell magnetic nanoparticles mediated by frozen interfacial spins, *Phys. Rev. B.* 80 (2009) 134418. <https://doi.org/10.1103/PhysRevB.80.134418>.
- [93] Q.K. Ong, X.-M. Lin, A. Wei, Role of Frozen Spins in the Exchange Anisotropy of Core–Shell Fe@Fe<sub>3</sub>O<sub>4</sub> Nanoparticles, *J. Phys. Chem. C.* 115 (2011) 2665–2672. <https://doi.org/10.1021/jp110716g>.
- [94] P.K. Manna, S.M. Yusuf, R. Shukla, A.K. Tyagi, Exchange bias in BiFe<sub>0.8</sub>Mn<sub>0.2</sub>O<sub>3</sub> nanoparticles with an antiferromagnetic core and a diluted antiferromagnetic shell, *Phys. Rev. B.* 83 (2011) 184412. <https://doi.org/10.1103/PhysRevB.83.184412>.
- [95] Z.-A. Li, N. Fontañá-Troitiño, a Kovács, S. Liébana-Viñas, M. Spasova, R.E. Dunin-Borkowski, M. Müller, D. Doennig, R. Pentcheva, M. Farle, V. Salgueiriño, Electrostatic doping as a source for robust ferromagnetism at the interface between antiferromagnetic cobalt oxides., *Sci. Rep.* 5 (2015) 7997. <https://doi.org/10.1038/srep07997>.

- [96] S.D. Bader, S.S.P. Parkin, Spintronics, *Annu. Rev. Condens. Matter Phys.* 1 (2010) 71–88. <https://doi.org/10.1146/annurev-conmatphys-070909-104123>.
- [97] J.S. Lee, Y.W. Xie, H.K. Sato, C. Bell, Y. Hikita, H.Y. Hwang, C.C. Kao, Titanium dxy ferromagnetism at the LaAlO<sub>3</sub>/SrTiO<sub>3</sub> interface, *Nat. Mater.* 12 (2013) 703–706. <https://doi.org/10.1038/nmat3674>.
- [98] N. Fontañá-Troitiño, S. Liébana-Viñas, B. Rodríguez-González, Z.-A. Li, M. Spasova, M. Farle, V. Salgueiriño, Room-Temperature Ferromagnetism in Antiferromagnetic Cobalt Oxide Nanooctahedra, *Nano Lett.* 14 (2014) 640–647. <https://doi.org/10.1021/nl4038533>.
- [99] T. Tatarchuk, M. Bououdina, J. Judith Vijaya, L. John Kennedy, Spinel ferrite nanoparticles: Synthesis, crystal structure, properties, and perspective applications, *Springer Proc. Phys.* 195 (2017) 305–325. [https://doi.org/10.1007/978-3-319-56422-7\\_22](https://doi.org/10.1007/978-3-319-56422-7_22).
- [100] H. Qin, Y. He, P. Xu, D. Huang, Z. Wang, H. Wang, Z. Wang, Y. Zhao, Q. Tian, C. Wang, Spinel ferrites (MFe<sub>2</sub>O<sub>4</sub>): Synthesis, improvement and catalytic application in environment and energy field, *Adv. Colloid Interface Sci.* 294 (2021) 102486. <https://doi.org/10.1016/j.cis.2021.102486>.
- [101] A.F.S. Abu-Hani, S.T. Mahmoud, F. Awwad, A.I. Ayes, Design, fabrication, and characterization of portable gas sensors based on spinel ferrite nanoparticles embedded in organic membranes, *Sensors Actuators, B Chem.* 241 (2017) 1179–1187. <https://doi.org/10.1016/j.snb.2016.10.016>.
- [102] S.R. Bhongale, H.R. Ingawale, T.J. Shinde, K. Pubby, S. Bindra Narang, P.N. Vasambekar, Nano-crystalline Magnesium Substituted Cadmium Ferrites as X-band Microwave Absorbers, *J. Magn. Magn. Mater.* 441 (2017) 475–481. <https://doi.org/10.1016/j.jmmm.2017.06.026>.
- [103] M. Amiri, M. Salavati-Niasari, A. Akbari, Magnetic nanocarriers: Evolution of spinel ferrites for medical applications, *Adv. Colloid Interface Sci.* 265 (2019) 29–44. <https://doi.org/10.1016/j.cis.2019.01.003>.
- [104] D. Peddis, N. Yaacoub, M. Ferretti, A. Martinelli, G. Piccaluga, A. Musinu, C. Cannas, G. Navarra, J.M. Greneche, D. Fiorani, Cationic distribution and spin canting in CoFe<sub>2</sub>O<sub>4</sub> nanoparticles, *J. Phys. Condens. Matter.* 23 (2011). <https://doi.org/10.1088/0953-8984/23/42/426004>.
- [105] H. Dong, Y.C. Chen, C. Feldmann, Polyol synthesis of nanoparticles: status and options regarding metals, oxides, chalcogenides, and non-metal elements, *Green Chem.* 17 (2015) 4107–4132. <https://doi.org/10.1039/c5gc00943j>.
- [106] Z.N. Kayani, S. Arshad, S. Riaz, S. Naseem, Synthesis of Iron Oxide Nanoparticles by Sol-Gel Technique and Their Characterization, *IEEE Trans. Magn.* 50 (2014). <https://doi.org/10.1109/TMAG.2014.2313763>.

- [107] M. Unni, A.M. Uhl, S. Savliwala, B.H. Savitzky, R. Dhavalikar, N. Garraud, D.P. Arnold, L.F. Kourkoutis, J.S. Andrew, C. Rinaldi, Thermal Decomposition Synthesis of Iron Oxide Nanoparticles with Diminished Magnetic Dead Layer by Controlled Addition of Oxygen, *ACS Nano*. 11 (2017) 2284–2303. <https://doi.org/10.1021/acsnano.7b00609>.
- [108] S. Slimani, C. Meneghini, M. Abdolrahimi, A. Talone, J.P.M. Murillo, G. Barucca, N. Yaacoub, P. Imperatori, E. Illés, M. Smari, E. Dhahri, D. Peddis, Spinel Iron Oxide by the Co-Precipitation Method: Effect of the Reaction Atmosphere, *Appl. Sci.* 11 (2021) 5433. <https://doi.org/10.3390/app11125433>.
- [109] D.S. Mathew, R.S. Juang, An overview of the structure and magnetism of spinel ferrite nanoparticles and their synthesis in microemulsions, *Chem. Eng. J.* 129 (2007) 51–65. <https://doi.org/10.1016/j.cej.2006.11.001>.
- [110] R.K. Kotnala, J. Shah, *Ferrite Materials: Nano to Spintronics Regime*, Elsevier, 2015. <https://doi.org/10.1016/B978-0-444-63528-0.00004-8>.
- [111] E.W. Gorter, Saturation Magnetization and Crystal Chemistry of Ferrimagnetic Oxides \*, *Philips Res. Rep.* 9 (1954) 295–320. [http://www.extra.research.philips.com/hera/people/aarts/\\_Philips\\_Bound\\_Archive/PRRep/PRRep-09-1954-295.pdf](http://www.extra.research.philips.com/hera/people/aarts/_Philips_Bound_Archive/PRRep/PRRep-09-1954-295.pdf).
- [112] F. Nanoparticles, Structural and Magnetic Properties of Spinel, (2019) 4888–4902. <https://doi.org/10.1166/jnn.2019.16877>.
- [113] R.S. De Biasi, L.H.G. Cardoso, A simple model for the magnetocrystalline anisotropy in mixed ferrite nanoparticles, *Phys. B Phys. Condens. Matter.* 407 (2012) 3893–3896. <https://doi.org/10.1016/j.physb.2012.06.017>.
- [114] C. Cannas, A. Musinu, G. Piccaluga, Magnetic properties of cobalt ferrite – silica nanocomposites prepared by a sol-gel autocombustion technique, (2006) 1–11. <https://doi.org/10.1063/1.2354475>.
- [115] R. Massart, Preparation of Aqueous Magnetic Liquids in Alkaline and Acidic Media, *IEEE Trans. Magn.* 17 (1981) 1247–1248. <https://doi.org/10.1109/TMAG.1981.1061188>.
- [116] K. Petcharoen, A. Sirivat, Synthesis and characterization of magnetite nanoparticles via the chemical co-precipitation method, *Mater. Sci. Eng. B Solid-State Mater. Adv. Technol.* 177 (2012) 421–427. <https://doi.org/10.1016/j.mseb.2012.01.003>.
- [117] S.J. Lee, J.R. Jeong, S.C. Shin, J.C. Kim, J.D. Kim, Synthesis and characterization of superparamagnetic maghemite nanoparticles prepared by coprecipitation technique, *J. Magn. Mater.* 282 (2004) 147–150. <https://doi.org/10.1016/j.jmmm.2004.04.035>.
- [118] G. Muscas, G. Concas, C. Cannas, A. Musinu, A. Ardu, F. Orrù, D. Fiorani, S. Laureti, D. Rinaldi, G. Piccaluga, D. Peddis, Magnetic properties of small

- magnetite nanocrystals, *J. Phys. Chem. C.* 117 (2013) 23378–23384. <https://doi.org/10.1021/jp407863s>.
- [119] X. Batlle, M. García del Muro, a. Labarta, Interaction effects and energy barrier distribution on the magnetic relaxation of nanocrystalline hexagonal ferrites, *Phys. Rev. B.* (1997). <https://doi.org/10.1103/PhysRevB.55.6440>.
- [120] G. Muscas, G. Singh, W.R. Glomm, R. Mathieu, P.A. Kumar, G. Concas, E. Agostinelli, D. Peddis, Tuning the size and shape of oxide nanoparticles by controlling oxygen content in the reaction environment: Morphological analysis by aspect maps, *Chem. Mater.* 27 (2015) 1982–1990. <https://doi.org/10.1021/cm5038815>.
- [121] F. Orrù, A. Musinu, C. Cannas, D. Peddis, G. Piccaluga, A. Ardu, Interparticle Interactions and Magnetic Anisotropy in Cobalt Ferrite Nanoparticles: Influence of Molecular Coating, *Chem. Mater.* 24 (2012) 1062–1071. <https://doi.org/10.1021/cm203280y>.
- [122] K. O’Grady, R.W. Chantrell, *Remanence Curves of Fine Particle Systems I: Experimental Studies*, Elsevier B.V., 1992. <https://doi.org/10.1016/b978-0-444-89552-3.50017-7>.
- [123] O. Karaagac, H. Kockar, A simple way to obtain high saturation magnetization for superparamagnetic iron oxide nanoparticles synthesized in air atmosphere: Optimization by experimental design, *J. Magn. Magn. Mater.* 409 (2016) 116–123. <https://doi.org/10.1016/j.jmmm.2016.02.076>.
- [124] Z. Klencsár, A. Ábrahám, L. Szabó, E.G. Szabó, S. Stichleutner, E. Kuzmann, Z. Homonnay, G. Tolnai, The effect of preparation conditions on magnetite nanoparticles obtained via chemical co-precipitation, *Mater. Chem. Phys.* 223 (2019) 122–132. <https://doi.org/10.1016/j.matchemphys.2018.10.049>.
- [125] S. Laurent, D. Forge, M. Port, A. Roch, C. Robic, L. Vander Elst, R.N. Muller, Magnetic iron oxide nanoparticles: Synthesis, stabilization, vectorization, physicochemical characterizations and biological applications, *Chem. Rev.* 108 (2008) 2064–2110. <https://doi.org/10.1021/cr068445e>.
- [126] A.P. Lagrow, M.O. Besenhard, A. Hodzic, A. Sergides, L.K. Bogart, A. Gavriilidis, N.T.K. Thanh, Unravelling the growth mechanism of the co-precipitation of iron oxide nanoparticles with the aid of synchrotron X-Ray diffraction in solution, *Nanoscale.* 11 (2019) 6620–6628. <https://doi.org/10.1039/c9nr00531e>.
- [127] M.O. Besenhard, A.P. LaGrow, A. Hodzic, M. Kriechbaum, L. Panariello, G. Bais, K. Loizou, S. Damiros, M. Margarida Cruz, N.T.K. Thanh, A. Gavriilidis, Co-precipitation synthesis of stable iron oxide nanoparticles with NaOH: New insights and continuous production via flow chemistry, *Chem. Eng. J.* 399 (2020) 125740. <https://doi.org/10.1016/j.cej.2020.125740>.

- [128] T. Ahn, J.H. Kim, H.M. Yang, J.W. Lee, J.D. Kim, Formation pathways of magnetite nanoparticles by coprecipitation method, *J. Phys. Chem. C*. 116 (2012) 6069–6076. <https://doi.org/10.1021/jp211843g>.
- [129] I. Nedkov, T. Merodiiska, L. Slavov, R.E. Vandenberghe, Y. Kusano, J. Takada, Surface oxidation, size and shape of nano-sized magnetite obtained by coprecipitation, *J. Magn. Mater.* 300 (2006) 358–367. <https://doi.org/10.1016/j.jmmm.2005.05.020>.
- [130] F. Vereda, J. De Vicente, M. Del Puerto Morales, F. Rull, R. Hidalgo-Álvarez, Synthesis and characterization of single-domain monocrystalline magnetite particles by oxidative aging of Fe(OH)<sub>2</sub>, *J. Phys. Chem. C*. 112 (2008) 5843–5849. <https://doi.org/10.1021/jp711990f>.
- [131] H. Khurshid, P. Lampen-Kelley, Ò. Iglesias, J. Alonso, M.H. Phan, C.J. Sun, M.L. Saboungi, H. Srikanth, Spin-glass-like freezing of inner and outer surface layers in hollow  $\gamma$ -Fe<sub>2</sub>O<sub>3</sub> nanoparticles, *Sci. Rep.* 5 (2015) 1–13. <https://doi.org/10.1038/srep15054>.
- [132] A. Omelyanchik, K. Levada, S. Pshenichnikov, M. Abdolrahim, M. Baricic, A. Kapitunova, A. Galieva, S. Sukhikh, L. Astakhova, S. Antipov, B. Fabiano, D. Peddis, V. Rodionova, Green synthesis of co-zn spinel ferrite nanoparticles: Magnetic and intrinsic antimicrobial properties, *Materials (Basel)*. 13 (2020) 1–13. <https://doi.org/10.3390/ma13215014>.
- [133] A. López-Ortega, E. Lottini, C.D.J. Fernández, C. Sangregorio, Exploring the Magnetic Properties of Cobalt-Ferrite Nanoparticles for the Development of a Rare-Earth-Free Permanent Magnet, *Chem. Mater.* 27 (2015) 4048–4056. <https://doi.org/10.1021/acs.chemmater.5b01034>.
- [134] R.D. Shannon, C.T. Prewitt, Effective ionic radii in oxides and fluorides, *Acta Crystallogr. Sect. B Struct. Crystallogr. Cryst. Chem.* 25 (1969) 925–946. <https://doi.org/10.1107/S0567740869003220>.
- [135] A.T. Ngo, P. Bonville, M.P. Pileni, Spin canting and size effects in nanoparticles of nonstoichiometric cobalt ferrite, *J. Appl. Phys.* 89 (2001) 3370–3376. <https://doi.org/10.1063/1.1347001>.
- [136] S. Ayyappan, S. Mahadevan, P. Chandramohan, M.P. Srinivasan, J. Philip, B. Raj, Influence of Co<sup>2+</sup> Ion Concentration on the Size, Magnetic Properties, and Purity of CoFe<sub>2</sub>O<sub>4</sub> Spinel Ferrite Nanoparticles, (2010) 6334–6341.
- [137] G. Muscas, N. Yaacoub, G. Concas, F. Sayed, R. Sayed Hassan, J.M. Greneche, C. Cannas, A. Musinu, V. Foglietti, S. Casciardi, C. Sangregorio, D. Peddis, Evolution of the magnetic structure with chemical composition in spinel iron oxide nanoparticles, *Nanoscale*. 7 (2015) 13576–13585. <https://doi.org/10.1039/C5NR02723C>.
- [138] O.B. Pagar, H.S. Nagare, Y.M. Chine, R.R. Autade, P.R. Narode, V.M. Sanklecha,

Mesoporous Silica: A Review, *Int. J. Pharm. Drug Anal.* 6 (2018) 1–12.

- [139] A.M. Ewlad-Ahmed, M.A. Morris, S. V. Patwardhan, L.T. Gibson, Removal of formaldehyde from air using functionalized silica supports, *Environ. Sci. Technol.* 46 (2012) 13354–13360. <https://doi.org/10.1021/es303886q>.
- [140] B. Singh, J. Na, M. Konarova, T. Wakihara, Y. Yamauchi, C. Salomon, and M.B. Gawande, Functional Mesoporous Silica Nanomaterials for Catalysis and Environmental Applications, *Bull. Chem. Soc. Jpn.* (2020) 1459–1496. <https://doi.org/10.1246/bcsj.20200136>.
- [141] I.I. Slowing, J.L. Vivero-Escoto, C.W. Wu, V.S.Y. Lin, Mesoporous silica nanoparticles as controlled release drug delivery and gene transfection carriers, *Adv. Drug Deliv. Rev.* 60 (2008) 1278–1288. <https://doi.org/10.1016/j.addr.2008.03.012>.
- [142] E.G. Fuller, H. Sun, R.D. Dhavalikar, M. Unni, G.M. Scheutz, B.S. Sumerlin, C. Rinaldi, Externally Triggered Heat and Drug Release from Magnetically Controlled Nanocarriers, *ACS Appl. Polym. Mater.* 1 (2019) 211–220. <https://doi.org/10.1021/acsapm.8b00100>.
- [143] A.M. Derfus, G. Von Maltzahn, T.J. Harris, T. Duza, K.S. Vecchio, E. Ruoslahti, S.N. Bhatia, Remotely triggered release from magnetic nanoparticles, *Adv. Mater.* 19 (2007) 3932–3936. <https://doi.org/10.1002/adma.200700091>.
- [144] S. Zhou, Q. Zhong, Y. Wang, P. Hu, W. Zhong, C. Huang, Z. Yu, Chemically engineered mesoporous silica nanoparticles-based intelligent delivery systems for theranostic applications in multiple cancerous / non-cancerous diseases, 452 (2022). <https://doi.org/10.1016/j.ccr.2021.214309>.
- [145] F. Fiévet, S. Ammar-Merah, R. Brayner, F. Chau, M. Giraud, F. Mammeri, J. Peron, J.-Y. Piquemal, L. Sicard, G. Viau, The polyol process: a unique method for easy access to metal nanoparticles with tailored sizes, shapes and compositions, *Chem. Soc. Rev.* 47 (2018) 5187–5233. <https://doi.org/10.1039/C7CS00777A>.
- [146] F. Kim, S. Connor, H. Song, T. Kuykendall, P. Yang, Platonic gold nanocrystals, *Angew. Chemie - Int. Ed.* 43 (2004) 3673–3677. <https://doi.org/10.1002/anie.200454216>.
- [147] K.J. Carroll, J.U. Reveles, M.D. Shultz, S.N. Khanna, E.E. Carpenter, Preparation of elemental Cu and Ni nanoparticles by the polyol method: An experimental and theoretical approach, *J. Phys. Chem. C.* 115 (2011) 2656–2664. <https://doi.org/10.1021/jp1104196>.
- [148] C. Feldmann, Polyol-mediated synthesis of nanoscale functional materials, *Solid State Sci.* (2005). <https://doi.org/10.1016/j.solidstatesciences.2005.01.018>.

- [149] R.J. Joseyphus, T. Matsumoto, H. Takahashi, D. Kodama, K. Tohji, B. Jeyadevan, Designed synthesis of cobalt and its alloys by polyol process, *J. Solid State Chem.* (2007). <https://doi.org/10.1016/j.jssc.2007.07.024>.
- [150] A. Talone, L. Ruggiero, S. Slimani, P. Imperatori, G. Barucca, M.A. Ricci, A. Sodo, D. Peddis, Magnetic mesoporous silica nanostructures: Investigation of magnetic properties, *Nanotechnology.* 31 (2020). <https://doi.org/10.1088/1361-6528/abac7c>.
- [151] N.Q. Yin, P. Wu, T.H. Yang, M. Wang, Preparation and study of a mesoporous silica-coated Fe<sub>3</sub>O<sub>4</sub> photothermal nanoprobe, *RSC Adv.* 7 (2017) 9123–9129. <https://doi.org/10.1039/c6ra28413b>.
- [152] R.W. Chantrell, N.Y. Ayoub, J. Popplewell, The low field susceptibility of a textured superparamagnetic system, *J. Magn. Magn. Mater.* 53 (1985) 199–207. [https://doi.org/10.1016/0304-8853\(85\)90150-7](https://doi.org/10.1016/0304-8853(85)90150-7).
- [153] A.T. Ngo, M.P. Pileni, Assemblies of ferrite nanocrystals: Partial orientation of the easy magnetic axes, *J. Phys. Chem. B.* 105 (2001) 53–58. <https://doi.org/10.1021/jp002243j>.
- [154] G.F. Goya, T.S. Berquó, F.C. Fonseca, M.P. Morales, Static and dynamic magnetic properties of spherical magnetite nanoparticles, *J. Appl. Phys.* 94 (2003) 3520–3528. <https://doi.org/10.1063/1.1599959>.
- [155] S. Slimani, G. Concas, F. Congiu, G. Barucca, N. Yaacoub, A. Talone, M. Smari, E. Dhahri, D. Peddis, G. Muscas, Hybrid Spinel Iron Oxide Nanoarchitecture Combining Crystalline and Amorphous Parent Material, *J. Phys. Chem. C.* 125 (2021) 10611–10620. <https://doi.org/10.1021/acs.jpcc.1c00797>.
- [156] G. Herzer, The Random Anisotropy Model A Critical Review And Update, in: B. Idzikowski, P. Švec, M. Miglierini (Eds.), *Prop. Appl. Nanocrystalline Alloy. from Amorph. Precursors SE - 2*, Springer Netherlands, 2005: pp. 15–34. [https://doi.org/10.1007/1-4020-2965-9\\_2](https://doi.org/10.1007/1-4020-2965-9_2).
- [157] G. Muscas, G. Concas, S. Laureti, A.M. Testa, R. Mathieu, J.A. De Toro, C. Cannas, A. Musinu, M.A. Novak, C. Sangregorio, S.S. Lee, D. Peddis, The interplay between single particle anisotropy and interparticle interactions in ensembles of magnetic nanoparticles, *Phys. Chem. Chem. Phys.* 20 (2018) 28634–28643. <https://doi.org/10.1039/C8CP03934H>.
- [158] M. Knobel, W.C. Nunes, H. Winnischofer, T.C.R. Rocha, L.M. Socolovsky, C.L. Mayorga, D. Zanchet, Effects of magnetic interparticle coupling on the blocking temperature of ferromagnetic nanoparticle arrays, *J. Non. Cryst. Solids.* 353 (2007) 743–747. <https://doi.org/10.1016/j.jnoncrysol.2006.12.037>.
- [159] W.C. Nunes, L.M. Socolovsky, J.C. Denardin, F. Cebollada, A.L. Brandl, M. Knobel, Role of magnetic interparticle coupling on the field dependence of the

- superparamagnetic relaxation time, *Phys. Rev. B.* 72 (2005) 212413. <https://doi.org/10.1103/PhysRevB.72.212413>.
- [160] J. Weissmüller, A. Michels, J.G. Barker, A. Wiedenmann, U. Erb, R.D. Shull, Analysis of the small-angle neutron scattering of nanocrystalline ferromagnets using a micromagnetics model, *Phys. Rev. B.* 63 (2001) 214414. <https://doi.org/10.1103/PhysRevB.63.214414>.
- [161] a. Michels, R. Viswanath, J. Barker, R. Birringer, J. Weissmüller, Range of Magnetic Correlations in Nanocrystalline Soft Magnets, *Phys. Rev. Lett.* 91 (2003) 267204. <https://doi.org/10.1103/PhysRevLett.91.267204>.
- [162] G. Herzer, The Random Anisotropy Model, in: B. Idzikowski, P. Švec, M. Miglierini (Eds.), *Prop. Appl. Nanocrystalline Alloy. from Amorph. Precursors*, Springer-Verlag, Berlin/Heidelberg, 2005: pp. 15–34. [https://doi.org/10.1007/1-4020-2965-9\\_2](https://doi.org/10.1007/1-4020-2965-9_2).
- [163] A. Vansteenkiste, J. Leliaert, M. Dvornik, M. Helsen, F. Garcia-Sanchez, B. Van Waeyenberge, The design and verification of MuMax3, *AIP Adv.* 4 (2014). <https://doi.org/10.1063/1.4899186>.
- [164] D. Peddis, M. V Mansilla, S. Mørup, C. Cannas, A. Musinu, G. Piccaluga, F.D. Orazio, F. Lucari, D. Fiorani, Spin-Canting and Magnetic Anisotropy in Ultrasmall CoFe<sub>2</sub>O<sub>4</sub> Nanoparticles, *J. Phys. Chem. B.* 112 (2008) 8507–8513. <https://doi.org/10.1021/jp8016634>.
- [165] S. Roy, M.A. Peric, Functionalized nanoparticles as catalysts for enantioselective processes, (2009) 2669–2677. <https://doi.org/10.1039/b903921j>.
- [166] W.D. Chen, A.X. Kohll, B.H. Nguyen, J. Koch, R. Heckel, W.J. Stark, L. Ceze, K. Strauss, R.N. Grass, Combining Data Longevity with High Storage Capacity — Layer-by-Layer DNA Encapsulated in Magnetic Nanoparticles, (n.d.). <https://doi.org/10.1002/adfm.201901672>.
- [167] F. Hu, L. Wei, Z. Zhou, Y. Ran, Z. Li, M. Gao, Preparation of biocompatible magnetite nanocrystals for in vivo magnetic resonance detection of cancer, *Adv. Mater.* 18 (2006) 2553–2556. <https://doi.org/10.1002/adma.200600385>.
- [168] Y. Wang, Q. Zhao, N. Han, L. Bai, J. Li, J. Liu, E. Che, L. Hu, Q. Zhang, T. Jiang, S. Wang, Mesoporous silica nanoparticles in drug delivery and biomedical applications, *Nanomedicine Nanotechnology, Biol. Med.* 11 (2015) 313–327. <https://doi.org/10.1016/j.nano.2014.09.014>.
- [169] R.A. Bohara, D. Thorat, S.H. Pawar, Role of functionalization : strategies to explore potential nano-bio applications of magnetic, (2016) 43989–44012. <https://doi.org/10.1039/c6ra02129h>.
- [170] Y. Tanaka, S. Saita, S. Maenosono, Influence of surface ligands on saturation

- magnetization of FePt nanoparticles, *Appl. Phys. Lett.* 92 (2008) 7.
- [171] C.R. Vestal, Z.J. Zhang, Effects of surface coordination chemistry on the magnetic properties of MnFe<sub>2</sub>O<sub>4</sub> spinel ferrite nanoparticles, *J. Am. Chem. Soc.* 125 (2003) 9828–9833. <https://doi.org/10.1021/ja035474n>.
- [172] M. Vasilakaki, N. Ntallis, N. Yaacoub, G. Muscas, D. Peddis, K.N. Trohidou, Optimising the magnetic performance of Co ferrite nanoparticles: Via organic ligand capping, *Nanoscale.* 10 (2018) 21244–24253. <https://doi.org/10.1039/c8nr04566f>.
- [173] M. Abdolrahimi, M. Vasilakaki, S. Slimani, N. Ntallis, G. Varvaro, S. Laureti, C. Meneghini, K.N. Trohidou, D. Fiorani, D. Peddis, Magnetism of nanoparticles: Effect of the organic coating, *Nanomaterials.* 11 (2021). <https://doi.org/10.3390/nano11071787>.
- [174] A. Jedlovsky-Hajdú, F.B. Bombelli, M.P. Monopoli, E. Tombácz, K.A. Dawson, Surface coatings shape the protein corona of SPIONs with relevance to their application in vivo, *Langmuir.* 28 (2012) 14983–14991. <https://doi.org/10.1021/la302446h>.
- [175] M. Szekeres, E. Illés, C. Janko, K. Farkas, I.Y. Tóth, D. Nesztor, I. Zupkó, I. Földesi, C. Alexiou, E. Tombácz, Hemocompatibility and Biomedical Potential of Poly(Gallic Acid) Coated Iron Oxide Nanoparticles for Theranostic Use, *J. Nanomed. Nanotechnol.* 06 (2015) 252. <https://doi.org/10.4172/2157-7439.1000252>.
- [176] T.J. Daou, J.M. Grenèche, G. Pourroy, S. Buathong, A. Derory, C. Ulhaq-Bouillet, B. Donnio, D. Guillon, S. Begin-Colin, Coupling agent effect on magnetic properties of functionalized magnetite-based nanoparticles, *Chem. Mater.* 20 (2008) 5869–5875. <https://doi.org/10.1021/cm801405n>.
- [177] D. Maity, D.C. Agrawal, Synthesis of iron oxide nanoparticles under oxidizing environment and their stabilization in aqueous and non-aqueous media, *J. Magn. Mater.* 308 (2007) 46–55. <https://doi.org/10.1016/j.jmmm.2006.05.001>.
- [178] R. Kaiser, G. Miskolczy, Magnetic properties of stable dispersions of subdomain magnetite particles, *J. Appl. Phys.* 41 (1970) 1064–1072. <https://doi.org/10.1063/1.1658812>.
- [179] T. Muthukumar, J. Philip, Effect of phosphate and oleic acid capping on structure, magnetic properties and thermal stability of iron oxide nanoparticles, *J. Alloys Compd.* 689 (2016) 959–968. <https://doi.org/10.1016/j.jallcom.2016.08.067>.
- [180] T. Phenrat, N. Saleh, K. Sirk, R.D. Tilton, G. V. Lowry, Aggregation and sedimentation of aqueous nanoscale zerovalent iron dispersions, *Environ. Sci. Technol.* 41 (2007) 284–290. <https://doi.org/10.1021/es061349a>.

- [181] T. Phenrat, N. Saleh, K. Sirk, H.J. Kim, R.D. Tilton, G. V. Lowry, Stabilization of aqueous nanoscale zerovalent iron dispersions by anionic polyelectrolytes: Adsorbed anionic polyelectrolyte layer properties and their effect on aggregation and sedimentation, *J. Nanoparticle Res.* 10 (2008) 795–814. <https://doi.org/10.1007/s11051-007-9315-6>.
- [182] A. Sharma, J.W. Foppen, A. Banerjee, S. Sawssen, N. Bachhar, D. Peddis, S. Bandyopadhyay, Magnetic Nanoparticles to Unique DNA Tracers: Effect of Functionalization on Physico-chemical Properties, *Nanoscale Res. Lett.* 16 (2021). <https://doi.org/10.1186/s11671-021-03483-5>.
- [183] A. Nacev, C. Beni, O. Bruno, B. Shapiro, The behaviors of ferromagnetic nanoparticles in and around blood vessels under applied magnetic fields, *J. Magn. Mater.* 323 (2011) 651–668. <https://doi.org/10.1016/j.jmmm.2010.09.008>.
- [184] Y.L. Liu, D. Chen, P. Shang, D.C. Yin, A review of magnet systems for targeted drug delivery, *J. Control. Release.* 302 (2019) 90–104. <https://doi.org/10.1016/j.jconrel.2019.03.031>.



